Transfer reaction study of neutron rich beryllium isotopes.

Jacob Graversen Johansen

Department of Physics and Astronomy
Aarhus University, Denmark

Dissertation for the Degree of Doctor of Philosophy

November 2012

Jacob Graversen Johansen
Department of Physics and Astronomy
Aarhus University
Ny Munkegade, Bldg. 1520
8000 Århus C
Denmark

This dissertation has been submitted to the Faculty of Science and Technology at Aarhus University, Denmark, in partial fulfillment of the requirements for the PhD degree in physics. The work presented has been performed in the period from August 2008 to November 2012 under the supervision of Hans O. U. Fynbo and Karsten Riisager. The experimental work was carried out at the ISOLDE facility at CERN, switzerland, in September 2010. The analysis work was mainly carried out at the Department of Physics and Astronomy in Aarhus.

Contents

Résumé (English)

The experimental study of exotic nuclei plays an important part in the understanding of nuclear structure. This thesis describes an experimental study of ^{10,11,12}Be, three beryllium isotopes situated on the neutron rich side of the nuclear chart. The three isotopes were studied in direct reactions (scattering and transfer) using a low energy ^{11}Be beam incident on a deuteron target. The aim of the experiment was to study the breaking of the N=8 magic number occurring in ^{12}Be. The breaking is caused by the mixing of the $0p_{1/2}$ and the $1s_{1/2}0d_{5/2}$ shells. The mixing is also known to occur in ^{11}Be, but the strength of the mixing in ^{12}Be is still to be determined. The mixing can be determined by deriving the spectroscopic factors from direct reactions. The thesis will start with a description of the beryllium isotopes and an introduction to direct reactions including the definition of the spectroscopic factors.

The experimental data analysed in this thesis stem from an experiment performed in September 2010 at the radioactive ion beam facility, ISOLDE, situated at CERN, Switzerland. The experiment was the third and last experiment in a series of ^{11}Be+d experiments performed at ISOLDE. The first two experiments were performed in 2005 and 2009. The statistics in the first two experiments are significant lower than the statistic of the 2010 experiment and the first two experiments acted as preparation for the final experiment. The analysis of the two first experiments were performed from august 2008 to august 2010 and corresponds to the work done in the first two years of my PhD. The analysis formed the basis of my Part-A exam and will not be described in this thesis (the results can be found in 3 and 4 in the list of publications).

The analysis, described in this thesis, can be divided into three parts the initial part, the main part, and a more detailed analysis of the data. Information regarding the experimental setup is determined in the initial part. This part contains calibration of the detectors and determining their individual positions, but also a calculation of the beam structure. The differential cross sections and spectroscopic factors are determined in the main part of the analysis.

The last part of the analysis shows the strength of the setup by providing extra information about the three isotopes through a more detailed analysis.

Resumé (Dansk)

Eksperimentelle undersøgelser af eksotiske kerner er af stor betydning for forståelsen af kernestrukturerne. Denne afhandling beskriver en eksperimentel undersøgelse af de tre kerner ^{10,11,12}Be på den neutronrige side af kernekortet. De tre kerner er undersøgt ved hjælp af to slags direkte reaktioner - spredning og transfer. Reaktionerne er udført med et lavenergi-^{11}Be-beam på et deuteron-target. Målet med eksperimentet var at studere nedbrydningen af det magiske tal N=8 i ^{12}Be. Nedbrydningen opstår, fordi skallerne $s_{1/2}0d_{5/2}$ og $0p_{1/2}$ begynder at overlappe hinanden i ^{12}Be. Dette overlap er også set i ^{11}Be. Hvor meget, de to skaller overlapper, er dog endnu ikke blevet bestemt.

Denne afhandling begynder med en introduktion af beryllium isotoperne og en beskrivelse af direkte reaktioner, inklusiv definitionen af spektroskopiske faktorer. De spektroskopiske faktorer, som bestemmes fra direkte reaktioner, giver et indirekte mål for, hvor stor overlappet mellem de to skaller er..

De eksperimentelle data, der er analyseret og beskrevet i denne afhandling, stammer fra et eksperiment udført i september måned i 2010. Forsøget blev udført på den radioaktive-ionbeam-facillitet ISOLDE, som er en del af CERN, Schweiz. Dette eksperiment var det tredie og sidste af en række eksperimenter med ^{11}Be+d udført på ISOLDE. De to første eksperimenter blev udført i 2005 og 2009. Statistikken fra disse eksperimenter er væsentlig mindre end statistikken opnået i eksperimentet fra 2010. Man kan sige, at de to første eksperimentet er blevet brugt som forberedelse til sidste eksperiment. De to første forsøgs data er blevet analyseret i de første år af min PhD fra 2008 til 2010. Analysen er blevet beskrevet i min Del A-rapport og vil ikke blive beskrevet her (resultaterne fra eksperimenterne kan findes i 3 og 4 i listen over mine publikationer).

Analysen af det tredje forsøgs data er i denne afhandling delt op i tre dele; en indledende del, en hoveddel og en del, der indeholder mere detaljerede analyser. Den første del indeholder bestemmelsen af den eksperimentelle opstilling. Heri indgår både kalibrering af detektorerne, bestemmelse af deres

placering i forhold til target samt en bestemmelse af strukturen af beamet. De differentielle tværsnit og de spektroskopiske faktorer bliver bestemt og kommenteret i hoveddelen. Den sidste del af analysen viser, hvordan man kan udvinde ekstra information af kernerne ved hjælp af en mere detaljeret analyse.

Publications

1. *Characterization of low energy radioactive beams using direct reactions*
   Johansen J. G. , Bildstein V. , Fraser, M. , Voulot, D. , Wimmer, K. and Riisager, K. - To be submitted

2. *Three-body properties of low-lying 12Be resonances*
   Garrido, E. , Jensen, A. S. , Fedorov, D. V. and **Johansen, J. G.** (2012) - Physical Review C (Nuclear Physics). 86, 2, s. 024310. 12 s.

3. *Transfer reactions using a low-energy 11Be beam*
   Johansen, J. S. (2011) - A I P Conference Proceedings Series. s. 368-370. 3 s.

4. *Low Energy Transfer Reactions With 11Be*
   Johansen, J. S. (2009) - A I P Conference Proceedings Series. 1, s. 321-322.

5. *Discovery of the Shape Coexisting 0+ State in 32Mg by a Two Neutron Transfer Reaction*
   Wimmer, K. , Kröll, T. , Krücken, R. , Bildstein, V. , Gernhäuser, R. , Bastin, B. , Bree, N. , Diriken, J. , Van Duppen, P. , Huyse, M. , Patronis, N. , Vermaelen, P. , Voulot, D. , Van de Walle, J. , Wenander, F. , Fraile, L. M. , Chapman, R. , Hadinia, B. , Orlandi, R. , Smith, J. F. , Lutter, R. , Thirolf, P. G. , Labiche, M. , Blazhev, A. , Kalkühler, M. , Reiter, P. , Seidlitz, M. , Warr, N. , Macchiavelli, A. O. , Jeppesen, H. B. , Fiori, E. , Georgiev, G. , Schrieder, G. , Das Gupta, S. , Lo Bianco, G. , Nardelli, S. , Butterworth, J. , **Johansen, J. S.** and Riisager, K. (2010) - Physical Review Letters. 105, 25, s. 252501. 4 s.

6. *Transfer Reactions on Neutron-rich Nuclei at REX-ISOLDE*
   Kröll, T. , Bildstein, V. , Wimmer, K. , Krücken, R. , Gernhäuser, R. , Lutter, R. , Swerdtfeger, W. , Thiolf, P. , Bastin, B. , Bree, N. , Diriken, J.

, Huyse, M. , Patronis, N. , Raabe, R. , Van Duppen, P. , Vermaelen, P. , Cederkäll, J. , Clément, E. , Van de Walle, J. , Voulot, D. , Wenander, F. , Blazhev, A. , Kalkühler, M. , Reiter, P. , Seidlitz, M. , Warr, N. , Deacon, A. , Fitzpatrick, C. , Freeman, S. , Das Gupta, S. , Lo Bianco, G. , Nardelli, S. , Fiori, E. , Geogiev, G. , Scheck, M. , Fraile, L. M. , Balabanski, D. , Nilsson, T. , Tengborn, E. , Butterworth, J. , Nara Singh, B. S. , Angus, L. , Chapman, R. , Hadinia, B. , Orlandi, R. , Smith, J. F. , Wady, P. , Schrieder, G. , Labiche, M. , **Johansen, J. S.** , Riisager, K. , Jeppesen, H. B. , Macchiavelli, A. O. and Davinson, T. (2009) - A I P Conference Proceedings Series. 1, s. 363-368.

Acknowledgment

First of all I would like to thank my supervisors, Karsten Riisager and Hans Fynbo for introducing me to this interesting project. I have enjoyed my four years in the group and I have learned a lot. This project would not have turned out so well without the guidance of Karsten and Hans. All important details have been discussed thanks to their keen attention to the data. I am also grateful for the assistance they have given me with all my presentations.

I would also like to thank all the people, who participated in the experiments. A special thanks go to Kathrin Wimmer and Vinzenz Bildstein. Their immense help has been indispensable in the preparation and running of the experiment. I would also like to thank Kathrin and Vinzenz for their assistance in the introduction to the analysis and simulation programs.

The T-REX group deserves credit for the impressive beam they provided us. I would especially like to thank Fredrik Wenander, Didier Voulot and Matthew A. Fraser for their collaboration during the experiment. Their guidance and measurements have had a large impact on the characterisation of the beam.

I would also like to thank Antonio M. Moro and José Antonio Lay Valera for their hospitality during my stay in Seville. I enjoyed my stay very much. Their help during the calculations of the theoretical cross sections have been much appreciated.

Our collaborators in Madrid and Gothenburg also have my gratitude. They have always made me feel welcome, both during experiments and when staying in Gothenburg and Madrid.

Finally I would like to thank Emilie and Carl for their everlasting support. You keep putting a smile on my face. I love you both.

CHAPTER 1

Introduction

This chapter will give a short introduction to the field of fundamental nuclear physics, starting with the discovery of the nucleus a hundred years ago. The most important parts of the field, for this thesis, will be described.

1.1 Hundred years of nuclear physics

2011 marked the hundredth year for the discovery of the nucleus by E. Rutherford. During these hundred years a lot has happened in the field of physics including quantum mechanics and Bohr's atom model that leads to a description of the electron orbits around the nucleus. The building blocks of the nucleus (nucleons) have also been identified as the proton (Z) and the neutron (N), with the discovery of the latter in 1932 by J. Chadwick. Later the discovery of quarks opened up for an understanding of the deeper structures of the nucleons. Today we have the standard model, for which indications of the final piece (the Higgs boson) have been seen at the LHC within the last year [Aad12, Cha12].

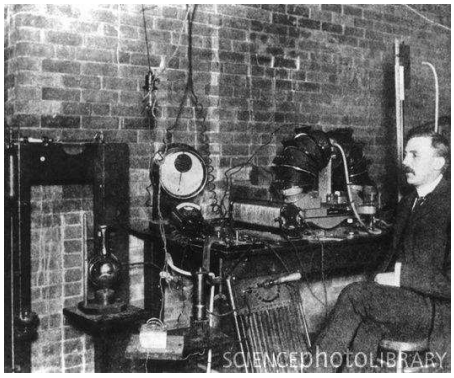

Figure 1.1: A picture of sir Ernest Rutherford in his laboratory.

The building blocks of the nucleus have been known for 80 years now, but the structure of nuclei is too complex to be calculated with QCD, even today. One of the major challenges arise from the large variation in the number of

nucleons from one to more than two hundred. Thus neither ab initio nor many body calculations can be used to describe all nuclei. Ab initio calculations are limited by todays computer power, hence only the lightest and simplest nuclei and reactions can be described using ab initio calculations. The limit today is around $A = 16$. Simplifications and generalisations have been used to go higher in mass, and various theories have been developed.

The theories are challenged by the constant discovery and production of more and more exotic nuclei. Hundred new isotopes were produced alone in 2010 [Tho11] For years, only the natural isotopes were known, and most of the theories have been developed from natural occurring isotopes. It was not until the development of the first ISOL facilities in the mid 60's that radioactive nuclei were studied systematically. Later the development of RIB facilities has lead to an increase in the number of known isotopes and today more than 3000 different isotopes have been studied [Tho11]. Fig. 1.2 shows the development of the nuclear chart from the early days with only natural occurring isotopes to today, where the drip line is reached for many elements, and heavy nuclei, beyond $Z = 110$, have been produced and studied in laboratories. Recent mean field calculations have shown, that the total number of p- and n-bound nuclei is approximately 7000 [Erl12]. Hence, experimental knowledge is only gained for half of all bound isotopes. The study of the more exotic nuclei have shown strong effects caused by the imbalance between neutrons and protons. The binding energies, masses, states and shapes of the nuclei are all affected by the number of the neutrons and protons and the ratio between the two. Theories, that are developed for stable nuclei, break down when going into the more exotic regions of the nuclear chart. The theories, therefore have to be modified to describe the more and more exotic nuclei discovered.

How the shape of the nuclei and the ordering of the states behave in the neutron rich low mass region of the nuclear chart will be studied in this thesis.

1.2 The disappearance of magic numbers

An important part of fundamental nuclear physics is to understand the properties of the bound states and resonances in nuclei (e.g. excitation energy, spin and parity). The theoretic models for calculating the properties are similar to

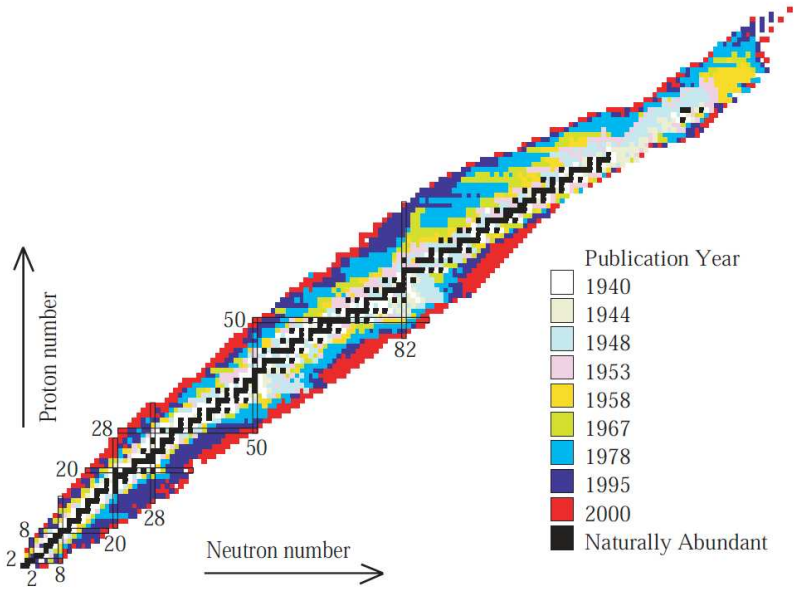

Figure 1.2: The nuclear chart. The isotopes are color-coded according to the time of discovery.

the theory used in atomic physics, where electrons are orbiting a core (the nucleus) in different shells, corresponding to different energies and quantum numbers. The problem in nuclear physics is the lack of a central potential. In atomic physics the main force acting on the electrons is from the nucleus, which is much heavier than the electrons, and can be assumed stationary. The electrons movement can then be described from a central potential caused by the nucleus, and other forces enter as perturbations. In a nucleus the forces acting on nucleons are from other nucleons, with similar masses and nuclear charges, hence a central potential description is not as useful as for the atom. Instead the potential used in the calculation has to be a combination of the potentials between the individual nucleons (ab initio calculations). Such calculations are too complicated for most isotopes and isotopes beyond A=16 have only recently been described by no-core shell models [Nav09]. Simplifications have to be made in order to go higher in number of nucleons.

In the shell model a nucleus is divided into core and valence nucleons. A potential formed by the core nucleons is used to determine the energies of the

shells. The valence nucleons are then filled into the shells (like electrons in an atom). The spin and parity of the states in the nucleus are thus given by the shells occupied by the valence nucleons.

In atomic physics some number of electrons are more stable than others, corresponding to closed shells. The same effect is seen in the shell model, known as the magic numbers: N = 8, 20, 28, 50, 82 and 126. The magic numbers arise from large energy gaps between certain shells. The energies of the different shells are determined by the structure of the core potential. The normal core potential is given by a wood-saxon potential with a spin-orbit term:

$$V(r) = \frac{-V_0}{1 + e^{r-R/a}} + V_{so}(r)\mathbf{L} \cdot \mathbf{S}. \tag{1.1}$$

This form will lead to large energy gaps above the magic numbers. This theory was already developed in 1949 by Mayer and Jensen. The study of more exotic nuclei has shown that the magic numbers break down when going away from stability and approaching the drip lines. This is caused by the core potentials dependency of the nucleons. The potential given in eq. (1.1) is derived from stable nuclei, but the potential is altered when going away from stability, leading to a movement of the levels. This movement leads to a closing and opening of energy gaps, which again can lead to a breaking of the magic numbers, like N=20 in the island of inversion around ^{32}Mg and N=8 in ^{12}Be, or the appearance of new magic numbers like N=16 in ^{24}O [Sor08]. The determination and understanding of the breaking and emerging of magic numbers is an important part of modern nuclear physics, as it can be used to describe the movement of energy levels across the nuclear chart. The experiment described in this thesis was mainly motivated by the N=8 magic number breaking in ^{12}Be.

The shell model calculations are heavily improved compared to the earliest calculations of Mayer and Jensen and provides a much better description of exotic nuclei today. The detailed description of the various shell model methods are beyond the scope of this thesis and for more details see E. Caurier et al. [Cau05]

1.3 Deformed nuclei

One of the effects, that contributes to the movement of the shells, is the deformation of the nuclei. The potential in eqn. 1.1 is derived for a spherical nucleus, but many nuclei have been shown to have a deformed shapes even in the ground state. Two types of deformations can occur, the prolate and the oblate deformation, fig. 1.3. The deformation of isotopes when going away from stability has been studied for many elements. The deformation is especially prominent in the Hg isotopes with an alternation between spherical and deformed ground states, see Heyde and Wood [Hey11] for more details.

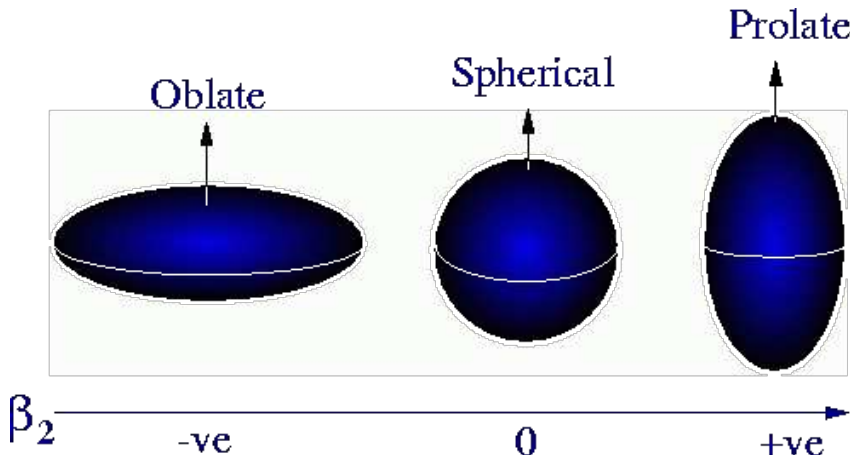

Figure 1.3: The three shapes, prolate, spherical and oblate, of nuclei.

The effect from the deformation on the shells was derived by S. G. Nilsson in 1955 [Nil55]. Fig. 1.4 shows the energy levels as a function of the deformation. The changes in energy gaps are clearly seen, leading to changes in the magic numbers.

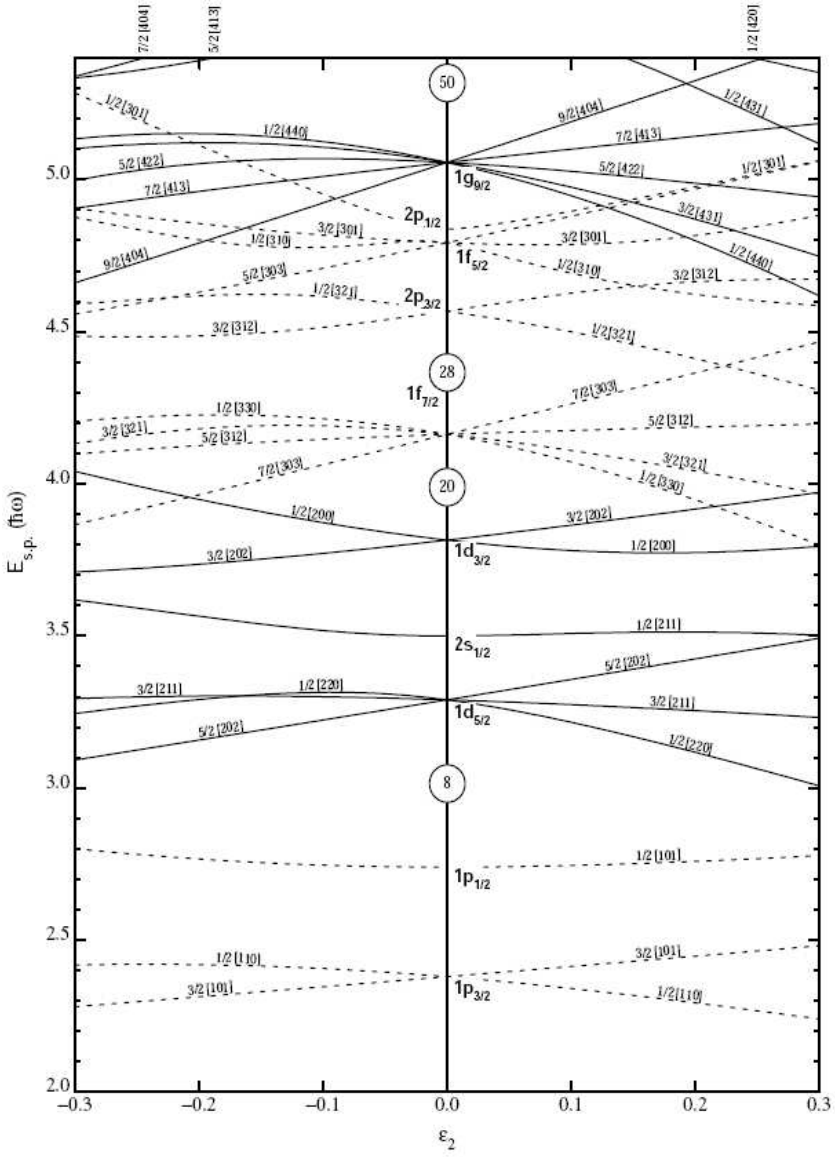

Figure 4. Nilsson diagram for protons or neutrons, Z or N ≤ 50 (ε_4 = 0).

Figure 1.4: A plot of the energy levels dependency on the deformation of the nuclei. The plot is derived using the model by S. G. Nilsson

1.4 Clustering in nuclei

Another important aspect in fundamental nuclear physics is the clustering of nucleons inside a nucleus. Theoretical calculations are currently trying to establish, when clustering occurs in nuclei [Ebr12].

Some nuclei are more energetically favorable and stable than others. The best known is the α-particle (^{4}He), which is much stronger bound than the neighboring nuclei. The α-clustering is quite prominent in the $N\alpha$-nuclei (^{4}He, ^{8}Be, ^{12}C etc.). All these nuclei show clear indications of being clusters of α-particles. ^{8}Be is an unbound nucleus and is the lightest nucleus that α-decays. The triple α-process leading to the production of ^{12}C shows the great importance of clustering in nuclear astrophysics. ^{12}C is also an example of clusters forming a stable nucleus. Nuclei containing clusters of different particles are known as well, like ^{7}Li (^{4}He+^{3}H) or the neutron rich beryllium isotopes (^{4}He+^{4}He+N·n). The effect of the clustering in the latter ones will be described in the next chapter.

The clustering within a nucleus will lead to a deformation of the nucleus, as the clusters will be separated. Taking ^{8}Be as an example, the two α-particles will be moving around each other making a deformed shape, rather than forming a spherical nucleus with 4N and 4Z. Furthermore the clustering can lead to new types of excited states due to the excitation of a cluster rather than a single valence nucleon or collective motions.

1.5 Halo nuclei

A special type of cluster nuclei are the halo nuclei. Halo nuclei appear close to the drip lines and are characterised by low binding energies and large matter radii [Jen04]. Furthermore the nucleus left after the removal of one (or two) nucleon(s) is strongly bound. Three types of halo nuclei have been seen, one-proton halos (^{2}H and ^{8}B), one-neutron halos (^{2}H, ^{11}Be, ^{19}C and ^{31}Ne) and two-neutron halos (^{6}He, ^{11}Li, ^{14}Be and ^{22}C) [Rii12]. The low binding energy and the large radius in halo nuclei are interpreted as a clustering containing a core (the strongly bound nucleus) and one or two nucleons orbiting the core at a large distance. The orbiting nucleons are called halo nucleons and the large distance between the core and the halo(s) leads to the large matter radius. The

large distance also makes it easy to separate the halo nucleon from the core, hence the low binding energy.

Interestingly all known two-neutron halo nuclei are Borromean nuclei. The total system is bound, but two of the three together are unbound, like ^{11}Li, which is bound, but n+n and ^{9}Li+n (^{10}Li) are both unbound [Jen04].

Halo structures can also occur in excited states of nuclei, even if the ground state is not a halo state. An example is the excited states in ^{10}Be described in section 2.4. The excited 1^-_1-state in ^{12}Be has been suggested as a two-neutron halo in a three-body calculation by C. Romero-Redondo et al. [RR08a]. If this is indeed true, the 1^-_1-state would be one of the first known non-Borromean two-neutron halo state. The ^{10}Be+n is bound (though very weakly) making the 1^-_1-state a tango state rather than a Borromean [Jen04].

The effect of a halo nucleon in reactions have been studied both experimentally and theoretically, examples can be found in [Sum07, CG97, Joh97]. The experiment described in this thesis represents one of the more complex studies. The reaction is a halo nucleus (^{11}Be) on another halo nucleus (^{2}H), and the final states can be both one- and two-neutron halo states.

CHAPTER 2

Neutron rich beryllium isotopes

The neutron rich beryllium isotopes, ^{11,12,10}Be, will be described in this thesis. The focus will be on the nuclear structure and the characteristics of the individual bound states in the three nuclei. The chapter will serve as a motivation for studying ^{11,12,10}Be.

2.1 Beryllium isotopes

This thesis describes an experimental study of the three neutron rich beryllium isotopes ^{10}Be, ^{11}Be and ^{12}Be. Beryllium (Z=4) is in the low mass region (^{14}Be being the heaviest bound beryllium isotope) of the nuclear chart. The low mass makes ab initio calculations possible for most beryllium isotopes. Furthermore beryllium isotopes plays important roles in both the breaking of magic numbers, clustering and halo structures, described in the previous chapter.

One of the most studied beryllium isotopes is the unstable ^{8}Be, which is of great importance in astrophysics. ^{8}Be is known as a two-α cluster and plays an important role as an intermediate state in the triple-alpha process. The ground state is a resonance with a width of $\Gamma = 5.57\,\text{eV}$ [Wus92]. The two-α cluster structure of ^{8}Be recurs in the more neutron rich nuclei like the stable ^{9}Be and ^{10}Be. They have been treated as three and four particle clusters in AMD (Antisymmetrised Molecular Dynamics) calculations [Oer97, Ita00]. Going further into the neutron rich side of the beryllium isotopes, the separation of the two-α particles starts to disappear. Nonetheless, the possible α+neutrons clusterings in ^{11}Be and ^{12}Be are investigated [KE02, Fre10]. The clustering in the beryllium isotopes makes the nuclei deformed. The deformations of ^{10}Be and ^{11}Be are believed to play an important role in direct reactions [For99, Aum00]. The effect of the deformation in the experiment discussed here is examined in chapter 8.

The neutron rich beryllium isotopes also shows interesting behavior from a shell model point of view. ^{11}Be is known for the inversion of the $1/2^+$ and $1/2^-$ states indicating a mixing of the $1s0d$ and the $0p$ shell. A mixing that leads to the breaking of the N=8 magic number in ^{12}Be.

^{11,12,10}Be will be described in more detail in the next sections.

2.2 ^{11}Be

^{11}Be is one of the few known one-neutron halo nuclei, section 1.5. The neutron separation energy is only 501 keV and the matter radius is much larger than for the neighboring nuclei (e.g. $r_m = 2.91$ fm in ^{11}Be compared to $r_m = 2.09$ fm for ^{11}B). The charge radius on the other hand is comparable ($r_c = 2.47$ fm in ^{11}Be compared to $r_c = 2.48$ fm for ^{11}B). This is all the characteristics of a neutron halo nucleus. ^{11}Be is interpreted as a core of ^{10}Be and a neutron orbiting the core at a relative long distance, fig. 2.1. ^{11}Be is considered a two body system (^{10}Be+n) in this thesis. The halo structure and the deformation of ^{11}Be is strongly affecting reactions involving ^{11}Be. Elastic scattering of ^{11}Be on heavier nuclei close to the coulomb barrier have been studied [DP10] and potentials that work for nuclei close to ^{11}Be fail to reproduce the experimental scattering cross sections of ^{11}Be. Resent DWBA calculations on a ^{10}Be(d,p)^{11}Be experiment also showed a discrepancy between theory and experiment [Sch12]. An attempt to determine the reaction potentials for halo nuclei is made by A. Bonnacorso et al. [Bon02]. They conclude, that a neutron halo leads to a large diffusiness of the imaginary part of the potential.

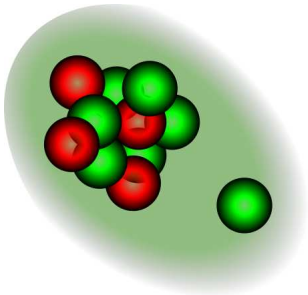

Figure 2.1: A drawing of a ^{11}Be nucleus indicating the halo structure, which leads to a deformed nucleus with a large matter radius.

The mixing of the $1s0d$ and the $0p$ shell is another interesting effect seen in ^{11}Be. Despite the low neutron separation energy, ^{11}Be have two bound states a $1/2^+$ ground state and a $1/2^-$-state with

an excitation energy of $E^* = 0.320$ MeV. Furthermore a low lying resonance at $E^* = 1.78$ MeV is known, fig. 2.2. The particle structure in the two-body model of the three states/resonance are:

$$|^{11}\mathrm{Be}; 1/2^+\rangle = \alpha_+ |^{10}\mathrm{Be}; 0^+_1\rangle |n; s_{1/2}\rangle + \beta_+ |^{10}\mathrm{Be}; 2^+_1\rangle |n; d_{5/2}\rangle . \quad (2.1)$$

$$|^{11}\mathrm{Be}; 1/2^-\rangle = \alpha_- |^{10}\mathrm{Be}; 0^+_1\rangle |n; p_{1/2}\rangle + \beta_- |^{10}\mathrm{Be}; 2^+_1\rangle |n; p_{3/2}\rangle . \quad (2.2)$$

$$|^{11}\mathrm{Be}; 5/2^+\rangle = |^{10}\mathrm{Be}; 0^+_1\rangle |n; d_{5/2}\rangle . \quad (2.3)$$

Only the simplest configuration is taken for the resonance, but small amounts of other terms are expected as well. The small energy required to excite the neutron from the *s*-shell to the *p*-shell and the fact that the *p*-shell configuration is placed between the *s*- and the *d*-shell configurations indicates a strong mixing of the two shells [Tal60]. The 0*p* and the 1*s*0*d* shells are strongly separated close to stability ($E^*_{1/2^+} - E^*_{1/2^-} = 3.09$ MeV for ^{13}C and 5.18 MeV for ^{15}O). The mixing is an example of the movement of the shells when going away from stability [Han01]. The strong mixing and the low separation energy affect the scattering and transfer reaction as well. ^{11}Be is easily excited and a strong coupling between the two bound states is expected, as well as a coupling to the low lying resonance [Mor06]. This has to be taken into account when interpreting the data, section 8.4

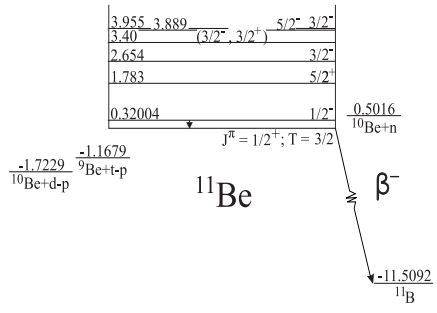

Figure 2.2: The bound states and the lowest resonances of ^{11}Be. The picture is taken from the TUNL datagroup [TUN].

2.3 ^{12}Be

The mixing of the 1*s*0*d* and the 0*p* shell is proven to appear in ^{12}Be as well, breaking the N=8 magic number. The mixing was already suggested by F. Barker et al. in 1976 [Bar76], who studied the beta decay of ^{12}Be. The β-decay strength was too weak for the ground state to be purely described

by a p^2 configuration for the two valence neutrons. The theory was supported by the low lying 2^+_1 excited state [Alb78], and spectroscopic factors determined in a neutron knockout exeperiment [Nav00]. The breaking of the N=8 magic number was finally confirmed in 2003 with the discovery of the low lying 0^+_2-state ($E^* = 2.2\,\text{MeV}$) by Shimoura et al. [Shi03], fig. 2.3.

The mixing of the shells have been studied in several break-up reactions [Nav00, Shi07, Pai06] as well as a few transfer reactions [For94, Kan10]. The first transfer experiment populating ^{12}Be (^{10}Be(t,p)^{12}Be) by Fortune et al. [For94] was able to populate the ground state, the 2^+_1- and the 1^-_1-state. No spectroscopic factors were determined and the spin assignment for the 2.70 MeV-state was suggested to be 0^+. This value has later been disproved and the spin and parity of the 2.70 MeVstate is accepted to be 1^- [Iwa00]. The second transfer reaction, a low energy ^{11}Be(d,p)^{12}Be transfer like the one described in this thesis, was also unable to clearly identify the 0^+_2-state, but spectroscopic factors were determined for all four bound states [Kan10]. The experimental spectroscopic factors were not consistent with theoretical ones, and new calculations have put doubt on the results from the transfer reaction experiment [For11]. Hence the amount of shell mixing in ^{12}Be is still to be determined, and the aim of the experiment discussed in this thesis is to provide new spectroscopic factors for all bound states including the 0^+_2-state from a (d,p) reaction.

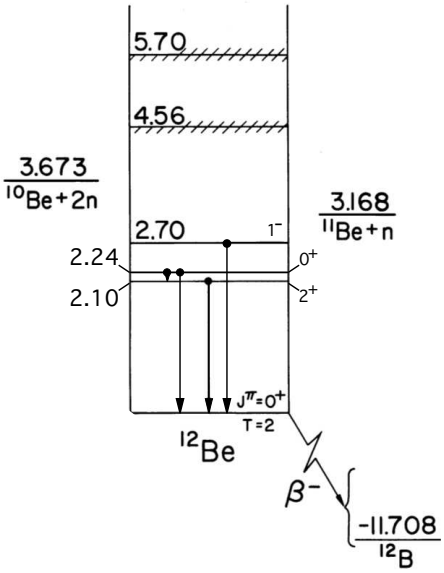

Figure 2.3: The bound states and the lowest resonances of ^{12}Be. The picture is taken from the TUNL datagroup [TUN] and modified to contain all accepted states and spin-parity values.

Furthermore, three body calculations have been performed by C. Romero-Redondo et al. in 2008 [RR08b] successfully describing the bound states of ^{12}Be. The 1^-_1-state shows indications of being a two-neutron halo state in the calculations. The model, furthermore, predicts a bound 0^--state [RR08a], which has never been seen. New improved calculations of the three body model have recently been performed, in order to predict the spin and parity of the low lying resonances [Gar12]. The 0^--state is moved up in excitation energy in the calculation, and a 0^--resonance just above the 1n-treshold is suggested rather than a bound 0^--state.

2.4 ^{10}Be

The very long lifetime of ^{10}Be (1×10^6 y) and the possibility of using stable beams to study ^{10}Be have made the study of ^{10}Be accessible for many years, and the structure of ^{10}Be is well known. The ^{11}Be(d,t)^{10}Be channel of the experiment has proven very interesting though. Both from an experimental and technical point of view and for an understanding of the structures of ^{11}Be and ^{10}Be. The ground state of ^{11}Be has two components, eqn. 2.1, and removing the halo neutron in a transfer would leave ^{10}Be in either the ground or the first excited state, seen in fig. 2.4. The high lying 1^-_1- and 2^-_1-states can be populated by knocking out one of the core neutrons, leaving the halo neutron orbiting the new ^{9}Be core. This is consistent with the interpretation of the two states being one-neutron halo states [AK06]. The last two states require multistep reactions to populate, and the reaction cross sections are expected to be small compared to the other reaction channels. Especially the 0^+_2-state is expected to be weakly populated.

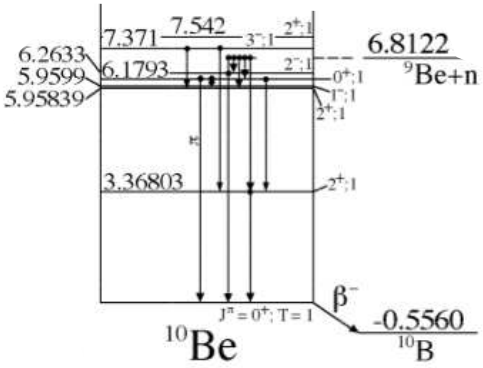

Figure 2.4: The bound states and the lowest resonances of ^{10}Be. The picture is taken from the TUNL datagroup [TUN].

The population requires both a knockout of a core neutron and an excitation of another core neutron from the $0p_{3/2}$-shell to the $1s_{1/2}$ shell. The 2^+_2-state requires a core neutron knockout but only an excitation of the halo neutron from the $1s_{1/2}$ shell to the $0p_{1/2}$ shell, which is much more likely, due to the mixing of the two shells in ^{11}Be.

2.5 The study of the isotopes

^{11}Be is the starting point of the experiment and is studied through scattering experiments. ^{10,12}Be are studied through one neutron transfers from or to ^{11}Be using a deuteron target.

The four highly excited states in ^{10}Be are very close in excitation energy, fig. 2.4, making them hard to distinguish in a transfer experiment if only charged particles are detected. Two of the four states are successfully identified and a third tentatively seen in this experiment, shown in chapter 7, proving how strong a setup is with both charged particle and gamma detection. The high resolution (10 keV) for germanium detectors used for gamma detection is a necessity to separate events from the four states,

The gamma energy from the decay of all excited states in ^{10,11,12}Be are shown in table 2.1 along with the branching ratios. The values are taken from C. M. Mattoon et al. [Mat09] for ^{10,11}Be and S. Shimoura et al. [Shi07] and H. Iwasaki et al. [Iwa00] for ^{12}Be. The only states that might produce gammas within 100 keV of each other is the four excited states in ^{10}Be, the rest should be easily identified in a gamma spectrum, chapter 7. All four highly excited states in ^{10}Be decay to the 2^+_1-state generating four gamma lines, which is pairwise separated with less than 100 keV. Only the 2^+_2- and the 2^-_1-states decays completely (or almost) to the 2^+_1-state. The 0^+_2 and the 1^-_1 have two other strong decays, a 219.2 keV ($0^+_2 \rightarrow 1^-_1$) and a 5959 keV ($1^-_1 \rightarrow 0^+_1$), which can be used to determine the population of the 0^+_2 and the 1^-_1 states respectively, section 7.2.3.

Nucleus	Decay	E_γ [keV]	BR [%]
^{10}Be	$2_1^+ \rightarrow 0_1^+$	3367	100
	$2_2^+ \rightarrow 2_1^+$	2590	91
	$1_1^- \rightarrow 0_1^+$	5959	66
	$1_1^- \rightarrow 2_1^+$	2593	34
	$0_2^+ \rightarrow 2_1^+$	2812	65.7
	$0_2^+ \rightarrow 1_1^-$	219.2	34.3
	$2_1^- \rightarrow 2_1^+$	2896	100
^{11}Be	$1/2^- \rightarrow 1/2^+$	320.0	100
^{12}Be	$2_1^+ \rightarrow 0_1^+$	2107	100
	$0_2^+ \rightarrow 0_1^+$	511*	83
	$0_2^+ \rightarrow 2_1^+$	144	17
	$1_1^- \rightarrow 0_1^+$	2680	100

Table 2.1: Known gamma decays in ^{10,11,12}Be. The decays are taken from [Mat09, Shi07, Iwa00]. * The 511 keV stems from pair production.

CHAPTER 3

Transfer reaction theory

This chapter will give a short motivation for using transfer reactions to study the neutron rich beryllium isotopes. Furthermore the procedure for calculating both experimental and theoretical differential cross sections will be described.

3.1 Transfer reactions

Transfer reactions are a powerful tool to probe single particle excitations in a nucleus, making transfer reactions very useful when studying single particle behaviours of states. A particle, or cluster of particles, is transfered from one nucleus to another in transfer reactions, generally described like:

$$A + a \rightarrow B + b. \tag{3.1}$$

$$B = A \pm v. \tag{3.2}$$

$$b = a \mp v. \tag{3.3}$$

v is the transfered particle and B is the particle to be studied. The sign in eqn. 3.2 and 3.3 depends on the type of transfer (adding or removal) The populated states of the final nuclei (B, b) can be described by taking the ground states of the initial nuclei (A, a) and add or remove one particle (cluster). In the simplest picture, the two cores (the part of the two nuclei, that is not transfered, A and b) are assumed not to be affected by the transfer, hence the final states are completely determined by, which state the transfered particle (v) was in, and which state it ends up in. Any core excitations or multistep transfers are considered to be higher order contributions. b will be referred to as particles in this thesis, even though all four elements in eqn 3.1 are nuclei .

One neutron transfers ($v = n$ in eqn 3.1) will be studied in this thesis, both adding a neutron to the ^{11}Be (A) nucleus ((d,p)) and removal of one ((d,t)), leading to single neutron excitations of ^{12}Be and ^{10}Be (B) respectively. It has

already been stated in chapter 2 that both ^{11}Be and ^{12}Be to a large extent can be described as a ^{10}Be core and one or two neutrons respectively. This description works especially very well for ^{11}Be with its halo structure.

The one neutron removal experiment ((d,t)) could be used to investigate the ground state structure of ^{11}Be, which is known to be a linear combination of a s-neutron and a ground state ^{10}Be and a d-neutron and an excited ^{10}Be, eqn. 2.1 The loosely bound halo neutron should be easily transfered leaving the ^{10}Be core in either the ground state or the excited 2^+_1-state. This structure has been studied in various (d,p) and (p,d) reactions, for instance [Aut70, Zwi79, Win01]. Also the higher lying states of ^{10}Be will be populated in the (d,t) transfer, as it will be shown in chapter 7. This is done by knocking out one of the core neutrons from ^{11}Be leaving ^{10}Be in an excited state, section 2.4. The halo neutron will still be lightly bound (< 900 keV), for the four high lying states, making it possible to study the suggested halo structures of the 1^-_1- and 2^-_1-states [AK06].

A one neutron transfer reaction is also a very good tool for studying the mixing of the sd and the p shell, which occurs in ^{12}Be as described in section 2.3. All bound states in ^{12}Be contain some amount of a $^{11}\text{Be}_{\text{gs}}$ and one neutron in an *s*-, *p*- or *d*-shell. Especially the $|^{10}\text{Be}; 0^+_1\rangle\,|n; s_{1/2}\rangle\,|n; s_{1/2}\rangle$ component in the two 0^+-states is interesting in the study of the mixing of the states. This component should be strongly populated in a ^{11}Be(d,p)^{12}Be reaction. The main aim of the experiment is to determine the amount of this component in the two 0^+-states. This will be done by determining the spectroscopic factors, which will be described in section 3.4. Differential cross sections will be described first, starting with experimental ones.

3.2 Experimental differential cross sections

The differential cross section from an experimental point of view is a measure of the probability for a particle being emitted in a given solid angle. The differential cross section is given by:

$$\frac{\mathrm{d}\sigma}{\mathrm{d}\Omega}(\theta,\phi) = \frac{\dot{N}_b(\theta,\phi)}{I_A \cdot n_t}\frac{1}{\mathrm{d}\Omega}. \tag{3.4}$$

$\dot{N}_b$ is the number of reactions per unit time, I_A is the beam intensity, n_t is the particle density in the target and $\mathrm{d}\Omega$ is the solid angle. This can be rewritten as:

$$\frac{\mathrm{d}\sigma}{\mathrm{d}\Omega}(\theta,\phi) = \frac{1}{N_A \cdot n_t}\frac{N_b(\theta,\phi)}{\mathrm{d}\Omega}. \tag{3.5}$$

Here $\frac{N_b}{\mathrm{d}\Omega}$ is the number of outgoing particles for a solid angle and N_A is the total number of beam particles in the experiment.

The detection effiency of the setup has to be taken into account in order to convert the number of detected particles to the total number of outgoing particles in a solid angle. Simulations of the experiment are used to take the detection efficiency into account, rather than calculating the detection effiency for all solid angles,. The simulation will be described in detail in section 4.6, but the basic idea is to generate N_A^{sim} events uniformly distributed over 4π in center of mass. Only events hitting the detectors in the setup will be registered. The cross section can be rewritten using the simulated data:

$$\frac{\mathrm{d}\sigma}{\mathrm{d}\Omega}(\theta,\phi) = \frac{1}{n_t}\frac{N_{\mathrm{det}}^{\mathrm{exp}}(\theta,\phi)}{N_{\mathrm{det}}^{\mathrm{sim}}(\theta,\phi)}\frac{N_A^{\mathrm{sim}}}{N_A^{\mathrm{exp}}}. \tag{3.6}$$

Here sim stands for simulated data while exp stands for experimental data.

In order to calculate the cross section the five values in eqn. 3.6 need to be determined. n_t given by:

$$n_t = \frac{\rho \mathrm{d}t N_a}{M} N_d = \frac{1.00(5)\cdot 10^{-3}\mathrm{g/cm^2}\cdot 6.02\cdot 10^{23}/\mathrm{mol}}{16.1\mathrm{g/mol}}\cdot 2 = 7.5(3)\cdot 10^{19}/\mathrm{cm^2}. \tag{3.7}$$

Here ρ is the density of the target and dt is the thickness of the target, these two are combined and are given in table 4.1. M is the molar mass of the target and N_d is the number of reaction particles per molecule (two deuterons per ethylene molecule).

The number of beam particles for the experimental data (N_A^{exp}) is determined by rutherford scattering on ^{107}Ag, and is determined in section 6.4. The number of beam particles for the simulation is simply the number of simulated particles, and is given in section 4.6.

It has proven easier to determine the ratio $\frac{N_{\mathrm{det}}^{\mathrm{exp}}}{N_{\mathrm{det}}^{\mathrm{sim}}}(\theta,\phi)$ rather than the two numbers individually. This is done by fitting excitation energy spectra from simulated data to the experimental ones:

$$\begin{aligned} N_{\mathrm{det}}^{\mathrm{exp}} &= a N_{\mathrm{det}}^{\mathrm{sim}} \\ a &= \frac{N_{\mathrm{det}}^{\mathrm{exp}}}{N_{\mathrm{det}}^{\mathrm{sim}}}. \end{aligned} \tag{3.8}$$

This way the statistical uncertainties are taken into account by the fit. An example of such a fit is given in section 8.2

3.3 Theoretical differential cross sections

The theoretical differential cross sections are calculated using the program FRESCO [Tho06]. A short describtion of the theory behind the calculations will be given in this section. The theory has been taken from [Tho09], which contains a more detailed description. The theory will be described for a general reaction (eqn. 3.1). The section starts with scattering theory ($v = 0$, $a = b$ and $A = B$) before treating DWBA calculations for one-neutron transfer reactions ($v = n$). Real potentials will in the following sections be noted with a V, while complex potential will be noted with a U.

3.3.1 Optical model

The first step is to calculate the elastic scattering cross section. This is done using an optical model (OM). The optical model is the simplest of the calculations. Only the differential cross section from the elastic scattering channel is calculated, all other reaction channels are treated as loss of flux. The two particles are treated as inert particles. The only force considered is the force between them, given by the potential $U(R)$ (R is the relative distance). The potential is assumed to have a finite range ($U(r) = 0$ for $r > R_n$), and the differential cross section is determined by the distortion on the wavefunction of the incoming particle caused by the potential. The center of mass frame is chosen in a way, such that the incoming particle is described by a plane wave traveling in the z-direction:

$$\Psi_{inc}(\vec{k}, \vec{R}) = e^{ikz}. \tag{3.9}$$

The wavefunction will be distorted by the potential, and the asymptotic form of the outgoing wavefunction, outside the range of the potential, is of the form:

$$\Psi_{out}(\vec{k}, \vec{R}) = e^{ikz} + f(\theta, \phi)\frac{e^{ikR}}{R}. \tag{3.10}$$

The probability of finding the particle in a given angle, and hence the cross section is then given by the square of f:

$$\frac{\mathrm{d}\sigma}{\mathrm{d}\Omega}(\theta, \phi) = |f(\theta, \phi)|^2. \tag{3.11}$$

Normally there will not be any ϕ-dependence of f, and only a θ-dependency is assumed in the calculations. If the reaction involves charged particles, the potential will

consists of a coulomb part and a nuclear part, and f can be seperated into two:

$$f(\theta) = f_C(\theta) + f'(\theta), \tag{3.12}$$

where $|f_C(\theta)|^2$ is the Rutherford amplitude and $f'(\theta)$ is the nuclear f-value.

The f-value can be determined by solving the Schrödinger equation with the potential ($U(R)$) and the center of mass energy (E):

$$[\hat{T} + U(R) - E]\Psi(\vec{k}, \vec{R}) = 0. \tag{3.13}$$

It is assumed that the potential is spherical symmetric making it possible to seperate the angular and radial part of the wavefunction. Thus the wavefunction can be written as an expansion in polynomials of $\cos(\theta)$:

$$\Psi(\vec{k}, \vec{R}) = \frac{1}{kR}\Sigma_{L=0}^{\infty}(2L+1)i^L\chi_L(k,R)P_L(\cos(\theta)) \tag{3.14}$$

The radial functions $\chi_L(K,R)$ is given by the equation:

$$\left[\frac{-\hbar^2}{2\mu}\left(\frac{\mathrm{d}^2}{\mathrm{d}R^2} - \frac{L(L+1)}{R^2}\right) + U(R) - E\right]\chi_L(k,R) = 0. \tag{3.15}$$

μ is the reduced mass. The solutions to the equation for a finite range potential can be written in terms of Hankel functions and the S-matrix ($\mathbf{S}_L$):

$$\chi_L^{\mathrm{ext}}(k,R) = A_L\left[H_L^-(0,kR) - \mathbf{S}_L H_L^+(0,kr)\right]. \tag{3.16}$$

The nuclear f-value can be found by combining eqn. 3.14, 3.16 and eqn. 3.10:

$$f'(\theta) = \frac{1}{2ik}\Sigma_L(2L+1)(\mathbf{S}_L - 1)P_L(\cos(\theta)). \tag{3.17}$$

The S-matrix clearly plays an important part, and the calculation of the cross section is reduced to finding the $\mathbf{S}_L$-values. All $\mathbf{S}_L$-values are determined by matching the asymptotic form, and the derivatives, of eqn. 3.16 with eqn. 3.10. The values are uniquely defined by the interaction potential ($U(R)$). An important part of OM calculations is determining the right potential for the specific reaction. Calculations with different optical potentials will be attempted in this thesis. The shape and depths of the potentials will be described when used in section 8.3.1.

Two important features regarding the S-matrix should be noted. First of all, terms with $\mathbf{S}_L = 1$ will not contribute to the f-value (eqn. 3.17). This happens if the nuclear potential does not affect the radial wavefunction ($\chi_L^{\mathrm{in}} = \chi_L^{\mathrm{ext}}$). For each potential there exits an L_1-value for which $\mathbf{S}_{L\geq L_1} = 1$, hence it is not necessary to go to $L = \infty$ when calculating the cross section. Secondly, for a real potential the norm of S_L is unitary: $|S_L| = 1$, but if the potential is complex the norm will be less than one. This leads to a loss of flux. The real part of the potential describes the elastic scattering, while the imaginary part removes the flux going to other reaction channels. The deeper an imaginary part, the greater a loss.

3.3.2 Coupled channel calculation

Inelastic scattering is also seen in this experiment, populating the $1/2^-$-state (and the $5/2^+$-resonance) in ^{11}Be, chapter 7.

The scattering theory, described in the previous section, is still applicable in determining the inelastic scattering cross section. However, a few generalisations are needed. The final wavefunction might contain more than one state:

$$\Psi_{\text{out}}(\xi, \vec{R}) = \phi_1(\xi)\chi_1(\vec{R}) + \phi_2(\xi)\chi_2(\vec{R}). \tag{3.18}$$

The indices 1 and 2 refer to the two different states (1 being the ground state). Only two states are considered here, but the theory works for even more states. $\vec{R}$ is the relative coordinates between the two nuclei (A and a) and ξ is the internal coordinates of the states. The extra state will also lead to a modification of eqn. 3.10 and 3.11:

$$\Psi_{out}(\vec{k}, \vec{R}) = e^{i\vec{k}_{\text{initial}}\cdot\vec{r}}\phi_1(\xi) + f_1(\theta,\phi)\frac{e^{ik_1R}}{R}\phi_1(\xi) + f_2(\theta,\phi)\frac{e^{ik_2R}}{R}\phi_2(\xi). \tag{3.19}$$

$$\frac{\mathrm{d}\sigma_i}{\mathrm{d}\Omega}(\theta,\phi) = \frac{k_i}{k_{\text{initial}}}|f_i(\theta,\phi)|^2, \tag{3.20}$$

with $i = 1, 2$ in the last equation. The f-values are once again found by determining the outgoing wavefunction (eqn. 3.18) and matching it with eqn. 3.19. The outgoing wavefunction is given by the Schrödinger equation:

$$(E - \hat{H})\Psi_{\text{out}} = 0. \tag{3.21}$$

The total hamiltonian for the reaction is given by:

$$\hat{H} = \hat{H}_A + \hat{T} + U(\xi, \vec{R}). \tag{3.22}$$

$\hat{T}$ is the kinetic energy of the particle, $U(\xi, \vec{R})$ is the interaction potential and $\hat{H}_A$ is the hamiltonian for the internal system. The two states are eigenfunctions for the internal hamiltonian:

$$\hat{H}_A\phi_1(\xi) = \varepsilon_1\phi_1(\xi) \tag{3.23}$$

$$\hat{H}_A\phi_2(\xi) = \varepsilon_2\phi_2(\xi). \tag{3.24}$$

The potential of $\hat{H}_A$ is normally fitted to obey the two equations above. This leaves only the radial parts to be determined. The radial parts are determined by making projections onto the two internal states. Here it is done for the ground state (1):

$$\begin{aligned} 0 &= \phi_1^*(\xi)(E - (\hat{H}_A + \hat{T} + U(\xi, \vec{R})))\Psi(\xi, \vec{R}) \\ &= (E - \varepsilon_1 - \hat{T} - U_{11}(\vec{R}))\chi_1(\vec{R}) - U_{12}(\vec{R})\chi_2(\vec{R}), \end{aligned} \tag{3.25}$$

with:

$$U_{nm}(\vec{R}) = \int \phi_n^*(\xi)U(\xi, \vec{R})\phi_m(\xi)\mathrm{d}\xi. \tag{3.26}$$

The two projections lead to two coupled equations:

$$(E - \varepsilon_1 - K - U_{11}(\vec{R}))\chi_1(\vec{R}) = U_{12}(\vec{R})\chi_2(\vec{R}). \quad (3.27)$$

$$(E - \varepsilon_2 - K - U_{22}(\vec{R}))\chi_2(\vec{R}) = U_{21}(\vec{R})\chi_1(\vec{R}). \quad (3.28)$$

The coupled equations have to be solved to determine the radial wave function before matching eqn. 3.18 with eqn. 3.19, hence determining the differential cross sections. The coupling matrix elements (U_{nm}) plays an important part in the calculation. The two equations are decoupled if the two off-diagonal terms are zero, leaving to independent equation to be solved like in section 3.3.1. A potential, that can couple the two internal states, are needed. A spherical potential cannot couple states with different spin and parities, but a deformed potential can. A deformed potential has an angular dependency on the radius:

$$U(R, \theta', \phi') = U(R - \tilde{R}(\theta', \phi')). \quad (3.29)$$

This potential can be expanded on spherical harmonics for small deformations:

$$U(R, \theta', \phi') = U(R) - U'(R) \sum_{\lambda} \delta_\lambda Y_{\lambda 0}(\theta', 0). \quad (3.30)$$

$U(R)$ is the spherical part of the potential. δ_λ is called the deformation length and is a measure of the deformation of the potential. λ is the multipole of the deformation. $\lambda = 2$ is the quadrupole deformation of the potential. $U'(R)\delta_\lambda$ is the projection of the potential onto a given spherical harmonics:

$$U'(R)\delta_\lambda = \int U(R, \theta', \phi')Y_{\lambda 0}(\theta', \phi')\mathrm{d}\Omega. \quad (3.31)$$

The coupling matrix elements can be calculated by inserting eqn. 3.30 into eqn. 3.26. The diagonal terms are determined by the spherical part of the potential ($U(R)$), while the off diagonal terms, coupling the two states, are given by the expansions. It is clear, that only certain states can be coupled with a given deformation. The selection rules are:

$$|J_i - J_f| \leq \lambda \leq J_i + J_f \quad (3.32)$$

and

$$\pi_f = (-1)^\lambda \pi_i. \quad (3.33)$$

The selection shows, that a dipole deformation is needed to couple the $1/2^+$ and the $1/2^-$-states in ^{11}Be, and a quadrupole deformation to couple to the $5/2^+$-resonance. A quadrupole is also needed to couple the first two states in ^{10}Be. Both a dipole and a quadrupole deformation is used in the calculations, section 8.3.2.

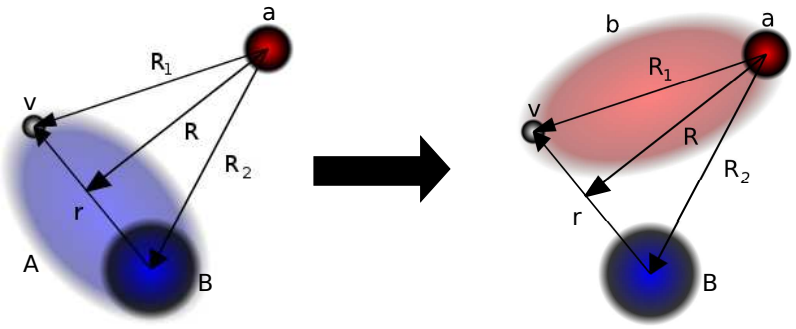

Figure 3.1: Drawing of the three body model for a one-neutron stripping reaction. Left is the initial situation were the valence particle is connected to the blue core, and the right is the final situation were the valence particle is transfered to the red core.

3.3.3 Distorted Wave Born Approximation

The theory for calculating transfer reaction cross sections is slightly more complicated than the scattering theory The basis is a three-body model with two cores (a, B) and a valence particle (v), fig. 3.1. Fig. 3.1 shows the initial (α) and final (β) situation of a transfer reaction, where the valence particle is removed from the initial nucleus (e.g. (d,t)). The three bodies all interact with each other, requiring three different potentials (V_{va}, V_{vB} and U_{aB}). A fourth potential is needed between the two particles in the initial (or final) situation (U_{aA}/U_{bB}). The differential cross section is given by the square of the transition amplitude.

$$\frac{d\sigma}{d\Omega} = \frac{\mu_\alpha \mu_\beta}{2\pi\hbar^2}\frac{k_\beta}{k_\alpha}|T(\vec{k}_\alpha, \vec{k}_\beta)|^2. \tag{3.34}$$

The transition amplitude is the probability of going from the initial situation (α) to the final (β), and is given by the potentials involved. The transition amplitude can be calculated in two ways called post and prior. The result is the same to first order in the Distorted Wave Born Approximation (DWBA). Details on the approximation will not be given here. The difference between the two ways, are the use of the potentials related to the initial or final state:

$$T^{prior} = < \chi_\beta \phi_b \phi_B | V_{va} + U_{aB} - U_{Aa} | \chi_\alpha \phi_A \phi_a >, \tag{3.35}$$

or:

$$T^{post} = < \chi_\beta \phi_b \phi_B | V_{vB} + U_{aB} - U_{Bb} | \chi_\alpha \phi_A \phi_a >, \tag{3.36}$$

The ϕ's are the internal wavefunctions of the particles. These are determined from the internal hamiltonians, like eqn. 3.23 and 3.24 (section 3.3.2). Here the potentials

are also scaled to produce the right eigenvalues. The χ's are the wave functions of the initial and the final state. These can also be found in coupled equations like the ones in eqn. 3.27 and 3.28:

$$(E_\alpha - \hat{T}_\alpha - U_{\alpha\alpha}(\vec{R}_\alpha))\chi_\alpha(\vec{R}_\alpha) = \int U_{\alpha\beta}(\vec{R}_\alpha, \vec{R}_\beta)\chi_\beta(\vec{R}_\beta)\mathrm{d}\vec{R}_\beta. \quad (3.37)$$

$$(E_\beta - \hat{T}_\beta - U_{\beta\beta}(\vec{R}_\beta))\chi_\beta(\vec{R}_\beta) = \int U_{\beta\alpha}(\vec{R}_\alpha, \vec{R}_\beta)\chi_\alpha(\vec{R}_\alpha)\mathrm{d}\vec{R}_\alpha. \quad (3.38)$$

The equations are found in a similar way as the ones in section 3.3.2, by taking the total Schrödinger equation and making a projection onto the two states. The transition amplitude can be written in integral form:

$$T = \int \mathrm{d}\vec{R}_\alpha \mathrm{d}\vec{R}_\beta \chi_\beta^{(-)*}(\vec{R}_\beta) I_{\beta\alpha}(\vec{R}_\alpha, \vec{R}_\beta)\chi_\alpha^{(+)}(\vec{R}_\alpha), \quad (3.39)$$

with:

$$I_{\beta\alpha}(\vec{R}_\alpha, \vec{R}_\beta) = < \phi_b\phi_B|V_{va} + U_{aB} - U_{Aa}|\phi_A\phi_a > . \quad (3.40)$$

These integrals can be calculated once the coupled equations are solved. All the calculations are done by FRESCO, and no further details will be given here.

3.4 Spectroscopic factors

An important parameter in transfer reaction experiments and the study of single particle structures of nuclei is the spectroscopic factor as mentioned earlier. The aim of the ^{11}Be(d,p)^{12}Be experiment described in this thesis is to determine the spectroscopic factor for each state populated in the reactions.

For many years spectroscopic factors have been interpreted as a measure of the amount of a given particle configuration of a state. As an example take the ground state of ^{12}Be, which is known as a linear combination of three different particle configurations:

$$|^{12}\mathrm{Be}; 0_1^+\rangle = \alpha\,|^{10}\mathrm{Be}; 0_1^+\rangle\,|2n; s_{1/2}^2\rangle + \beta\,|^{10}\mathrm{Be}; 0_1^+\rangle\,|2n; p_{1/2}^2\rangle + \gamma\,|^{10}\mathrm{Be}; 0_1^+\rangle\,|2n; d_{5/2}^2\rangle\,. \quad (3.41)$$

The factors (α, β, γ) can be determined by probing the different particle configurations individually, like the $\alpha\,|^{10}\mathrm{Be}; 0_1^+\rangle\,|2n; s_{1/2}^2\rangle$ in a ^{11}Be(d,p) reaction. The spectroscopic factor determined in the experiment is interpreted as the value α^2. The validity of this interpretation has been questioned in recent years. The spectroscopic factor is a quantity describing effects on the total volume of a nucleus, while direct reactions happen at the surface. Hence, modifications can occur especially when going away from stability [Pan97]. The large dependency on the potentials used

in the calculations has also been used to question the concept of spectroscopic factors [Jen11]. It has been proposed to use the absolute normalization constant (ANC) instead, which is a surface quantity and may describe reactions better, especially for exotic nuclei, [Tim10] and references therein. The validity of spectroscopic factors for exotic nuclei have been tested experimentally for various types of experiments, and while a strong effect is seen in nucleon knock-out reactions, no changes have been seen in one nucleon transfer reactions, [Lee11]. The debate is still ongoing, but it will not be covered in this thesis, and only spectroscopic factors will be determined.

The spectroscopic factor is defined as a scaling factor between an experimental determined differential cross section and a theoretical one:

$$S := \frac{\frac{\mathrm{d}\sigma}{\mathrm{d}\Omega}_{\text{experiment}}}{\frac{\mathrm{d}\sigma}{\mathrm{d}\Omega}_{\text{theory}}}. \tag{3.42}$$

From this definition and the description of the differential cross sections given in the two previous sections it is clear why the spectroscopic factor is equal to the norm squared for a given particle configuration. Both the theoretical and the experimental determined differential cross section is calculated for a given configuration of a state, like the $|^{10}\mathrm{Be}; 0^+_1\rangle\,|2n; s^2_{1/2}\rangle$- configuration of the 0^+-states in ^{12}Be. Only one particle configuration for each state can be probed by a given transfer reaction. This is easily seen by adding a neutron to the ground state of ^{11}Be, the only 0^+-configuration possible is the $s^2_{1/2}$. The coupling between the initial and the final state is only non-zero for the given configuration, hence the experimental differential cross section is proportional to:

$$\frac{\mathrm{d}\sigma}{\mathrm{d}\Omega}_{\text{experiment}} \propto \left|\alpha\,\langle 2n; s^2_{1/2}|\,\langle {}^{10}\mathrm{Be}; 0^+|\,U\,|\text{initial}\rangle\right|^2 = |\alpha|^2 \tag{3.43}$$

Initial is the initial configuration with the deuteron and ^{11}Be and U is the transition potential.

For the theoretical calculation it is a choice made in the parameters. The theoretical cross section is calculated with the assumption, that the state is completely described by a given particle configuration corresponding to

$$|^{12}\mathrm{Be}; 0^+\rangle_{\text{theory}} = |^{10}\mathrm{Be}; 0^+_1\rangle\,|2n; s^2_{1/2}\rangle\,, \tag{3.44}$$

and the differential cross section becomes proportional to:

$$\frac{\mathrm{d}\sigma}{\mathrm{d}\Omega}_{\text{experiment}} \propto \left|\langle 2n; s^2_{1/2}|\,\langle {}^{10}\mathrm{Be}; 0^+|\,U\,|\text{initial}\rangle\right|^2 = 1 \tag{3.45}$$

The proportionality constant is the same, hence from the definition of the spectroscopic factor:

$$S = |\alpha|^2\,. \tag{3.46}$$

This is valid if the reaction is a single step process, if the transfer is done in a two step process, for instance where the initial nucleus is excited, new configurations can be populated. Taking again the 0^+-states of ^{12}Be. If ^{11}Be is excited to the $1/2^-$ state, the single particle configuration populated is the:

$$|^{10}\mathrm{Be}; 0_1^+\rangle\,|2n; p_{1/2}^2\rangle$$

configuration. These effects requires a deeper theoretical analysis and are not discussed further in this thesis.

CHAPTER 4

The experiment

A description of the experimental procedure will be given in this chapter. Including the experimental setup, the detectors and the production of our radioactive beam. Furthermore a short description of the simulation will be given.

4.1 Performing a transfer reaction experiment

The motivation for studying neutron rich beryllium isotopes, especially ^{12}Be, in a transfer reaction should be clear from the last two chapters. Performing a transfer reaction involving a radioactive isotope is a complicated task though. The short lifetime of ^{11}Be ($\tau = 19.9\,\mathrm{s}$) makes it impossible to use as a target. Instead the reaction is done in inverse kinematics using a radioactive ion beam (RIB) of ^{11}Be and a deuteron target. This requires both a RIB facility, to produce a ^{11}Be beam and a foil containing deuterons. Deuterons are stable and foils containing deuterons are easily accessible. A plastic foil (CH_2), where the protons are exchanged with deuterons, is used in this experiment. Several RIB facilities, that can produce low energy ^{11}Be beams, exists today. The ISOLDE facility at CERN, Switzerland, is used in this experiment. The experiment is performed by directing the ^{11}Be beam onto the deuteron target and two (or more) particles goes out of the target after the reaction. The light particles (p, d or t) are detected and used to determine the differential cross section, while the heavy fragments are sent to a beam dump. Silicon detectors are needed to detect the outgoing charged particles. Gamma detectors are also used, in this experiment, to separate the individual states in the heavy nuclei. All the components will be described individually in this chapter.

The experiment is performed as a series of small runs. A run ranges from minutes to a few hours in time. A data file containing the signals from the detectors are created for each run. The data from all the runs are analysed together, except when determining the fluctuations in the beam, chapter 6. During the experiment small runs with other targets are performed, section 4.4. These extra runs are used to improve the analysis.

4.2 ISOLDE

The radioactive ^{11}Be beam was produced at ISOLDE, CERN. ISOLDE was one of the first facilities at CERN, and one of the first low energy RIB facilities in the world. The ISOLDE facility is shown in fig. 4.1. The beams are produced at one of the two primary target stations, one connected to the General Purpose Separator (GPS), which was used in this experiment, and one connected to the High Resolution Separator (HRS). The beam production is done through fragmentation of heavy ions. A Tantalum (Ta) target was used for the ^{11}Be production. High energy protons ($\sim$ 1.4 GeV) from the PS booster hit the primary Ta target creating unstable nuclei which decay through emission of several light isotopes, including ^{11}Be. The target is heated to temperatures between 700°C and 1400°C making the fragments evaporate from the target and diffusing onto an ion source. The created nuclei are laser ionised creating a positive ion, which can be accelerated through high voltage. The ions are accelerated up to 60 keV and sent to one of the two separators (GPS or HRS). The separators are a series of bending magnets, one for the GPS and two for the HRS (fig. 4.1), which separate the accelerated beam particles according to their masses. Only the low-energy ^{11}Be particles go through the separator and into the ISOLDE experimental hall. The rest of the emission fragments are stopped in the separators.

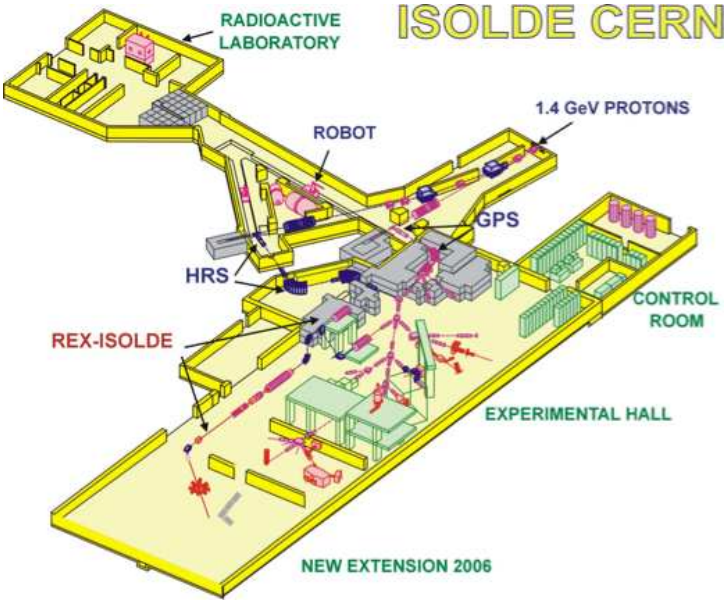

Figure 4.1: A drawing of the ISOLDE facility. The facility is divided into two parts, the target area (top part) and the experimental area (bottom part).

4.3 REX-ISOLDE

The ^{11}Be beam from the GPS has to be accelerated further, in order to get a beam energy high enough to induce nuclear reactions. This is done at the REX-ISOLDE postaccelerator [Kes03]. Fig. 4.2 shows a diagram of the postaccelerator. The idea of the REX is to create highly charged nuclei, which can be accelerated through a short linear accelerator. The ability to use a short LINAC, combined with the placement outside of the highly radioactive target area of ISOLDE, is the strength of REX-ISOLDE.

The acceleration is done in three steps. First the ions are trapped, bunched and cooled in a penning trap (REXTRAP). The cooled ions are afterwards sent to an electron beam ion source (REXEBIS). The EBIS creates highly charged ions using a magnetically compressed electron beam [Cur05]. ^{11}Be is totally stripped creating $^{11}Be^{4+}$. The REXTRAP uses a noble gas to cool the beam. Thus the bunched beam needs to be separated once again before being accelerated, which is done through two bending magnets. The noble gas used is neon, and the bending magnets are only able to separate particles with different q/A, hence the separator cannot distinguish $^{11}Be^{4+}$ and for instance $^{22}Ne^{8+}$. A neon gas without ^{22}Ne had to be used in the REXTRAP. A purified ^{20}Ne gas was used as a cooler gas reducing the ^{22}Ne contamination in the final beam to less than 1 %. Last step is the acceleration of the beam. The acceleration is done in a LINAC, that is able to accelerate the beam up to 3 MeV/u. A beam energy of 2.8 MeV/u was used in the experiment. After the reacceleration the beam is directed, through a bending magnet, onto the reaction target placed at the MINIBALL station.

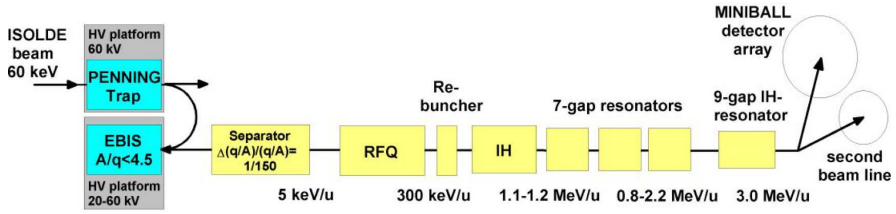

Figure 4.2: Diagram of the REX post accelerator. The low-energy beam from ISOLDE enters the penning trap, where it is bunched and sent to the EBIS. The EBIS strips the beam particles and send them through a q/A separator to the LINAC. The LINAC consists of four different types of cavities, that can accelerate the beam up to 3 MeV/u.

4.4 Targets

Five different targets were used in the experiment. Table 4.1 shows the five targets along with a short description of the purpose of the target. A foil of deuterated polyethylene (CD_2) was used as the primary target in the experiment. The deuterated polyethylene was used to produce the ^{11}Be+d reactions investigated in this thesis. Unfortunately the target contained a significant amount of carbon and a small fraction of protons. It is not possible to create a pure CD_2 target and a few percent contamination of CH_2 is expected. ^{11}Be can react with both the carbon and the protons in the target producing protons, deuterons and fusion products, which will act as a background on the real ^{11}Be+d events. To determine and remove the background a few runs on a pure carbon target as well as on a regular polyethylene (CH_2) target were performed throughout the experiment. The effect of the background is described in chapter 7. The reactions from the two background targets could be used to investigate the reactions of ^{11}Be on both carbon and protons as well, and indeed the (p,p) and (p,d) reactions are studied in chapter 9.

The total number of ^{11}Be particles in the experiment is needed in order to determine the differential cross section, eqn. 3.6. The beam intensity is determined through reactions with known cross sections, like Coulomb scattering. The low Z-value of the two nuclei (Z= 4 and 1) makes the (d,d) scattering mainly nuclear and the channel cannot be used to determine the beam intensity. Instead a silver target was used. Short, beam intensity, measurements were performed regularly during the experiment. This provides the beam intensity at a given time in the experiment. The beam intensity will fluctuate during the days of an experiment, and this has to be taken into account to get the right scaling of the angular distributions, hence regular intensity measurements are needed. The beam measurement and the calculation of the total number of ^{11}Be in the experiment will be described in section 6.4.

The last target was a stopper foil made of a thick aluminum foil. The target was used to create a ^{11}Be gamma source. The ^{11}Be particles will be stopped in the target and afterwards β-decay to excited states in ^{11}B. The excited ^{11}B will then gamma decay producing gammas with energies up to 8 MeV. This ^{11}Be source is used to both calibrate and determine the high energy detection efficiency of the MINIBALL, described in section 5.7.

4.5 The detector setup

Two types of detectors were used in the experiment, silicon detectors for charged particles and germanium detectors for gammas. A standard setup for transfer reaction experiments at ISOLDE has been developed combining the MINIBALL array [Ebe01]

Target	Thickness	Purpose
CD_2	1.00(5) mg/cm^2	Primary target. ^{11}Be + d reactions.
^{107}Ag	1.9(1) mg/cm^2	Beam intensity measurement through Coulomb scattering.
CH_2	1.1(1) mg/cm^2	Used to determine the background from reactions on protons.
C	1.50(5) mg/cm^2	Used to determine background from fusion products of ^{12}C+^{11}Be.
Al	$\sim$ 200 μm	Energy and efficiency calibration of MINIBALL.

Table 4.1: The five different targets used in the experiment.

and the T-REX setup [Bil12]. A picture of the setup is seen in fig. 4.3.

The MINIBALL is an array of 24 germanium detectors placed in eight clusters. A Ge-cluster is seen in fig. 4.5. The clusters are placed on a movable frame, making it possible to adjust the position of the individual clusters to optimize the angular coverage for each experiment. The MINIBALL has an energy resolution down to 10 keV, which is a factor of 20 better than the resolution of the charged particle detectors used in this experiment.

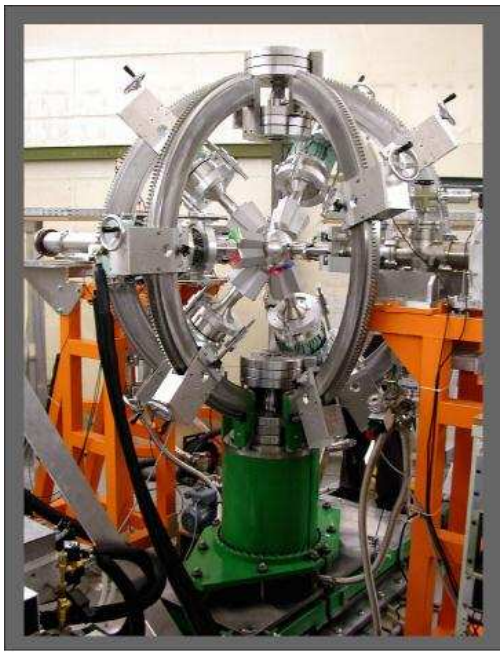

Figure 4.3: A picture of the MINIBALL setup. The eight germanium cluster is placed on an adjustable frame making it a versatile setup.

The T-REX setup used for charged particle detection consists of 16 silicon detectors placed in a barrel like configuration, fig. 4.4. The barrel has four sides and two end-caps. The four sides are made from eight square detectors two on each side. The barrel is designed to have two end-caps made from four annular detectors (AD) each. Each AD cov-

ers almost a quarter of the end-cap. Both end-caps have a hole in the centre to let the beam and heavy fragments slip through. The end-cap covering the very backward angles was missing in the experiment. The T-REX covers nearly all angles from 8° to 152° in the laboratory system, even without the backward end-cap [Bil12]. The target is placed in the middle of the setup (red dot in fig. 4.4) using a target ladder. The four detectors making up the forward side of the barrel are shielded with a 11.57 μm thick mylar foil in order to protect the detectors from heavy fragments. Light particles pass through the foil while heavy particles like beryllium isotopes are stopped. The mylar foil lowers the resolution of the charged particle data due to straggling in the foil. Furthermore it increases the low energy limit for charged particles to be detected.

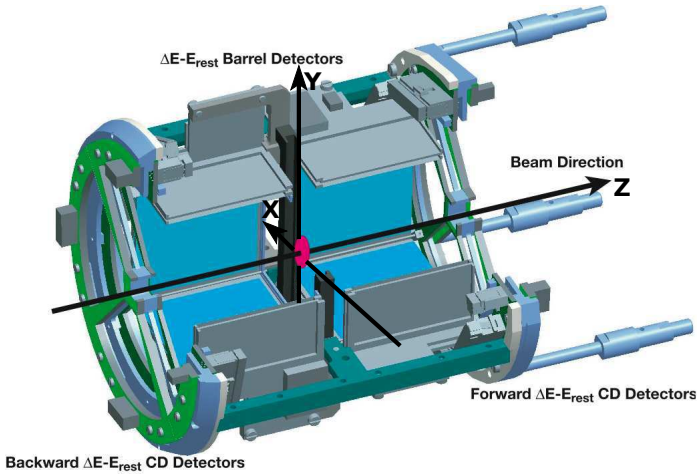

Figure 4.4: A drawing of the T-REX setup including the laboratory frame described in section 5.2. The target is represented by a red dot. Half of the detectors on the top and left right side is omitted to give a view inside the detector. The beam is assumed to follow the z-direction.

4.5.1 Silicon detectors

The silicon detectors in the T-REX are telescope detectors with a thin detector (ΔE-detector) in front of a thick one (E-detector). The advantage of two detectors in telescope is the ability to make particle identification, described in section 7.2.1. Ideally the particles go through the front detector and stop in the back one, hence the thinner a front detector the better. The combined energy deposited in the two detectors cor-

responds to the total energy of the incoming particle. The thickness of the ΔE- and E-detectors can be seen in table 4.2.

The momentum vectors of the particles are required to calculate excitation energy spectra, chapter 7. Hence the position within the detectors of the particles have to be determined as well. This is done by using segmented detectors as ΔE-detectors. The thick E-detectors are only used for measuring the energy and each one consists of only one large pad (the E-detectors are sometimes called pad-detectors).

The T-REX setup consists of two types of ΔE-detectors with different segmentations. The eight detectors making up the side of T-REX are square detectors with an active area of 50x50 mm^2. The detectors are position sensitive detectors (PSD). The front side of a PSD is divided into 16 strips while the backside is one big pad (not to be confused with the E-detector). The PSD has one readout for each strip on the front-side and one for the backside. The backside readout gives the total energy deposited in the detector (ΔE) while the front-side readouts give a signal indicating the position in the corresponding strip. The front sides of the detectors have a resistant layer and a readout in one end of each strip. If a particle hits a strip close to the readout the current lost in the resistive layer is small and the front and back side readout are the same. If a particle hits a strip in the end away from the readout all current is lost in the resistive layer. Hence the signal from the front side ranges from 0 in one end to ΔE in the other, providing the position, section 5.4.

The annullar ΔE-detectors are divided into 24 strips (front side) and 16 rings (backside). The position is determined by the strip and ring number, section 5.2. The energy is determined from either the energy signal in the ring or the strip. An energy difference between the two signals of less than 500 keV is required for signals to be accepted as a true event.

Place in T-REX	Detector	Thickness [μm]
Barrel side	PSD	140
	Pad	1000
End-cap	AD	500
	Pad	500

Table 4.2: Detector types and thickness for the silicon detectors in T-REX

Details on the electronics will not be given in this thesis, for more information see V. Bildstein et al. [Bil12]. In short terms the signals from the detectors are sent through a preamplifier, an amplifier and an analog to digital converter (ADC). The ADC number, the ADC channel number and the value of the signal (channel number

in spectrum) are afterwards stored in data files. The ADC number and the ADC channel number provide information on the detector number and signal type (position or energy), while the channel number of the signals provide the value of either the position or the energy. The channel numbers have to be converted to either position or energy, which requires a calibration, chapter 5.

4.5.2 Germanium detectors

The MINIBALL setup consists of 8 clusters, each cluster contains three germanium detectors (fig. 4.5), and each detector is divided into six segments giving the MINIBALL a high angular resolution. The high angular resolution is needed in order to make doppler correction of the gammas, section 7.2.3.

Each germanium detector has seven readouts, one for each of the six segments and one for a common core. The core gives the total energy deposited in the detector while the segment readouts give the energy deposited in each segment. As the gamma ray are scattered in the detector, the energy of the gamma can be divided between several segments, hence the core signal is used as the energy signal and the segment signals are used to determine which segment the gamma hits, hence determining the position within the detector. If the energy is divided between several segments, the segment with the largest energy signal is used as position. A measurement of the position within a segment is not needed in this experiment.

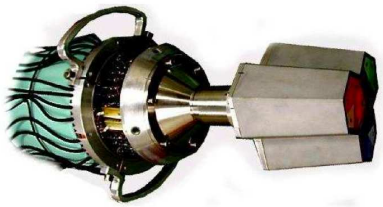

Figure 4.5: A picture of a MINIBALL cluster with the three segmented germanium detectors. The detectors are the three hexagons to the right. Each detector has six triangular segments. The part to the left is electronics and a container for liquid nitrogen.

4.6 Simulation

The lack of 4π-coverage and the non spherical structure of the T-REX makes the detection efficiency for a given solid angle dependent on the angle. Rather than calculating the detection efficiency for all angles a simulation of the experiment is made. The simulation code is written by V. Bildstein [Bil10] using Geant4 [Ago03] and the g4miniball package [Boi09]. The simulation can simulate both transfer and scattering reactions. N (10^6 is used in this experiment) reactions are produced with a flat dis-

tribution in center of mass. The direction and energy in the laboratory frame of the outgoing particles are determined from kinematics. The number of the detector and strip, the particle hits (if any), is afterwards determined, and a root-file, containing all information regarding each detected particle, is generated. The simulated data can afterwards be analysed using the same program as the experimental data.

The flat distribution ensures, the number of recorded simulated particles, in a given angle, is only dependent on the detection efficiency of the setup and not the angular distribution. The number of detected particles in a given angle in the experiment is, on the other hand, dependent on the angular distribution of the reaction and the detection efficiency. The angular distribution of a reaction can be determined by comparing the number of experimental detected particles with the number of detected particles in the simulation, section 3.2.

The detailed structure of the beam can be set in the simulation, including the spread in energy, the reaction depth in the target, the shape and offset of the beam, and the angle and divergence of the beam. This is used to test and determine the detailed structure of the experimental beam in chapter 6 and to improve the simulations used to determine the angular distributions.

The simulations are also used in an attempt to determine the width of the lowest lying resonance known in ^{12}Be, section 10.3.

CHAPTER 5

Calibration

In this chapter, the calibration of the silicon and germanium detectors will be described. Calibration of both the energy and the position signals are performed.

5.1 Signals from the detectors

The momentum vector for one of the outgoing particles is required to determine the reaction type of each event. Four parameters ($[x, y, z, E]$) can be measured as described in the last chapter, but the signals require calibration.

The energy and position calibration for the silicon detectors are done using an α-source, described in section 5.3 and 5.4. The α-particles are stopped in the ΔE-detectors and the light particles from the reactions of ^{11}Be on deuterons are used to calibrate the pad-detectors (E-detectors), section 5.5. An ^{152}Eu source and the ^{11}Be beam are used for the energy calibration of the germanium detectors. The positions of the germanium detectors are determined using a stable beam of ^{22}Ne on a deuteron target, all this is described in section 5.6.

Furthermore the detection efficiency of the MINIBALL has to be determined. The efficiency has to be taken into account when producing gamma gated spectra, section 7.2.3. The MINIBALL efficiency is determined by K. Wimmer [Wim10a] and will only briefly be described at the end of this chapter.

5.2 The laboratory frame

The position ($[x, y, z]$) of an event should be given relative to the reaction point. The laboratory frame is defined as shown in fig. 4.4. Origin is placed in the center of the target, which is also the center of the T-REX. The z-axis is placed parallel to the PSD's and perpendicular to the AD's. The y-axis is the vertical axis and the x-axis the horizontal one perpendicular to the z-axis.

The beam is assumed to be moving along the z-axis and all reactions are assumed to happen in origin. This assumption will be investigated in chapter 6 where the structure of the beam will be determined. With this assumption the direction (angle

and azimuthal angle) of the outgoing particle can be determined using the coordinates of the event.

The position of an event in the lab frame is determined in two steps. First the position in the detector (*pos*) is calculated, using the formulas described in the next sections. Afterwards the position is transformed from the detector frame to the laboratory frame. The transformation requires knowledge of the individual detectors position in the laboratory frame. The positions of the silicon detectors are determined from the construction of the T-REX and the transformations are given by:

$$x_{\mathrm{PSD}} = 50\,\mathrm{mm}(pos - 0.5)\cos(\frac{\pi}{2}N_{\mathrm{detector}}) + 29\,\mathrm{mm}\sin(\frac{\pi}{2}N_{\mathrm{detector}}) \quad (5.1)$$

$$y_{\mathrm{PSD}} = 50\,\mathrm{mm}(pos - 0.5)\sin(\frac{\pi}{2}N_{\mathrm{detector}}) + 29\,\mathrm{mm}\cos(\frac{\pi}{2}N_{\mathrm{detector}}) \quad (5.2)$$

$$z_{\mathrm{PSD}} = \pm(8\,\mathrm{mm} + 3.125\,\mathrm{mm}N_{\mathrm{strip}}) \quad (5.3)$$

$$\theta_{\mathrm{AD}} = \arctan\left(\frac{9\,\mathrm{mm} + 2\,\mathrm{mm}N_{\mathrm{ring}}}{63\,\mathrm{mm}}\right) \quad (5.4)$$

$$\phi_{\mathrm{AD}} = -59.3411\,\mathrm{mrad}N_{\mathrm{strip}} + 712.09\,\mathrm{mrad} + \frac{\pi}{2}(1 - N_{\mathrm{detector}}). \quad (5.5)$$

The detector numbers (N_{detector}) are counted clockwise looking towards the beam starting with 0 for the top detector. The sign on the z_{psd} component is dependent on wether it is a detector before or after the target. A transformation from (x, y, z) to (θ, ϕ), or the other way, is easily done.

The positions of the germanium detectors have to be determined individually, which will be done in section 5.6.2.

5.3 Annular Detectors (AD)

First the four segmented ΔE-detectors that make up the end cap of the T-REX barrel are calibrated. The calibration is performed by placing an α-source at the target position. The α-source consists of four emitters (^{148}Gd, ^{239}Pu, ^{241}Am and ^{244}Cm) with α-energies 3182.7 keV, 5156.6 keV, 5485.6 keV and 5804.8 keV.

The signals from the AD's are merged together two and two in the ADC's to reduce the number of ADC channels. The top and left AD, and the bottom and right share the same ADC numbers and the same ADC channel numbers. Each pair has a total of four ADC channels rather than 40 (one for each strip (24) and ring (16)). Instead the strip and ring number are stored in an address signal (2 ADC channels: a strip and a ring number). The energy signals of all strips and rings are stored in two other ADC channels, one for the front (strips) and for the back side (rings). The energy signal for a strip can be determined by making a gate in the address signal.

The address signal contains 32 peaks divided into two groups, fig 5.1. Each peak represents a strip or ring, and each group corresponds to a detector. Channels from

400 to 700 represents hits in either the top or bottom detector (dependent on the ADC number) and channels 1000 to 1300 represents hits in the left or right detector. The mean value of each peak (C_N) is determined and a gate is made to determine the strip/ring number:

$$N \in [C_N - 6, C_N + 6]. \tag{5.6}$$

N is the strip/ring number.

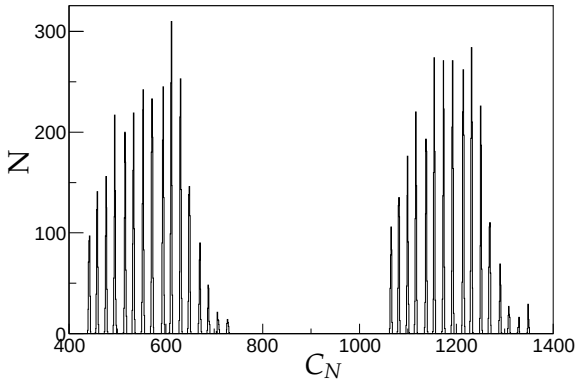

Figure 5.1: The histogram showing the address from an ADC. Each peak represents a strip in the top (400-700) or left AD (1000-1400).

The energy calibration is done with a simple linear relation:

$$\Delta E = a_{\Delta E}(C_{\Delta E} - b_{\Delta E}). \tag{5.7}$$

C being the channel number in the spectrum. Fig. 5.2 shows a linear fit using the four known energies from the α-source. The energy calibration is performed for each strip and ring in each detector. A channel number spectrum is generated for each strip/ring by using the address gates, eqn. 5.6. The channel numbers corresponding to the four α-energies are determined using a gaussian fit to the four peaks in the channel number spectra, not shown here.

5.4 Position Sensitive Detectors (PSD)

The position sensitive detectors, that make up the four sides of the T-REX barrel are described in section 4.5.1. The PSD's have 17 readout each, one for each of the 16 strips providing the position in the strip, and one from the rear side providing the energy, section 4.5.1.

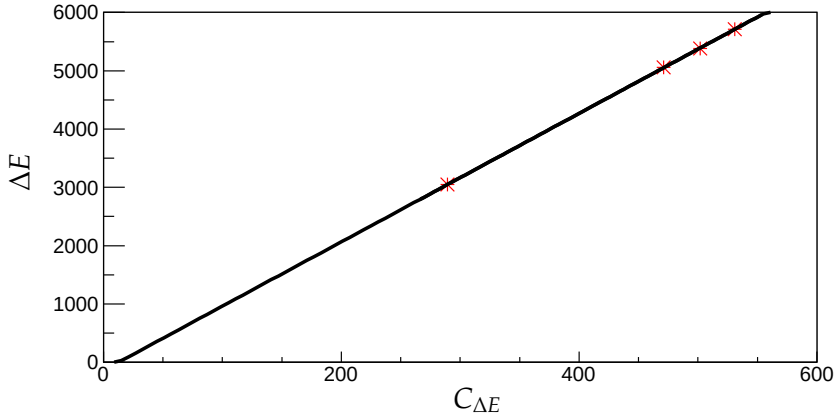

Figure 5.2: A linear fit to the four α-energies for strip 0 in the top AD.

The resistive front layer provides a signal ranging from 0 to ΔE dependent on the position in the strip. The position signal is divided by the total energy, making the range 0 to 1 to generate a common scale of the position signal for each event. The calibration of the position is then:

$$Pos = \frac{a_{\text{pos}}(C_{\text{pos}} - b_{\text{pos}})}{\Delta E}. \tag{5.8}$$

C_{pos} is the channel number for the position and ΔE is the calibrated energy signal. It is clear that the position signal is dependent on the energy signal. Unfortunately the energy signal is also dependent on the position signal as shown in fig. 5.3. The figure shows the backside signals as a function of the front-side signals for two PSD's. The total detected energy is reduced for the particles dependent on the position in the strip, due to the resistivity in the detector. The relation between the channel number and the energy is no longer linear but given by:

$$\Delta E = a_{\Delta E}\left(\frac{C_{\Delta E} - b_{\text{tilt}}}{a_{\text{tilt}}(1 - Pos) + 1} - b_{\Delta E}\right). \tag{5.9}$$

Here Pos is the calibrated position signal and $C_{\Delta E}$ is the energy channel number. All a's and b's are numbers to be determined in the calibration (tilt refers to the tilting of the lines in fig. 5.3). The strong dependency between the energy and the position signal makes an iterative process necessary to calibrate the PSD detectors.

The calibration is further complicated in the four forward PSD's due to the Mylar foil in front of them, section 4.5.1. The energy loss of the α-particles in the Mylar is dependent on the incoming angle giving a further dependency between the energy

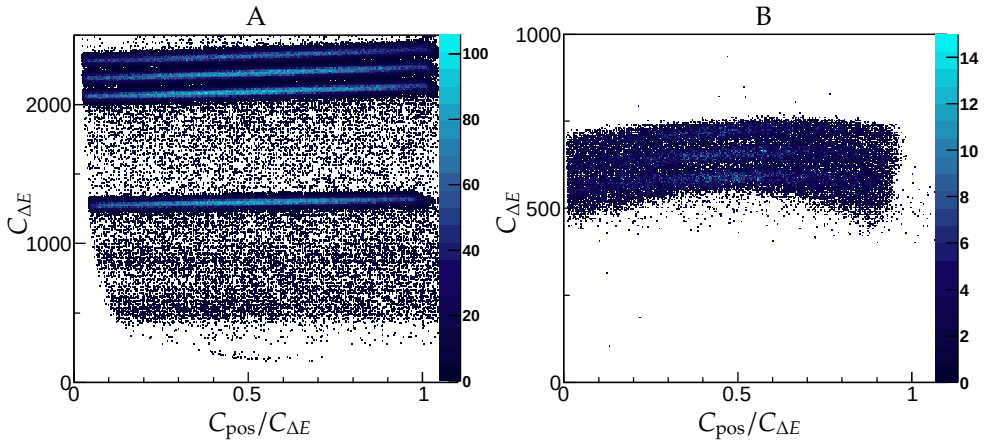

Figure 5.3: Two plots showing the strong dependency between the position signal and the energy signal in the backward (A) and forward (B) PSD's.

and the position, fig. 5.3B. The three peaks are bent, rather than straight like in the backward PSD's. Furthermore, only three peaks are detected. The α-particles with the lowest energy are stopped in the Mylar foil.

5.5 Pad detectors (E-detectors)

The pad detectors only provide an energy, hence no position calibration is done.

The energy calibration is inspired by the $\Delta E - E$ plots used to distinguish protons from deuterons etc. in section 7.2.1. A clear relation, between the energy deposited in the ΔE- and the E-detector, exists. The relation is dependent on the particle type, the energy of the particle and the angle between the particle and the detector (θ_{det}). The energies of the α's from the α-source used to calibrate the energy of the ΔE-detectors are not strong enough to enter the pad detectors. Instead particles from the reactions of ^{11}Be on deuterons are used. The reaction produces both protons, deuterons and tritons. Spectra of the channel numbers are made gated on various intervals in θ_{det} (strip number) and ΔE. The spectra contain two or three peaks corresponding to protons, deuterons and tritons, or one or two of them. Fig. 5.4A shows two pad energy spectra taken from the top detector strip 0 with the following gates:

$$1.95\,\text{MeV} \leq \Delta E \leq 2.05\,\text{MeV} \tag{5.10}$$

$$2.95\,\text{MeV} \leq \Delta E \leq 3.05\,\text{MeV} \tag{5.11}$$

A strong peak at 0.5 MeV (protons) and a weak one at 1 MeV (deuterons) are seen for

the spectrum with a $\Delta E \approx 2\,\text{MeV}$ gate. Three peaks are seen in the spectrum with a $\Delta E \approx 3\,\text{MeV}$ gate representing the three particles. The shifts in energy of the proton and deuteron peaks between the two spectra are clearly seen. A third gate around $\Delta E \approx 4\,\text{MeV}$ is made as well. Energy spectra are generated for the three gates in all strips in each detector and as many peaks as possible are determined for each spectra.

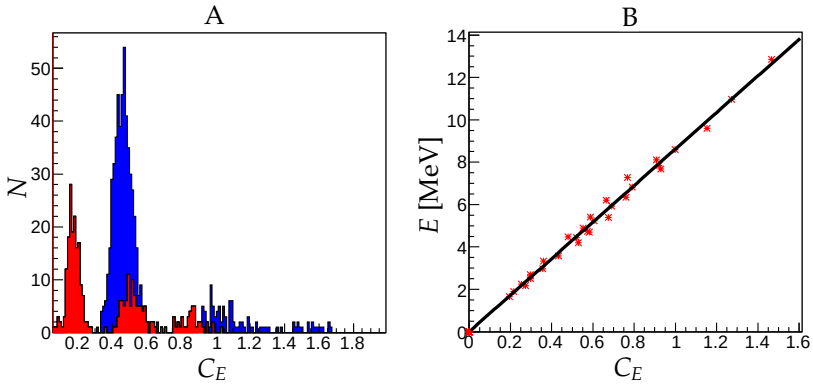

Figure 5.4: (A) Two histograms of channel numbers made with two gates on the ΔE-signal; Red: $\Delta E \approx 3\,\text{MeV}$, Blue: $\Delta E \approx 2\,\text{MeV}$. All three particles are seen at 3 MeV, only the two lightest are seen at 2 MeV. (B): A linear fit to all the identified peaks in one of the four forward PSD's.

The corresponding energies have been determined using SRIM [Zie83], and a linear fit is made using peaks from all gates and strips in a detector, fig. 5.4B. The large uncertainty in the channel number for each peak in, fig. 5.4A, is compensated by the large amount of points in fig. 5.4B, and a linear relation is clear.

5.6 Germanium detectors (MB)

The 24 germanium detectors in the MINIBALL all have six segments and a core. The core gives the total energy in the detector, and the segments provides a better determination of the position of the detected gamma. Pulse shape analysis could be used to determine the position of the gamma in the segments [Des05]. This is not done in this analysis, the angular resolution given by using the centre of the segments is sufficient to make a doppler correction of the gammas, chapter 7.

5.6.1 Energy calibration

The gammas from the experiment ranges in energy from 300 keV to 6 MeV, requiring a long energy range for the germanium detectors. Thus the energy calibration is made with two sources. A low energy source (^{152}Eu) providing gammas from 121 keV to 1400 keV. The ^{152}Eu source was placed in the target ladder like the α-source in the previous sections. The high energy source was ^{11}Be produced by the REX-ISOLDE and stopped in an aluminum target, section 4.4. ^{11}Be provides gammas from 2100 keV to 6800 keV [Mil82]. The gamma energies for the two sources are given in table 5.1. The corresponding channel numbers are found by gaussian fits in channel number spectra. An energy calibration is made for each segment and core using a linear relation between the channel number and the energy.

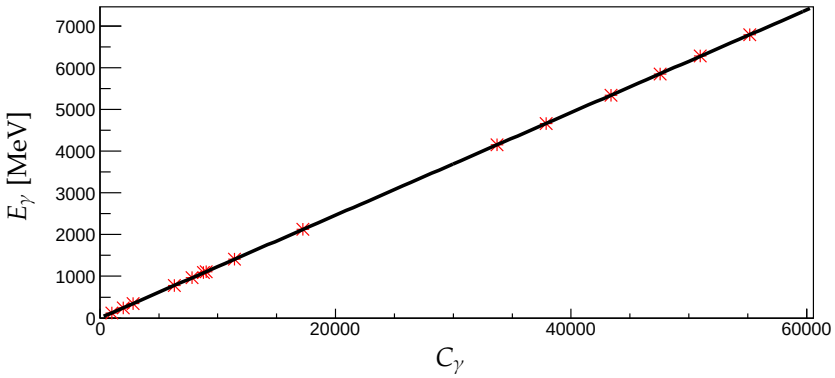

Figure 5.5: A linear fit to the 16 gamma energies for one of the germanium cores.

5.6.2 Position calibration

The position of each segment relative to the target has to be determined. This is done using gammas from a d(^{22}Ne,p)^{23}Ne reaction. A proton gated gamma spectrum is made for each segment and the gammas from the strongest line is identified, fig. 5.6. The strongest line is known to be the $1/2^+ \rightarrow 5/2^+$ transition in ^{23}Ne with a gamma energy of $E_{^{23}\mathrm{Ne}} = 1016.85$ keV. The angle of the segments can then be determined from the doppler shift:

$$\theta = \arccos\left(\frac{1}{\beta}\left(1 - \frac{E_{^{23}\mathrm{Ne}}}{\gamma E'}\right)\right). \tag{5.12}$$

E' is the doppler shifted gamma energy, corresponding to the mean value of the peak (fig. 5.6) and β and γ are the relativistic factors determined from the energy and angle

^{152}Eu	^{11}Be
121.781	2124.47
244.698	4154.90
344.279	4665.90
778.904	5340.47
964.079	5851.47
1085.87	6278.81
1408.01	6789.81

Table 5.1: E_γ for the gamma sources used to calibrate the germanium detectors. All values are in keV.

of the proton:

$$\gamma = \frac{T_A + Q - T_b - T_B + m_B c^2}{m_B c^2} \tag{5.13}$$

$$\beta = \sqrt{1 - \frac{1}{\gamma^2}}. \tag{5.14}$$

A, b and B refer to eqn. 3.1 and are here ^{22}Ne, p and ^{23}Ne respectively. T_B is calculated from momentum conservation (eqn. 7.5).

5.7 MINIBALL efficiency

The last component to be determined for the detectors is the MINIBALL detection efficiency. The efficiency calibration of the MINIBALL is done with four different gamma sources, ^{152}Eu, ^{60}Co, ^{207}Bi and ^{11}Be. The activity is known for the first two sources and the MINIBALL efficiency can be determined from the number of detected gammas and the run time, fig. 5.7. These two sources (^{152}Eu and ^{60}Co) only provide gamma energies up to 1400 keV, and the efficiency is needed up to 6 MeV. ^{11}Be is used to determine the high energy efficiency, producing gammas up to 6.8 MeV, table 5.1. The activity of ^{11}Be is unknown, hence only the relative intensity between individual gamma lines in ^{11}Be can be determined. The relative intensities are then scaled to overlap with the efficiency from the other sources. ^{207}Bi provides gamma energies between the ones from ^{11}Be and the ones from the low energy sources. The activity of ^{207}Bi is also unknown, and is scaled to overlay with the low energy gamma

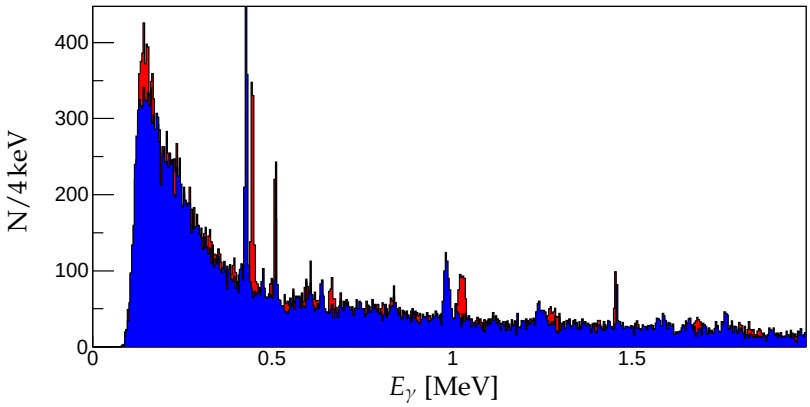

Figure 5.6: Two gamma energy spectra made from the d(^{22}Ne,p)^{23}Ne reaction. A peak close to 1016 keV, but slightly shifted, is seen in both spectra. The spectra are made from a detector placed before (red) and after (blue) the target.

efficicencies. A fit to the following function taken from RadWare [Rad95] is made:

$$\varepsilon_{\mathrm{MB}} = \exp\left(\left[(A + Bx + Cx^2)^{-G} + (D + Ey + Fy^2)^{-G}\right]^{-1/G}\right) \tag{5.15}$$

with:

$$\begin{aligned} x &= \log(E/100\mathrm{keV}) \\ y &= \log(E/1000\mathrm{keV}). \end{aligned}$$

The parameters will not be given here, but the determined efficiencies for the four sources along with the fit is shown in fig. 5.7. The MINIBALL efficiency for each of the detected gammas in the transfer experiment is determined. The efficiencies are shown in table 5.2.

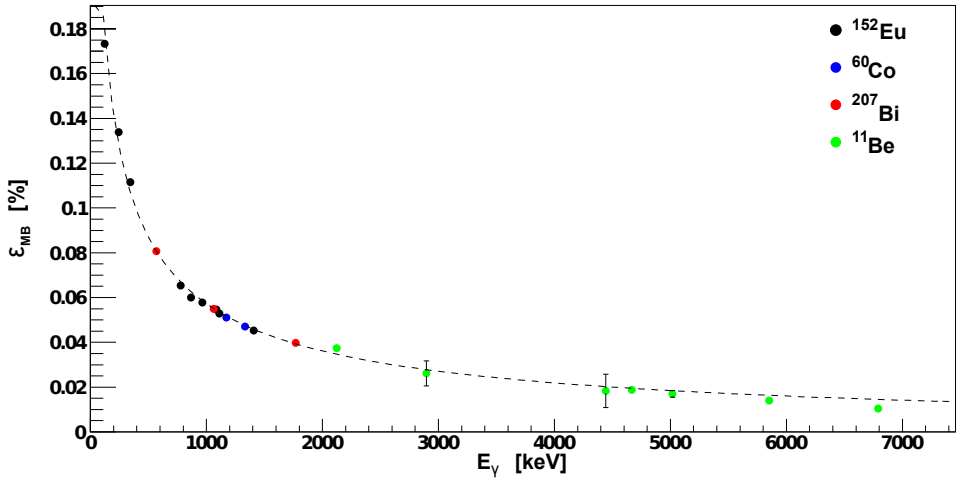

Figure 5.7: The detection efficiency of the MINIBALL as a function of the gamma energy. The measured efficiencies are marked for the individual sources. The dotted line represents the best fit.

Nuclei	γ [keV]	ε_{MB} [%]
^{12}Be	511	8.2
	2100	3.5
	2700	3.0
^{11}Be	320	12
^{10}Be	219.2	14
	2600	3.2
	2900	2.8
	3300	2.5
	6100	1.5

Table 5.2: The MINIBALL efficiency for each of the gamma lines in ^{10,11,12}Be.

CHAPTER 6

Beam diagnostic

In this chapter it will be demonstrated how coincidence events from direct reactions can be used to determine the structure of a radioactive beam. The technique will be used on the ^{11}Be beam in order to improve the transfer reaction analysis.

6.1 Coincidence events

The momentum vector of the detected particles can now be determined, with the detectors calibrated. Next step is to fully understand the momentum vectors of the beam particles. This can be done by using coincidence events. The setup is designed to detect the light particles (p, d and t) and let the heavy fragments slip through to a beam dump, but in some cases it is possible for the heavy nucleus to be detected in the annular detectors, who covers angles down to 8 degrees. Fig. 6.1 shows the relation between the angles of the two outgoing particles for the three main reactions. Only the reactions populating the ground state of the final nucleus is shown, as they provides the largest outgoing angles. The angles covered by the T-REX is marked as grey areas in the plot. The plot shows that coincidence of both ^{11}Be+d and ^{10}Be+t is very likely. Only the d(^{11}Be,t)^{10}Be events are used in this chapter to simplify the analysis as much as possible, especially when determining the beam energy, section 6.2.4. The statistic is still plentiful.

The angular range of the light particles is limited in coincidence events compared to single particle events due to the requirement of a minimum eight degree angle for the nucleus. The statistic of these coincidence events is also much lower than in single particle events (one third for the (d,t) reactions), which makes them less suitable for determining angular distributions and differential cross sections. Instead the coincidence events can be used to determine the shape and structure of the beam. There is a complete knowledge about the total energy and momentum of the final state in a coincidence event. The complete kinematic enables a study of the energy and momentum vector of any of the in- or outgoing particles. In this chapter the incoming particle (^{11}Be) will be studied. The information about the beam gained from coincidence events can then be used to improve the analysis of the single particle events and the simulation of the reaction.

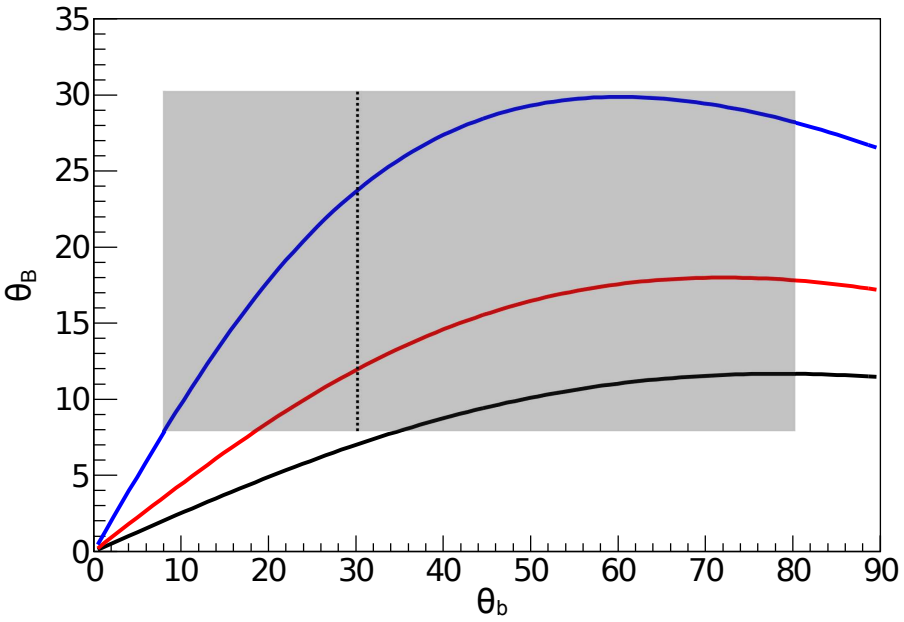

Figure 6.1: The outgoing angle of the heavy fragment (θ_B) as a function of the outgoing angle of the light particle (θ_b). The three lines in the plot represents: Blue: (d,t), Red: (d,d) and Black: (d,p). The grey area represent the area covered by the T-REX, the dotted line indicate the distinction between the AD's and the PSD's.

6.2 Beam characterisation

The characterisation of the beam is done in three steps. First the width and offset of the beam are determined from the azimuthal angle of the two outgoing particles. Secondly the incoming angle and divergence of the beam are determined. Finally the beam energy is determined in two ways.

The order of these steps is determined by the inter-dependency of the quantities. The displacement can be determined independently of the incoming angle and the beam energy, while the two others are very dependent on the displacement and width of the beam, as it will be shown in section 6.2.2 and 6.2.4.

The analysis is derived for a general reaction of the type seen in eqn. 3.1 and tested on simulations before applied to the experimental data in section 6.3.

The outgoing angles of the particles are calculated using eqn. 5.1-5.5 and assuming the reaction occurred in origin. If this is not true, the angles derived are wrong. The beam is characterised by looking at the errors caused by this assumption.

6.2.1 Beam width and offset

The beam width and offset can be determined by calculating the error in the x and y coordinates of the two particles. The principle is to use the azimuthal angles (ϕ) of the two outgoing particles. The azimuthal angles are given by:

$$\phi = \tan \frac{y}{x}. \tag{6.1}$$

It is clear that ϕ is independent on energy, z and the incoming angle, making it ideal to determine the offset of each event. The two outgoing particles will move back to back in the center of mass frame (CM) due to momentum conservation. This leads to the following relation for the azimuthal angles in CM:

$$|\phi_b - \phi_B| = \pi. \tag{6.2}$$

This relation is unaffected by the transformation from CM to the laboratory frame, as the transformation is done along the beam axis, changing only θ's. The transformation is slightly dependent on the incoming angle. The effect is negligible though, as it will be shown from the simulations. Combining the two equations we get the following relation:

$$\frac{y_b}{x_b} = \frac{y_B}{x_B}. \tag{6.3}$$

If this relations does not hold for an event, the x- and y-values are wrong, implying that the reaction did not occur in origin but at a point we will note as (x_A, y_A) to indicate it is the x- and y-value of the incoming particle. The equation is made into a function of x_A and y_A to determine the offset:

$$\frac{y_b - y_A}{x_b - x_A} = \frac{y_B - y_A}{x_B - x_A}. \tag{6.4}$$

This gives a linear relation between the offset in the $x-$ and $y-$direction. The offset is assumed to be as minimal as possible, leading to the following minimization problem:

$$\min(x_A^2 + y_A^2), \tag{6.5}$$

which can be solved using a Lagrangian multiplier:

$$x_A = \frac{x_b y_B - x_B y_b}{(y_b - y_B)^2 + (x_b - x_B)^2}(y_b - y_B) \tag{6.6}$$

$$y_A = \frac{x_b y_B - x_B y_b}{(y_b - y_B)^2 + (x_b - x_B)^2}(x_B - x_b). \tag{6.7}$$

The offset for each coincidence event can now be determined using these two equations. The form of the beam can be illustrated by plotting x_A vs. y_A (xy-plots). Fig. 6.2 shows xy-plots for four simulations with parameters shown in table 6.1. The

Sim.	w_A (mm)	$s_A(x,y)$ (mm)	(θ_A,ϕ_A) (mrad)	Δ_A (mrad)	E^* (MeV)
A	0	(0,0)	(0,0)	0	0
B	5	(0,0)	(0,0)	0	0/3.31
C	5	(-1,0)	(0,0)	0	0
D	5	(0.0)	(87,0)	0	0

Table 6.1: The beam structure for the four Geant4 simulation used to check the technique. All simulations are made with a uniform distribution on a disc in the xy-plane. w is the diameter, s is the offset, θ is the incoming angle and Δ the divergence of the beam. E^* is the excitation of ^{10}Be.

A-D corresponds to the ones in table 6.1. Fig. 6.2A shows the analysis of the simulation with a thin beam. The width of the spot in fig. 6.2A arises from the uncertainty in the x- and y-values of the AD. The same effect is seen in fig. 6.2B, where the spot size of 6 mm diameter is again 1 mm to large. All this indicates an uncertainty of 1 mm in the diameter coming from the uncertainty in the AD strip sizes. The effect of an increased beam width is clear though. Two things should be noted.

First, the distribution in fig. 6.2B is peaked at (0,0) rather than uniformly distributed, indicating that the assumption of a minimal shift is too strong. This makes it difficult to give a description of the distribution of the beam. Simulations with different distributions have to be performed to see the effect of the distribution. A gaussian distribution with a FWHM width of 5 mm is compared to simulation B in fig. 6.3. The projections on the x-axis (x_A) are shown as well. The clear difference in the two plots indicates a possibility for a rough estimate of the distribution. It will be shown in section 6.3, that the experimental data is closest to a uniform distribution, hence the gaussian simulation will not be used more in this chapter.

Secondly, the shape of the peaks are determined partly by the shape of the beam and partly by the setup. The T-REX setup lacks detectors close to $\phi = \pi/4 + N\pi/2$, which causes the missing events at $x = \pm y$ in fig. 6.2. A setup with 4π angular coverage would produce a perfect circle for a circular beam spot, as used in the simulation. The circular shape is easily seen, even without the last part.

The total offset can also be determined, illustrated in fig. 6.2C. Comparing fig. 6.2B and C the two spots are identical except the latter is shifted -1 mm in x corresponding to the shift added to simulation C. This shows that a shift in the beam will be detected with this technique. Once again the beam spot is peaked at (0,0) in fig. 6.2C, confirming the insensitivity to the detailed distribution of the beam spot. The final

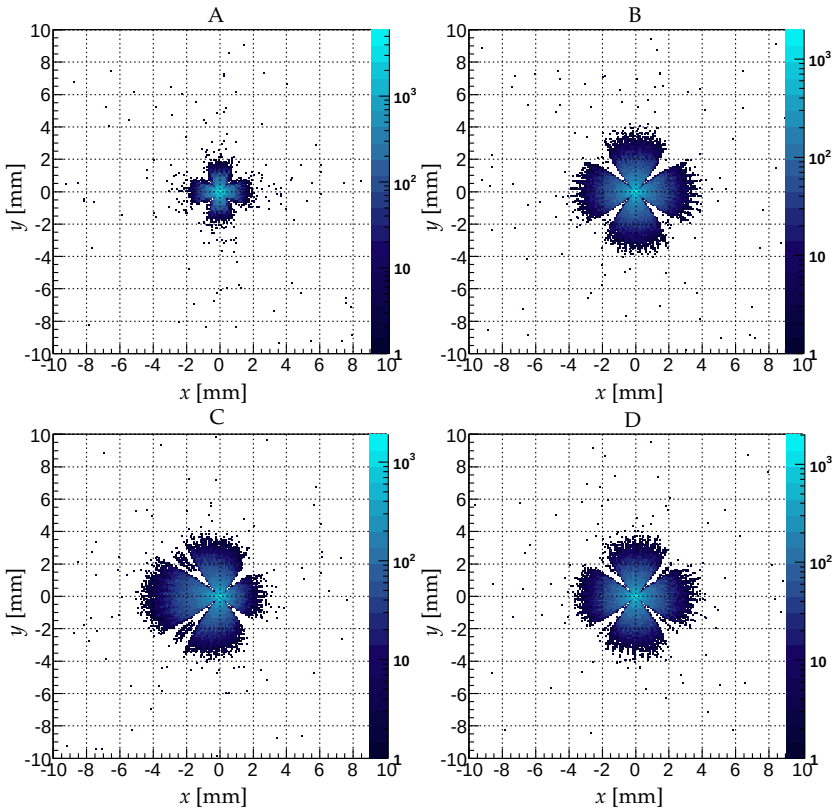

Figure 6.2: A plot of x_A vs. y_A for the four simulations in table 6.1. A-D refers to the simulation numbers. The shape of the peaks are caused by the setup, which does not cover 4π.

simulation, fig. 6.2D, is made to illustrate the independency of the incoming angle. Comparing fig. 6.2B and D no difference is seen despite the large incoming angle in simulation D. This shows no or a negligible effect on the angle of the incoming beam. Furthermore, fig. 6.2B shows the independency on the excitation energy of the final nucleus. Half of the events in simulation B is performed assuming a population of the first excited state in ^{10}Be, and no effect is seen in fig. 6.2B.

In conclusion, the width, shape and offset of the beam can be determined using only the x- and y-coordinates of the two outgoing particles. The uncertainty in the width is $\Delta w = 1\,\text{mm}$ and much lesser for the offset.

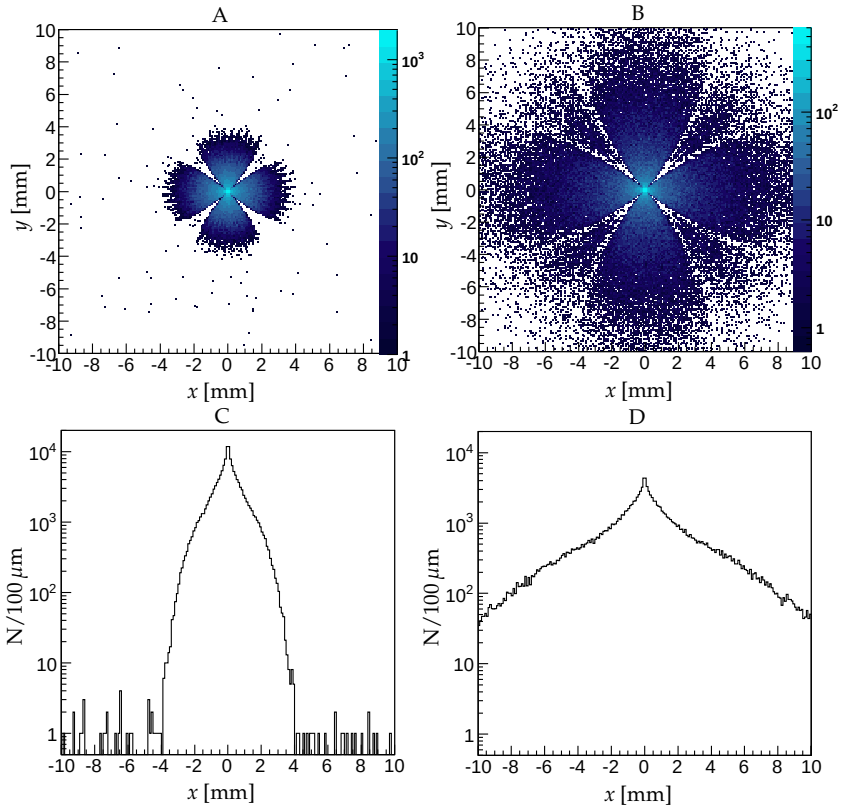

Figure 6.3: xy-plots for a uniform distribution (A+C) and a gaussian (B+D). A+B shows the 2D plot while C+D shows histograms of x_A. The difference in distribution is clearly seen.

6.2.2 Divergence and direction of the beam

The direction of the beam can be determined from momentum conservation. The momentum vector of the beam is given by adding the momentum vectors of the two outgoing particles:

$$\vec{P}_A = \vec{P}_b + \vec{P}_B \tag{6.8}$$

with the momentum vectors of the outgoing particles given by:

$$\vec{P} = \sqrt{\frac{2mE}{x^2 + y^2 + z^2}}(x, y, z). \tag{6.9}$$

The incoming angle and azimuthal angle is then given by:

$$\tan\theta_A = \frac{\sqrt{(P_A^x)^2 + (P_A^y)^2}}{P_A^z} \tag{6.10}$$

$$\tan\phi_A = \frac{P_A^y}{P_A^x}. \tag{6.11}$$

The incoming angle (θ) and the azimuthal angle (ϕ) for each beam particle can be

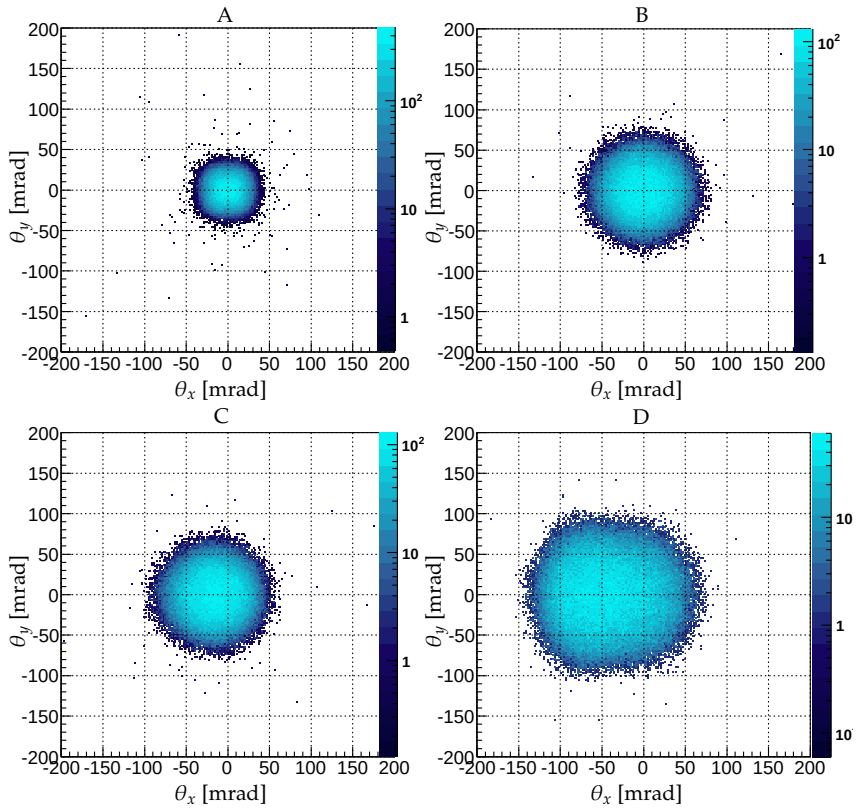

Figure 6.4: A plot of $\theta_A \cos\phi$ vs. $\theta_A \sin\phi$ for the four simulations in table 6.1. A-D refers to the simulation numbers.

determined by combining the four equations. This way the x- and y-component of the angle can be determined by $\theta_x = \theta\cos\phi$ and $\theta_y = \theta\sin\phi$. The dependency on all eight observables can lead to large uncertainties in the results.

The angle have been calculated for the four simulations from table 6.1. Fig. 6.4 shows a θ_x vs. θ_y plot for the four simulations. The large effect of the width of the

beam on the calculated angle is clearly seen. The effects of the energy and z-position can be ignored in the simulations and it will be shown in section 6.3 that the effect is negligible when applying this technique to the experimental data. Fig. 6.4A shows that the uncertainties in x and y lead to a 35 mrad uncertainty in θ_A for each event individually. Combining all events and looking at the total spectrum reduces the uncertainty to a few mrad. The depency on x and y is confirmed by simulation B. The width of the beam leads to a significant spread in the calculated incoming angles ($\Delta\theta_A = 70$ mrad), fig. 6.4B. The comparison of fig. 6.4C and D shows the difference between an offset in the beam and an incoming angle in the beam. The offset is transformed into an offset in the calculated incoming angle, while an angle will lead to a spread in the calculated angle. The large spread in fig. 6.4D indicates that the framework for the incoming angle breaks down at large angles.

To reduce the influence of the beam width and offset on the calculated divergence and direction of the beam the former should be determined before calculating the angles.

6.2.3 Combining the offset and the angle measurements

The strong dependence of the beam width on the incoming angle shown in section 6.2.2 can be investigated further and the resolution on the determined incoming angle can be improved. This will be done in this section.

Fig. 6.5 shows a plot of the x_A-value determined in section 6.2.1 vs. θ_x determined in section 6.2.2 for the four simulations. A similar plot can be made for the y-components, which will not be shown, as the interpretations are similar to the ones for the x-components. Ideally these plots would show the emittance of the beam, but from fig. 6.5A it is clear that experimental resolution effects must be understood first. The beam in fig. 6.5A has 0 mmmrad emittance. The extra width in the plot is caused by the same uncertainties seen in fig. 6.2 and 6.4. Instead the plots can be used to determine the offset, width, angle and divergence independently.

Each plot can be interpreted as having two stretched components, a vertical one at $x_A = 0$ mm and a diagonal one ($\theta_x \approx 25 x_A$). The two components are centered around (0,0) for simulation A and B, as expected. The diagonal in fig. 6.5C is shifted -1 mm in x compared to fig. 6.5B, indicating that an offset in the beam will lead to a shift in the diagonal component corresponding to the offset of the beam, and only a minor shift in the vertical one. An angle in the beam will on the other hand affect the vertical component, as shown in fig. 6.5D, but not the diagonal one. The vertical component in fig. 6.5D is centered at $\theta_x \approx 80$ mrad, compared to the 87 mrad used in the simulation. Furthermore, a width in the beam will stretch the diagonal component while a divergence in the beam will stretch the vertical component, hence

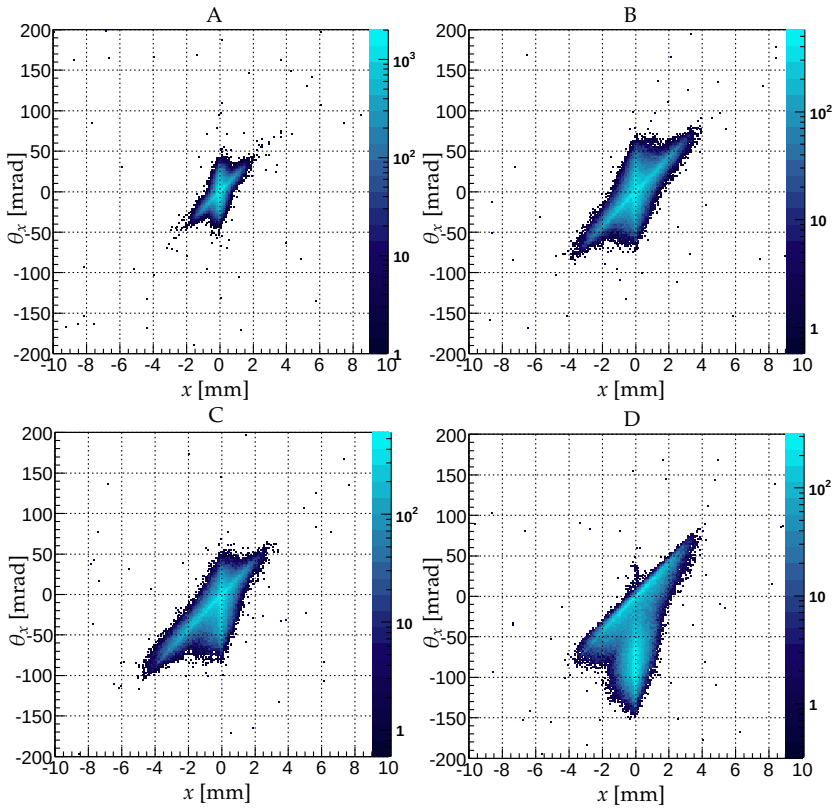

Figure 6.5: A plot of x_A vs. $\theta_A \cos\phi$ for the four simulations in table 6.1. A-D refers to the simulation numbers.

all four parameters (offset, width, angle and divergence) can be determined from a x_A vs. θ_x plot.

The two components are an effect of the setup, and with a setup covering 2π the two components will merge into one. The two components can be separated by gating only on light particles hitting the left or right PSD, or the top and bottom. This is done for simulation C, and can be seen in fig. 6.6. It is clear from fig. 6.5 and 6.6, that the top and bottom PSD's should be used to determine the offset in the x-direction (x_A) and the left and right PSD's should be used to determine the x-component of the incoming angle. The opposite is the case for the y-components. Ideally only particles detected in the xz-plane should be used to determine θ_x and y_A, due to the large sensitivity to these two components and the insensitivity to θ_y and x_A. Likewise, only particles in the yz-plane should be used to determine θ_y and x_A.

Thus an x_A vs. θ_x and a y_A vs. θ_y plot will be used to determine the angle and

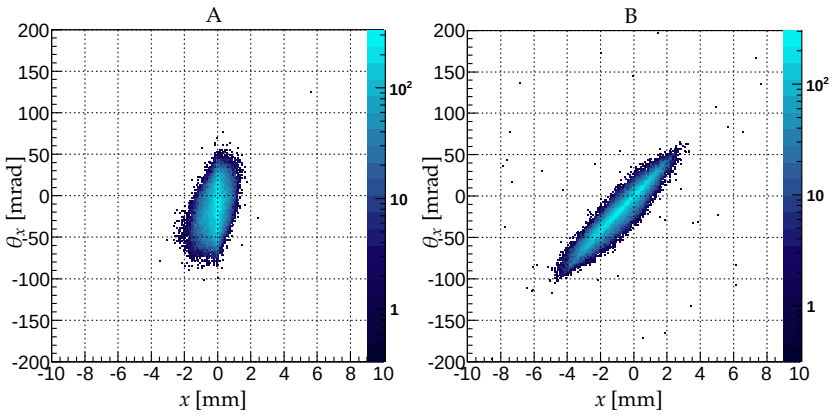

Figure 6.6: A plot of x_A vs. $\theta_A \cos\phi$ for simulation C. (A) is from tritons hitting the left or right PSD. (B) is tritons hitting the top or bottom PSD.

divergence of the experimental beam in section 6.3.

6.2.4 Beam energy

The beam energy is determined in two ways, using first energy and then momentum conservation. In both cases the beam energy is determined at the reaction point, assumed to be in the center of the target. The beam energy before the target can then be calculated by adding the energy lost in the target before the reaction.

Energy conservation gives:

$$T_A = T_b + T_B + E^* - Q. \tag{6.12}$$

E^* is the total excitation energy of the outgoing particles, but normally only B is excited. In this experiment only ^{10}Be can be excited. The excitation energy cannot be directly measured, hence the beam energy minus the excitation energy is calculated instead, and then a correction for the excitation energy is made afterwards:

$$E = T_A - E^* = T_b + T_B - Q. \tag{6.13}$$

The advantage of this method is the independency on the position of the reaction, the only uncertainties arises from the energy of the particles and the energy loss in the target. The disadvantage is the required need of information about the excitation energy.

The second method is calculating the beam energy from:

$$T_A = \frac{(P_A^x)^2 + (P_A^y)^2 + (P_A^z)^2}{2m_A}. \tag{6.14}$$

The momentum vector is calculated using eqn. 6.8. This method gives the beam energy, but it is dependent on the position of the reaction, making the uncertainty dependent on the width of the beam.

Fig. 6.7 shows the calculated beam energy from simulation B in table 6.1. In the simulation half of the events populate the ground state of ^{10}Be and the other half populate the first excited state ($E^* = 3.31$ MeV). The beam energy is set to $T_A = 31.35$ MeV at the reaction point. Fig. 6.7A is the energy calculated using energy conservation. Two peaks are shown at 31.24 and 27.90 MeV with widths 0.150 and 0.157 MeV respectively. The lowest peak is from events populating the excited state in ^{10}Be, and it is lowered with 3.3 MeV corresponding to the excitation energy as expected. Fig. 6.7B shows the energy determined from momentum conservation, only one peak emerges as the method ignores the excitation energy, but the peak is broader than the two in fig. 6.7A due to the uncertainty in the xy-plane. The energy calculated with the second method is 31.45 MeV with a 0.5 MeV width. The beam energy set in the simulation is within the error of all three reconstructed energies proving the validity of the two equations.

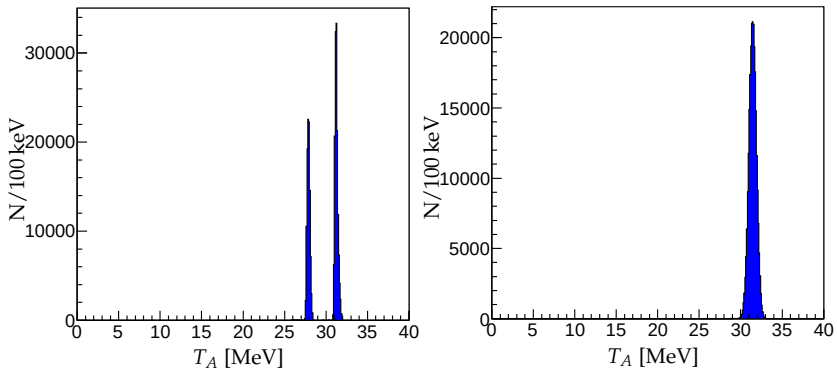

Figure 6.7: Spectra of the incoming energy determined from energy conservation (left) and momentum conservation (right). The spectra are made from simulation B.

Which method to use depend on the reaction, the setup and information known about the final states. The first method requires a clear information about the excitations of the final nuclei and has a stronger energy dependency. The second method is limited due to the beam spot. The methods can also be used together for confirmation as it will be done in section 6.3.

In conclusion the beam energy can be determined within 0.2 MeV with both methods. The spread in the energy determined using momentum conservation is affected by the beam width. A beam width of 5 mm leads to a FWHM energy spread of

$\Delta E = 0.5\,\mathrm{MeV}$.

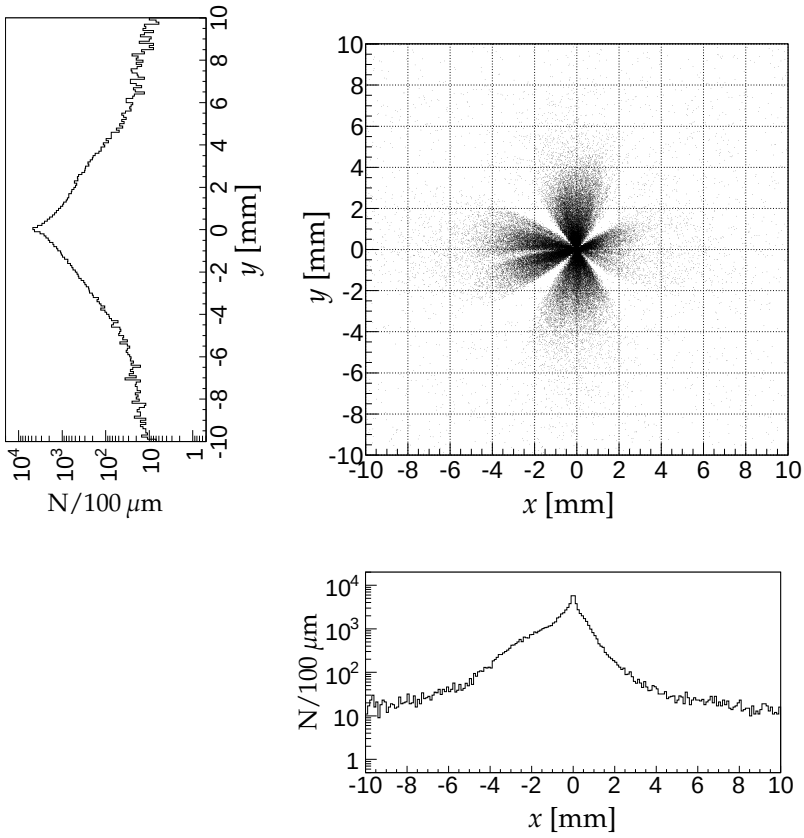

Figure 6.8: A xy-plot of the experimental data from the d(^{11}Be,t)^{10}Be reaction. The plot should be compared to the plots in fig. 6.2 and fig. 6.3

6.3 Experimental data

The method will now be applied to the d(^{11}Be,t)^{10}Be data of the experiment.

The first step is determining the beam width, offset and shape. Fig. 6.8 shows a plot of the calculated x_A's and y_A's, both 2D and projections. Only the outline of the plot is useful, hence no z-color is used. Comparing the projections with fig. 6.3C+D shows indications of a round beam spot with a uniform distribution and a small gaussian tail. The uniform distribution, that makes up the main part of the beam, has a diameter of 6 mm and is shifted -1.3 mm in the x-plane. The tail arises partly from

particles in the beam halo and partly from beam particles scattered on the edge of an 8 mm collimator placed 176 mm before the target.

To determine the incoming angle and the divergence of the beam a plot similar to the ones in fig. 6.5 has to be made, both for the x- and y-component, fig. 6.9A and B.

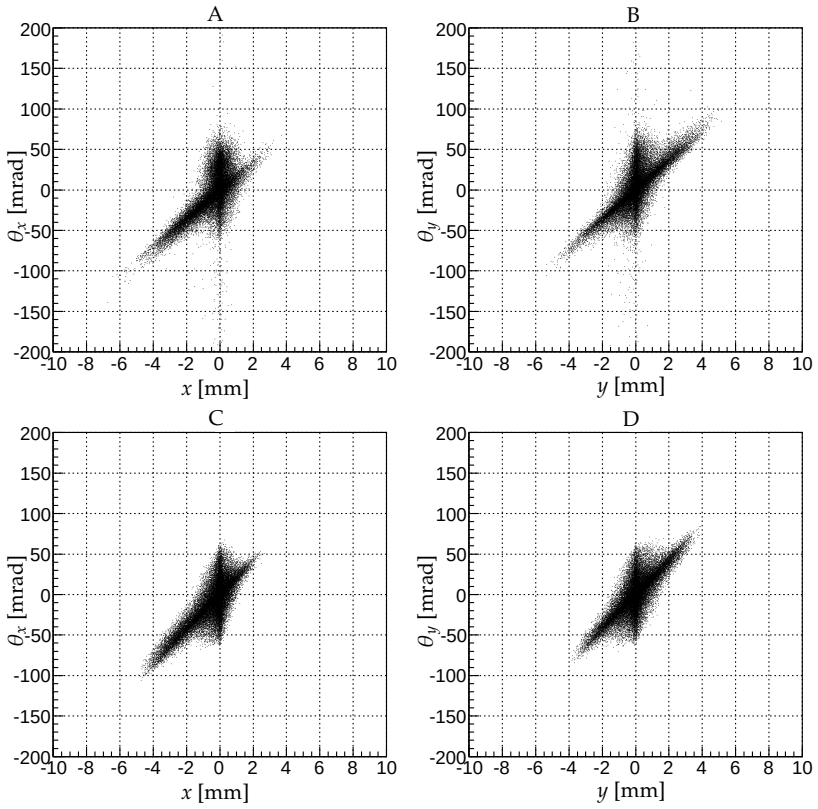

Figure 6.9: A plot of x_A vs. $\theta_A \cos\phi$ (A) and y_A vs. θ_y (B) for the experimental data and for simulation using a beam with $w_A = 6\,\text{mm}$, $s_A = -1.3\,\text{mm}$, $\theta_A = 20\,\text{mrad}$ and $\phi_A = \pi/2\,\text{rad}$ (C) and (D). In order to avoid saturation in the scatter plot, only one third of the data is plotted.

The incoming angle is determined first from the vertical components. θ_x is shifted 20 (5) mrad compared to simulation C, while θ_y is centered around zero. This indicates an incoming angle of $\theta_A = 20\,(5)\,\text{mrad}$ towards the left.

A simulation using the determined value of the beam width ($w_A = 6\,\text{mm}$), offset ($s_A = -1.3\,\text{mm}$) and angle ($\theta_A = 20\,\text{mrad}$) is made to determine the divergence. The x vs. θ_x and y vs. θ_y for the simulated data is plotted in fig. 6.9C and D respectively. The difference between the simulated and the experimental data is caused by either

the tail of the beam width (the diagonal component) or the divergence (the vertical component). The majority of the events in the experimental and the simulated data are placed within the same area, confirming a beam spot of 6 mm shifted −1.3 mm in x and with an incoming angle of 20 mrad. This also indicates a very small divergence of the beam, and an upper limit is set to $\Delta\theta \leq 30$ mrad. Small tails in both width and divergence are present, but they drop off very rapidly.

The determined values for the beam structure have been compared to emittance measurements performed on the REX-ISOLDE using a stable beam [Vou09]. The measurement was performed using an emittance meter and a beam of ^{20}Ne accelerated to 2.85 MeV/u. The result was an rms emittance of $\lesssim 2.8$ mmmrad, this leads to a prediction of just a few mrad of beam divergence at the target with a beam width og 6 mm. This is much lesser than the limit set by the coincidence events, but still consistent.

The beam energy has been determined using both methods described in section 6.2.4, the plots of the beam energies can be seen in fig. 6.10. Method one, using energy conservation, produces three peaks as expected. ^{10}Be has six bound states, but the four highest are separated with only 300 keV, making them indistinguishable in the analysis, see fig. 2.4. Method two, using momentum conservation, only produces one peak. The mean values and widths of the peaks are determined by a gaussian fit. The calculated energies along with the statistical uncertainties given by the fits can be seen in table 6.2 and the energy spreads in table 6.3. A wide distribution at low beam energies is seen in both methods, this is from reactions on the carbon in the polyethylene target. This will be investigated in details in section 6.5.

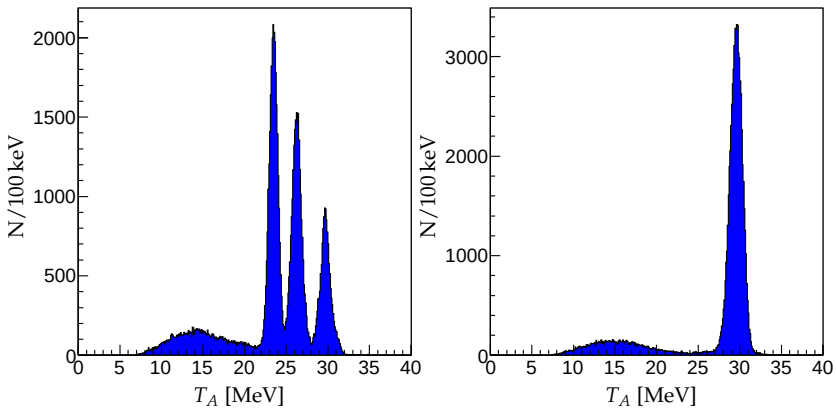

Figure 6.10: The beam energy from the experimental data, determined from energy (left) and momentum (right) conservation.

The width of the beam should lead to a larger width in method two, but the four peaks have comparable widths and all four peaks are much wider than the ones from the simulations (fig. 6.7). The average energy spread from the four peaks is $\frac{\Delta E}{E} = 5\,\%$. This is higher than a previous determined beam spread measured using silicon detectors at REX-ISOLDE [Zoc12]. The beam energy was measured there for a 300 keV/u stable beam. The beam spread was determined to $\frac{\Delta E}{E} = 0.5\%$ and an additional spread of $\frac{\Delta E}{E} = 1.4\,\%$ was seen, caused by the silicon detectors. An increase in energy to 2.85 MeV/u should not increase the total beam spread from 2 % to 5 %. This indicates a new dominating effect.

The large energy spread is expected to stem from a large uncertainty in the reaction depth. The beam energy is calculated assuming the reactions occurring halfway through the target. If the reaction happens in the beginning (or end) of the target, the energy loss corrections are wrong. The effect of the reaction depth has been investigated by calculating the beam energy using the experimental data assuming a reaction at three depths in the target; in the beginning of the target, in the middle and at the end of the target, fig. 6.11. The mean values are determined with gaussian fits and the energy loss in the target before the reaction is added. The calculation showed, that the uncertainty in the reaction depth leads to an uncertainty of $\Delta E_{\text{in}} = 0.8$ MeV in the reconstructed beam energy. Including this effect along with the uncertainty from the silicon detectors may account for most of the observed energy spread.

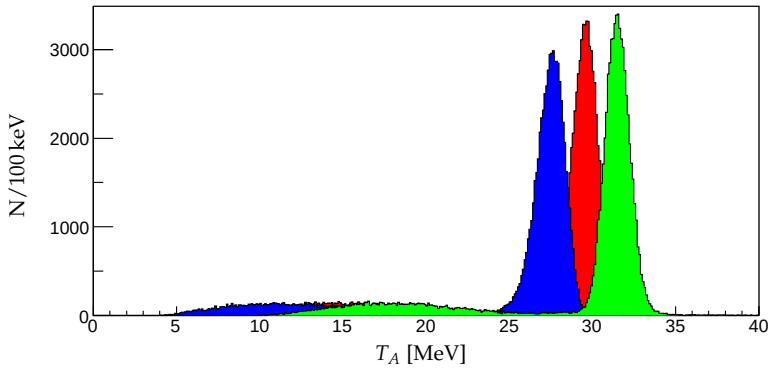

Figure 6.11: The beam energy calculated from momentum conservation using the experimental data, and assuming a reaction in the beginning (green), in the middle (red) and in the end (blue) of the target.

The expected beam energy of 31.35 MeV is within the uncertainty of the measured value, though slightly higher. The expected value of 31.35 MeV is calculated by extrapolating a beam energy measurement at 300 keV/u to 2.85 MeV/u. The mea-

surement at 300 keV/u is a precise measurement performed on a stable beam [Zoc12]. The extrapolation will lead to an uncertainty in the provided beam energy, which is higher than the uncertainty from the coincidence events. Making the values determined from coincidence events more reliable.

The overall structure of the beam is now determined, next step is to look at the fluctuations in the beam throughout the experiment and determining the beam intensity.

Met.	Mean (MeV)	E^* (MeV)	T_{reac} (MeV)	T_{in} (MeV)
1	29.685(6)	0.00	29.685(6)	30.800(6)
	26.257(5)	3.31	29.567(5)	30.690(5)
	23.486(3)	6.1	29.586(3)	30.707(2)
2	29.576(3)	–	29.576(3)	30.698(3)

Table 6.2: Table of the mean values from a gaussian fit to the four peaks shown in fig. 6.10 including the statistical uncertainty. The determined values are calculated into beam energies at the reaction point (T_{reac}) before the beam energy is determined by correcting for the energy loss in the target (T_{in}). Only uncertainties from the gaussian fit is given in the table.

Method	σ (MeV)	ΔE_{FWHM} (MEV)
1	0.656(6)	1.54(1)
	0.625(4)	1.47(1)
	0.546(3)	1.29(1)
2	0.756(3)	1.78(1)

Table 6.3: Table of the sigma of a gaussian fit to the four peaks shown in fig. 6.10. The spread in the beam energies is determined from σ.

6.4 Beam intensity

The beam intensity is needed to calculate the differential cross section, section 3.2. The elastic scattering cross section is mainly nuclear, section 8.2. Hence the elastic

channel cannot be used to determine the beam intensity. Instead six runs with a silver target have been performed throughout the experiment. These reactions are below the coulomb barrier and the elastic scattering can be used to determine the beam intensity. The beam intensities from the six measurements can be seen in table 6.4.

The beam intensity will fluctuate during the experiment. To see this fluctuation a plot of detected particles (p, d and t) pr. minute for each run are plotted as a function of the file number (timescale), fig. 6.12. The plot shows a very intense beam at the beginning of the experiment, but the intensity slowly drops during the experiment. The six measurements of the intensity is also indicated in the plot. The number of detected deuterons pr. incoming ^{11}Be is determined by taking the number of detected deuterons pr. second from a run next to an intensity measurement, and divide by the beam intensity. The values are given in table 6.4. There is a significant fluctuation in the calculated ratios especially in the first (**I**) measurement. The first measurement is taken with a very intense beam, fig. 6.12, and the low beam intensity value is expected to be caused by deadtime due to the high intensity, hence this measurement is ignored. An average value for the last five is made:

$$\frac{N_{\mathrm{d}}}{N_{^{11}\mathrm{Be}}} = 0.76(17) \cdot 10^{-6}. \tag{6.15}$$

The total number of ^{11}Be's on the deuteron target can then be calculated by taking the total number of detected deuterons ($N_{\mathrm{d}}^{\mathrm{total}} = 842400$) and dividing it with the ratio, giving:

$$N_{^{11}\mathrm{Be}}^{\mathrm{total}} = 1.11(25) \cdot 10^{12}. \tag{6.16}$$

Run	I_{beam} [10^6 /s]	$\frac{N_{\mathrm{d}}}{N_{^{11}\mathrm{Be}}}$ [$\cdot 10^{-6}$]
I	3.93	2.3
II	6.12	0.86
III	5.52	1.0
IV	6.06	0.72
V	5.23	0.69
VI	4.46	0.55

Table 6.4: The measured beam intensities from runs with ^{11}Be on Ag, and the calculated ratio between number of incoming ^{11}Be and number of detected deuterons.

The beam intensity clearly changes during the experiment, but does the beam structure? The technique to determine the beam structure described in this chapter is

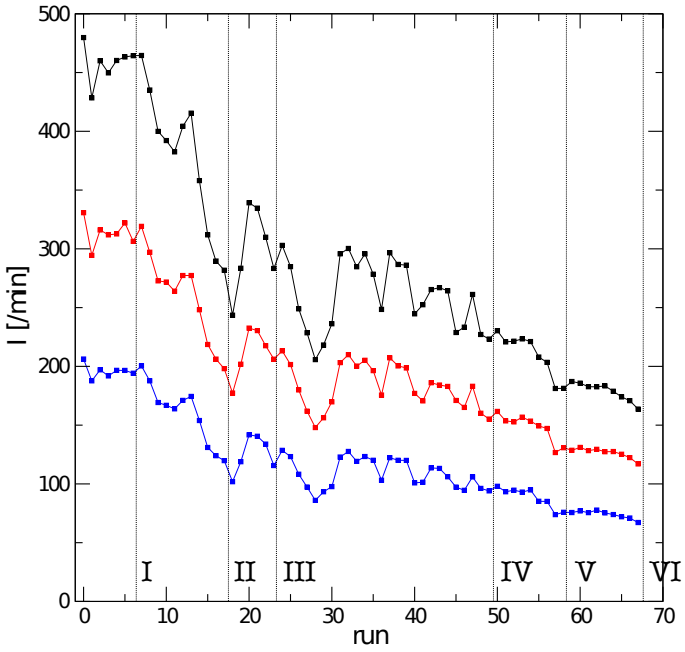

Figure 6.12: The number of detected protons (black), deuterons (red) and tritons (blue) pr. minute for each run on the deuteron target. The time of the beam intensity measurements are marked with vertical lines.

applied to small parts of the data to investigate this. The x vs. y plots at three different times during the experiment; in the begining (run 1-5), the middle (run 21-26) and at the end (run 59-65), are showed in fig. 6.13. No changes are seen and it seems only the beam intensity changes during the experiment.

6.5 Background from contaminants in the target

With the detectors calibrated and under control, and the structure and energy of the beam determined, the only part left to understand, before calculating the differential cross sections, is the target.

The primary target is deuterated polyethylene, which contains, beside deuterons, carbon and protons. ^{11}Be can react with the protons and the carbon nuclei and produce protons, deuterons and tritons, which will form as a background in the analysis.

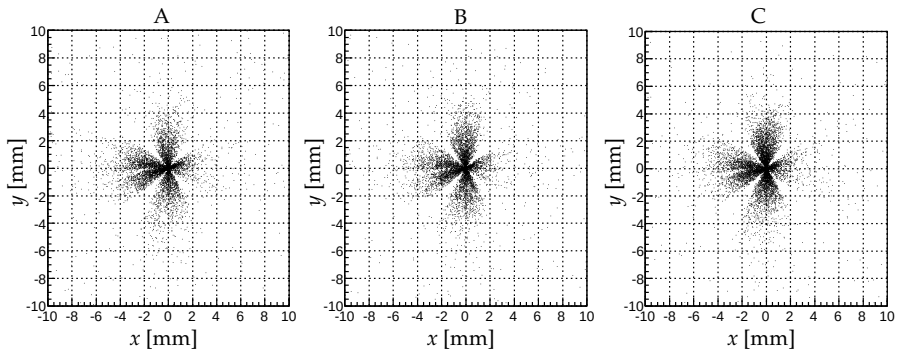

Figure 6.13: Plots of the beam width at different times during the experiment. A: The begining of the experiment with the intense beam. B: In the middle of the experiment at the time of large fluctuations in the intensity, C: In the end with a stable but low intensity beam.

An example of the background has already been seen in fig. 6.10, but it will be even more eminent when calculating excitation energy spectra, chapter 7. It is crucial to understand the background, in order to get the right normalisation and angular distribution. The coincidence events have proven extremely effective in the understanding of the background from contaminations in the target. While the background and the real events are strongly entangled in the single particle events (fig. 7.3), in coincidence events the two are clearly separated. Fig. 6.10 shows a clear separation between the peaks from (d,t) events and the broad, low energy, distribution from reactions on carbon in the target.

Runs have been performed in this experiment using a target of pure carbon and a regular polyethylene target in order to determine the background, section 4.4. The data from these runs are analysed separately, assuming the events are from ^{11}Be+d reactions. This will generate distributions similar to the background in the reactions on deuterated polyethylene. The distributions have to be scaled, to take into account the difference in run time and number of nuclei in the different targets. Normally the background distributions are scaled to fit the single particle events, but the entanglement can lead to a large uncertainty. The coincidence events are used in this experiment instead. The beam energy is calculated for all coincidence events with identified deuterons and tritons assuming d(^{11}Be,d)^{11}Be and d(^{11}Be,t)^{10}Be reactions. The calculations are done for all three targets (CD_2, C and CH_2). The deuterons are used to determine the background from protons in the target. The number of tritons produced in the runs on the proton target ((p,t) reactions) are too few to give a reliable result. The statistic from the (p,d)-reactions are much higher. Fig. 6.14 shows

the calculated beam energies for the three targets. Both energy (left) and momentum (right) conservation are used for (d,t) (top) and (d,d) (bottom).

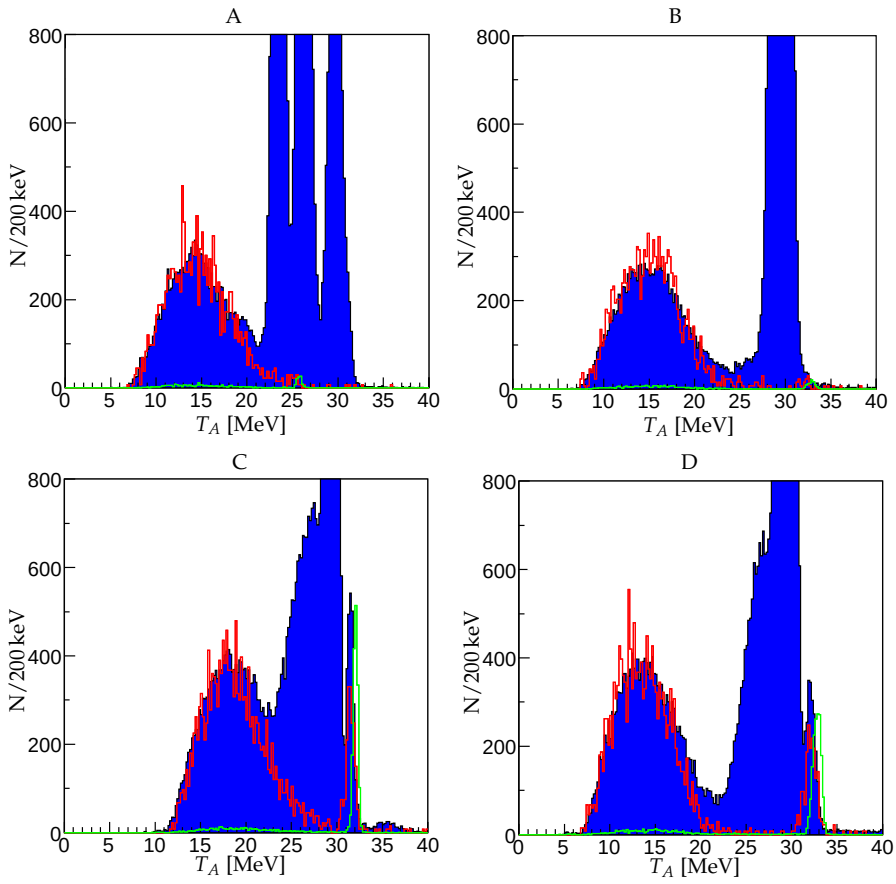

Figure 6.14: T_A calculated from energy (A+C) and momentum (B+D) conservation using coincidence events with identified tritons (A+B) and deuterons (C+D). The three spectra are made with data from three different targets; blue: CD_2, red: C and green CH_2.

The broad distribution is clearly from reactions on carbon nuclei in the target, and is used to determine the scaling factor for the carbon target data:

$$\text{run}_\text{d} = 7.5\text{run}_\text{C} \tag{6.17}$$

A rough estimate of the ratio between carbon nuclei and deuterons in the target can be given, by taking the scaling factor times the ratio between the total lengths of the

runs. A scaling of 7.5 % corresponds to a ratio of:

$$\frac{N_{^{12}C}}{N_d} = 0.53 \text{ (close to 1:2 as expected).} \tag{6.18}$$

Determining the scaling factor for the proton target data is more complicated. Only the deuteron data can be used. A peak at 31 MeV is seen in the deuterated polyethylene data, which is caused by reactions from either carbon or protons in the target. The carbon data contributes to the peak but cannot reproduce the total peak with the scaling factor determined from the broad distribution. The rest is either the tail of the main peak at 29.56 MeV or reactions on protons. The peak from the proton data (scaled with 0.4 in the figure) produces an energy slightly to high, but this might be caused by an unknown effect. Only an upper limit for the scaling factor on the data from runs on regular polyethylene can be set:

$$\text{run}_d = 0.2\text{run}_p \tag{6.19}$$

This corresponds to approximately a 1 % proton contamination in the deuterated polyethylene.

The strong separation between the real and background data shows, that full kinematic events can be used to effectively select true reactions from backgrounds reactions from contaminants in the target, or to determine the ratio between true and background reactions.

6.6 Summary

A new technique to characterise the beam structure using coincidence events has been developed. The technique has been tested on simulated data and successfully reproduced the beam structures. The technique has been applied to the experimental data and the beam structure of the ^{11}Be is determined. The structure is consistent with independent emittance measurements. The technique enabled a study of the beam structure at different times during the experiment. No fluctuations were seen in the beam width but a significant decrease in the beam intensity were detected using the number of detected particles pr. second. A decrease in the beam intensity in an experiment over a few days involving a radioactive ion beam is expected. The beam intensity measurements have also been compared to other measurements (using faraday cups) and again the measurements are in good agreement.

The technique provided the first ever measurements of a fully accelerated radioactive beam at ISOLDE. The analysis gave a description of the beam at the point of the reaction. This information has never been obtained with this precision before at a transfer experiment at ISOLDE, and will prove important in the further analysis.

The clean determination of the contaminations in the target will also prove a valuable information in the next chapter. The strong separation between fusion products and direct reactions is another strength of the coincidence events and can be used to significantly improve the understanding of the background in the analysis. The background will be investigated further in the next chapter.

CHAPTER 7

Excitation energy spectra

The reaction type for each event will be determined in this chapter. This includes determining the type of the outgoing particle and the excitation of the outgoing Nucleus. The chapter contains a high particle energy part and a low particle energy part. The difference between the parts is the ability to distinguish protons from deuterons and tritons for the high energy particles.

7.1 Identifying the reaction type for an event

The initial state of the reactions have been established in the previous chapter. Next step is to understand the final state of the reactions. The important part is to determine the types of the outgoing particles and the state populated in the nucleus for each event. Ideally a differential cross section has to be determined for all bound states in ^{10,11,12}Be individually. This requires a catagorising of each event. The catagorising is done in two or three steps dependent on the energy of the particles. The excitation energy of the nucleus can be calculated using the momentum vector of the initial particles and the outgoing particle (p,d or t). Knowledge about the particle type is required to determine the momentum vector, and the Q-value of the reaction. The particle type can be determined by a $\Delta E - E$ plot if the energy of the outgoing particle is high enough, section 7.2. If the energy is too low to make particle identification the analysis is complicated a bit, section 7.3. Excitation energy spectra are created from the calculated excitation energy, and events populating different states can be separated if the resolution is high enough. This is not the case for most of the bound states investigated in this experiment and gamma gates are used to separate the states with small difference in excitation energy. Gamma gated excitation energy spectra is generated afterwards to confirm the gamma gates.

7.2 High energy particles

High energy particles are defined in this thesis as particles with energy enough to go through the ΔE-detectors, enabling particle identification. The energy required to

pass through the ΔE-detector is dependent on the particle type, the detector thickness and the angle between the detector and the particle. Fig. 7.1 shows the energy required for a particle to punch through the ΔE-detector (enabling $\Delta E - E$ indentification) as function of the laboratory angle for each of the three particle types (solid lines). The kinetic curves of protons, deuterons and tritons for reactions populating the ground states of ^{12,11,10}Be are shown as well (dashed lines). The high energy particles occurs in the very forward angles, hence particle identification will only be attempted in the AD's and the forward PSD's.

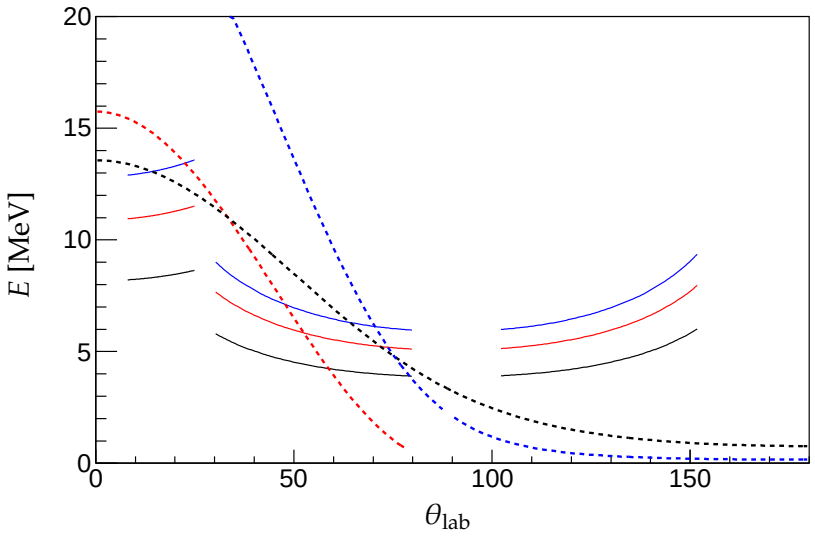

Figure 7.1: The energy required for protons (black), deuterons (red) and tritons (blue) to punch through the ΔE-detector (solid lines). The kinetic curves for the reactions populating the ground states of ^{12,11,10}Be is shown as well.

7.2.1 Particle identification

Particle identification of the high energy particles can be done by comparing the energies deposited in the ΔE and E detectors. There is a strong relation between the energy deposited in the two detectors and the particle type as mentioned in section 5.5. This is evident from a $\Delta E - E$ plot. Fig. 7.2 shows a $\Delta E - E$ plot for strip 5 in the forward PSD's. The plot shows four curves corresponding to protons, deuterons, tritons and α-particles. The shapes of the curves are very dependent on the angle between the detector and the particle, hence a $\Delta E - E$ plot has to be made for each strip in the PSD's to avoid overlap between the three Z=1 curves. To compensate for the dif-

ferent angles within the strip, a small correction is made, assuming a linear relation between the energy loss and the distance travelled in the ΔE-detector [Jep04].

$$\Delta E_{\text{cor}} = \Delta E \cos\theta. \tag{7.1}$$

$$E_{\text{cor}} = E + (1 - \cos\theta)\Delta E. \tag{7.2}$$

Here θ is the angle between the norm of the detector and the incoming particle. This is only valid for small angles, hence the requirement of individual plots for each strip. Corrected values are used in fig. 7.2.

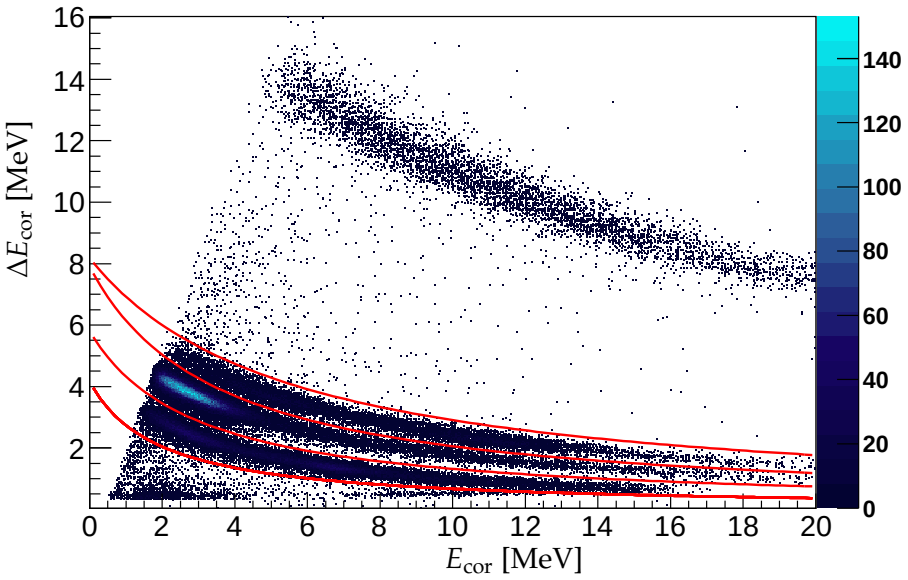

Figure 7.2: A plot of the ΔE vs. E deposited in the strip 5 of the four forward PSD's. The gates made to identify p, d and t are shown as red lines. ^{4}He particles are also seen, but omitted in the analysis.

Gates have been made for each of the three Z=1 particles for each $\Delta E - E$ plot. The gates can be seen in fig. 7.2. All gates are of the form:

$$E_{\text{cor}} = \frac{N}{a\Delta E_{\text{cor}} + b}, \tag{7.3}$$

with N, a and b being parameters determined individually for each strip and particle. If an event lies within two neighboring lines, the event will be classified as being that given particle type, and analysed as such (e.g. particles between the two lowest lines are protons).

7.2.2 Excitation energy spectra

Once the light particle in an event is identified as either a proton, deuteron or triton the excitation of the nucleus can be determined from energy and momentum conservation:

$$E^* = T_A - T_b - \frac{P_B^2}{2m_B} + Q. \quad (7.4)$$

$$\vec{P}_B = \vec{P}_A - \vec{P}_b. \quad (7.5)$$

A, B and b refers to eqn. 3.1. The excitation energy spectra for ^{10,11,12}Be can be seen in fig. 7.3. The ground states are clearly seen in all three spectra. Furthermore, peaks at 2100 keV and 2700 keV in ^{12}Be, and at 3300 keV and 6000 keV in ^{10}Be, corresponding to the excited bound states in the two nuclei, are seen.

The pure excitation energy spectrum of ^{12}Be (top-left in fig. 7.3) contains a significant background. The background arrises from contaminants in the target. The background is also evident in the spectra for ^{11}Be and ^{10}Be, though less significant. Background from reactions on carbon and protons in the target have already been investigated in section 6.5. The events from runs on carbon and regular polyethylene are analysed as if they came from a ^{11}Be+d experiment, and excitation spectra are calculated using eqn. 7.4 and 7.5. The background spectra are scaled with 8.43 (carbon) and 0.2 (proton), and compared to the total spectra, right side of fig. 7.3. The scaling factor of the carbon data is slightly higher than the 7.5 found in section 6.5. The value 8.43 is used to get a better agreement between the background and the total excitation spectra at negative excitation energies, which is definitely background. The cause for the higher scaling factor is still to be determined. Two explanations are in principle possible. Either the scaling factor determined in section 6.5 is too low due to the requirement of coincidence events, or the 7.5 value is correct and another effect contributes to the background. The best candidate so far is ^{22}Ne contamination in the beam. ^{22}Ne+d reactions will produce light particles seen in single particle events, but not any coincidence events and can not be determined from the method described in section 6.5.

Especially reactions on Carbons contribute to the background. This is expected due to the large ratio between deuterons and Carbons ($\approx 2:1$) in the target compared to the ratio between the deuterons and protons ($\approx 100:1$). The uncertainty in the proton background, described in section 6.5, will not affect the angular distributions for the excited states, as gamma gates are used for those (see next section) but the elastic scattering cross section will be affected. The effect is very small, almost negligible, due to the much larger cross section for (d,d) than for (p,d). With a 0.2 scaling of the data from the proton target, the ratio between scattered deuterons and deuterons from (p,d) in fig. 7.3 (middle-right) is less than 0.1

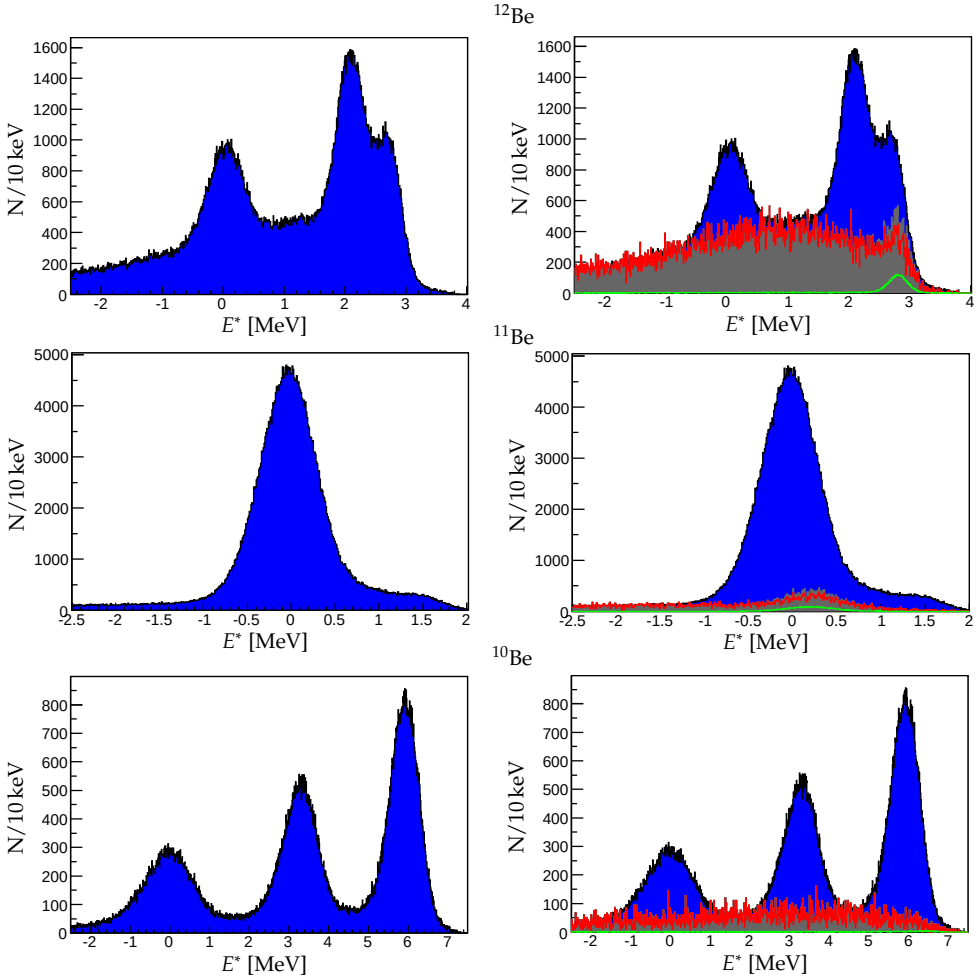

Figure 7.3: Excitation energy spectra made from high energy particles. Left: The pure spectra. Right: Spectra from runs on proton (green) and carbon (red) targets, and the sum of the two (grey) are plotted as well

The energy resolution from the light particles is 500 keV, which is too low to distinguish the excited states in ^{12}Be and ^{10}Be and to distinguish elastic from inelastic scattering. Gamma gates are used to improve the resolution and separate the close lying states in the next sections.

7.2.3 Gamma gated spectra

The gammas detected by the MINIBALL can be used to cleanly separate the events populating closely lying states. Gamma gated excitation energy spectra are generated for gammas in coincidence with deuterons, protons and tritons respectively in the following sections. First step is to generate a gamma energy spectrum for each reaction. All gammas except one produced from the three reactions are emitted from a moving nucleus, which doppler shifts the emitted gammas. The doppler shift can be corrected for, by isolating the gamma energy in eqn. 5.12:

$$E = \gamma E'(1 - \beta \cos\theta). \tag{7.6}$$

The only decay not doppler shifted is the decay of the long lived 0_2^+-state in ^{12}Be. This will be discussed in detail in section 7.2.3.2. The relevant peaks for each nucleus are identified in the gamma energy spectra and energy gates containing the peaks are determined. The gates can be seen in table 7.1. Gamma gated excitation energy spectra are afterwards determined by only using charged particles in coincidence with gammas within the gates. All the gamma peaks of interest are situated on top of a significant background of random coincidences. A background gate is made for all the states to remove the background from the gamma gated excitation energy spectra. The background gates are also shown in table 7.1. comparing with the total excitation energy spectrum, fig. 7.10.

7.2.3.1 ^{11}Be

^{11}Be is the easiest case of the three nuclei with only two bound states. The elastic and the inelastic channels can be separated by gating on the 320 keV gamma peak, clearly seen in fig. 7.4. The peak is placed on top of a large background, and a background gate is made in order to remove events from random coincidences with background gammas. The two gates can be seen table 7.1.

The gamma gated spectrum, with the background subtracted, is plotted along with the total excitation energy spectrum in fig. 7.5. The gamma gated spectra is scaled to take the MINIBALL efficiency, given in table 5.2, into account. The elastic scattering channel is dominating as expected. Still the 320 keV gamma gate provides sufficient data to calculate a differential cross section for the inelastic scattering data as well, chapter 8.

Nucleus	Decay	E_γ [keV]	E-gate [keV]	Δt-gate [ns]
^{11}Be	$1/2^-_1 \rightarrow 1/2^+_1$	320	[300,340]	–
		Background	[340,380]	–
^{12}Be	$2^+_1 \rightarrow 0^+_1$	2100	[2060,2160]	–
		Background	[2160,2260]	–
	$0^+_2 \rightarrow 0^+_1$	511	[490,520]	> -200
		Background	[475,490] or [520,535]	> -200
	$1^-_1 \rightarrow 0^+_1$	2700	[2650,2800]	–
		Background	[2800,3000]	–
^{10}Be	$2^+_2 \rightarrow 2^+_1$	2600	[2500,2750]	–
		Background	[2800,2650]	–
	$2^-_1 \rightarrow 2^+_1$	2900	[2800,3000]	–
		Background	[3300,3500]	–
	$2^+_1 \rightarrow 0^+_1$	3300	[3300,3500]	–
		Background (LE)	[3500,3600]	–
	$1^-_1 \rightarrow 0^+_1$	5900	[4600,6200]	–
		Background (LE)	[6200,6600]	–

Table 7.1: The gamma energy and time gates used to separate the individual reactions from each other in the three nuclei. (LE) means the gate only has been used for low energy particles

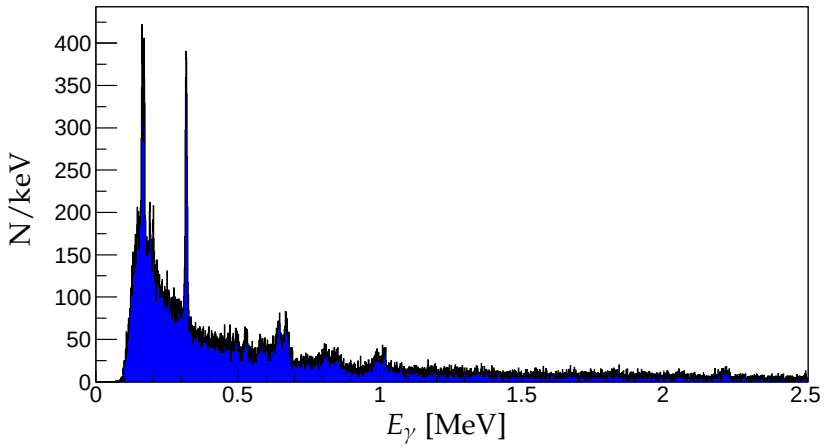

Figure 7.4: The gamma energy spectrum made from gammas in coincidence with a deuteron. The gammas are Doppler corrected. A strong sharp peak is eminent at 320 keV.

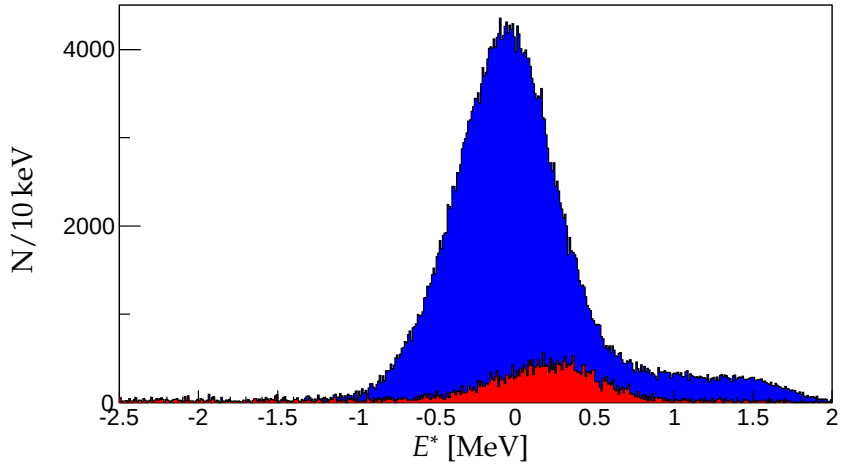

Figure 7.5: The total excitation energy spectra for ^{11}Be (blue) along with the excitation energy spectrum for the excited state in ^{11}Be made from gamma gated deuterons (red).

7.2.3.2 ^{12}Be

^{12}Be has three known bound excited states, which all primarily decays to the ground state, section 2.3. The life times of the 2^+_1 and the 1^-_1 states are very short, and they decay with a 2107 keV and a 2700 keV gamma respectively, table 2.1. The two gamma lines can easily be seen in fig. 7.6. The two peaks lies on top of a small but significant background. A peak and a background gate are made for the two states similar to the $1/2^-$-state in ^{11}Be. The gates are shown in table 7.1.

The 0^+_2 mainly decays (BR = 83 %) to the ground state with an e^+e^- pair creation corresponding to 511 keV signals in the germanium detectors, table 2.1. This leads to a long lifetime for the 0^+_2 state. The lifetime is measured to be 3 31(12) ns [Shi07]. Gammas from states with lifetime in the order of nanoseconds are normally hard to detect with this setup [Wim10b]. The majority of the produced nuclei will have left the reaction chamber before decaying, making the MINIBALL unable to detect them. The gamma decay can be detected if the excited ^{12}Be nucleus is stopped somewhere within the reaction chamber. The maximum angle of the outgoing ^{12}Be in the ground state is shown in fig. 6.1. The angle is slightly smaller for the excited ^{12}Be nuclei, making the maximum angle 10 °, which is still large enough to hit the AD's. If the nucleus is stopped in the AD's, the decay can be detected by the germanium detectors, enabling the generation of a gamma gated excitation energy spectrum for the 0^+_2-state,

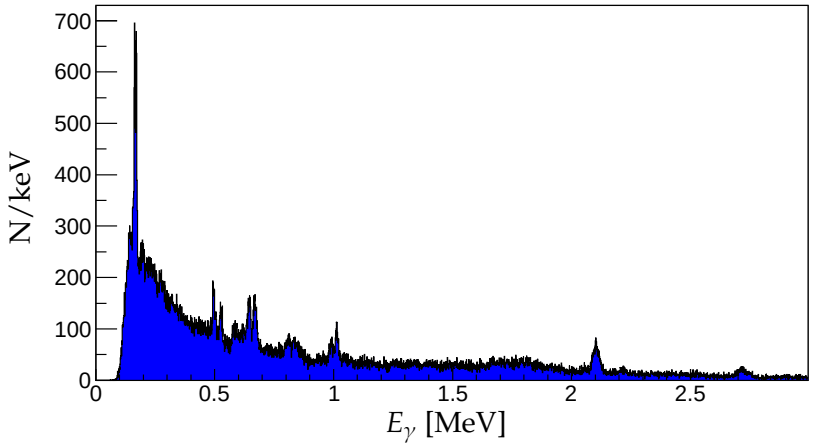

Figure 7.6: The gamma energy spectrum made from gammas in coincidence with a proton. The gammas are Doppler corrected. A sharp peak at 2100 keV is seen, along with a small peak at 2700 keV.

fig. 7.8. The gamma gated spectrum for the 0_2^+-state is scaled to take the MINIBALL efficiency into account. The efficiency of the MINIBALL is determined from decays at the target and not at the AD's, section 5.7, hence a lower efficiency should be expected and the scaling could be too conservative. Furthermore the angular distribution of the detected outgoing particles could be altered due to the requirement on the angle of the ^{12}Be nucleus.

The long lifetime of the 0_2^+ state enables a second gate. Fig. 7.7 shows the time between the detected proton and the detected gamma ($\Delta t = t_\gamma - t_\mathrm{p}$) vs. the gamma energy. The gamma energy, in the plot, is not doppler corrected, as the plot is used to identify decays from a stopped nucleus. The majority of the events are placed close to $\Delta t = -250$ ns corresponding to the difference in the readout times of the germanium and silicon detectors, but events with a larger time difference occur for a few gamma energies. Most of these are random coincidences from gamma background, but three clear lines are visible. The 2100 keV line is mainly random coincidence with gammas from the sequential decay of ^{11}Be to the ground state of ^{11}B via an exited state in ^{11}B. This gamma line is the same as used for calibration of the MINIBALL detectors in section 5.6.1. The 690 keV line is an E0 transition in ^{72}Ge emerging from an excitation of ^{72}Ge in the MINIBALL through an inelastic scattering with neutrons [Jen09]. This line will be investigated in section 10.3.2. The 511 keV is partly from background electrons, but mainly from the E0 transisition in ^{12}Be. The time difference signal can be used to determine the lifetime of the 0_2^+ state, which will be done in section 10.1,

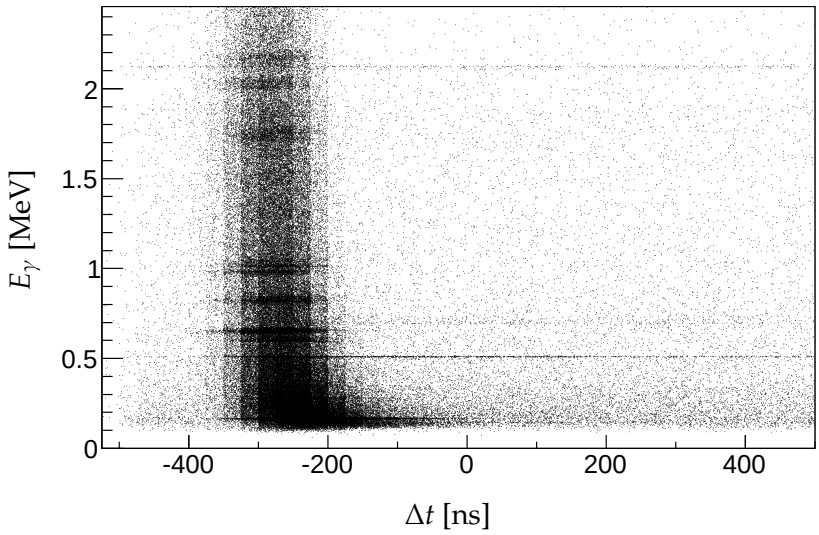

Figure 7.7: The gamma energy vs. the time between the detection of the proton and the detection of the gamma.

but it can also be used to lower the background for the 0_2^+ spectrum by requiring a $\Delta t > -200$ ns, table 7.1.

Note the 2100 keV is present in times before the main peak ($\Delta t < -300$ ns), while the other two only emerges after the reaction. This is a strong evidence for the interpretation of the 2100 keV being random coincidences and the other two stemming from reactions between a target and a beam particle. Projections onto the y-axis in fig. 7.7 at times before and after the main peak has shown the emergence of a low energy tail in the 2100 keV peak after the reaction. The main, present at all times, is centred at 2125 keV consistent with the gamma from the β-decay. The tail could be a peak situated at 2107 keV, corresponding to the gamma decay of the 2_1^+-state in ^{12}Be to the ground state. The tail is interpreted as gammas from the sequential decay of the 0_2^+-state to the 2_1^+-state. A rough estimate of the branching ratios based on the numbers in the tail and the 511 keV line is consistent with the values in table 2.1 determined by S. Shimoura et al. [Shi03].

The gamma gated excitation energy spectra are shown in fig. 7.8 with the backgrounds subtracted. The three peaks are centered at 2100 keV, 2200 keV and 2700 keV, which indicate true events and reliable gamma gates. The three gamma gated spectra are added together with the background spectra in fig. 7.3, and compared to the total excitation energy spectrum. The overlay of the two spectra is almost perfect, but

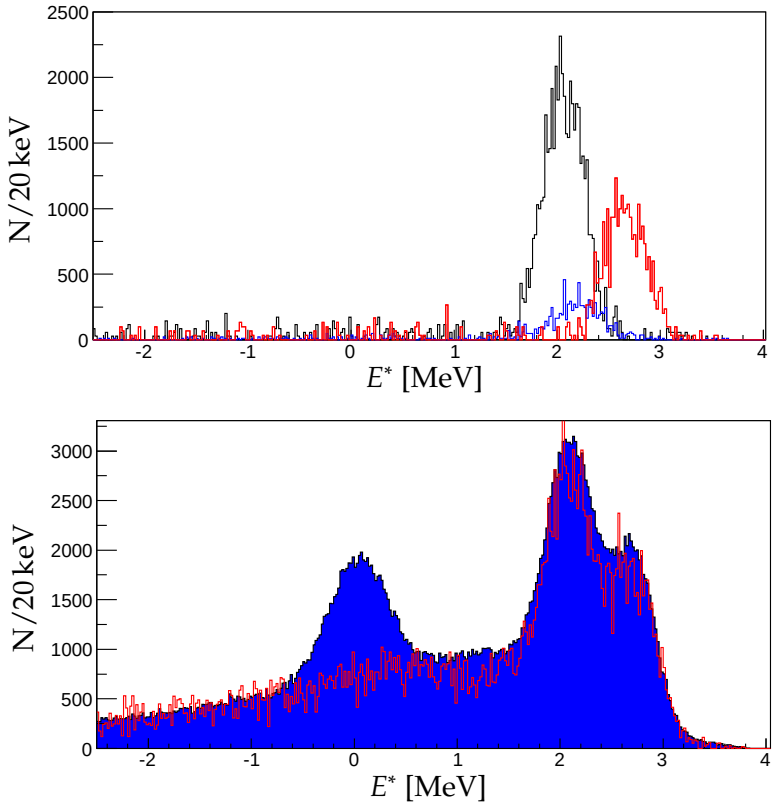

Figure 7.8: Top: Excitation energy spectra from gamma gated protons. Black: 2^+_1 (2107 keV), blue: 0^+_2 (511 keV) and red: 1^-_1 (2700 keV). Bottom: The total excitation energy spectrum (blue) and the excitation energy spectrum made from background runs and gamma gated spectra (red).

some events populating the excited states are still to be accounted for. An attempt to explain these events will be done in section 10.2.

7.2.3.3 ^{10}Be

^{10}Be is the most complicated of the three nuclei due to the four close lying states around $E^* = 6$ MeV, fig. 2.4. It has been possible to identify five out of the six bound states in ^{10}Be. The gamma decays of excited states in ^{10}Be are shown in table 2.1. Four of these gamma lines are clearly seen in fig. 7.9. The figure shows a 2D-plot of the gamma energies versus the excitation energy calculated from the tritons. The projections onto the two axis are shown along with the 2D-plot, the gamma spectrum for

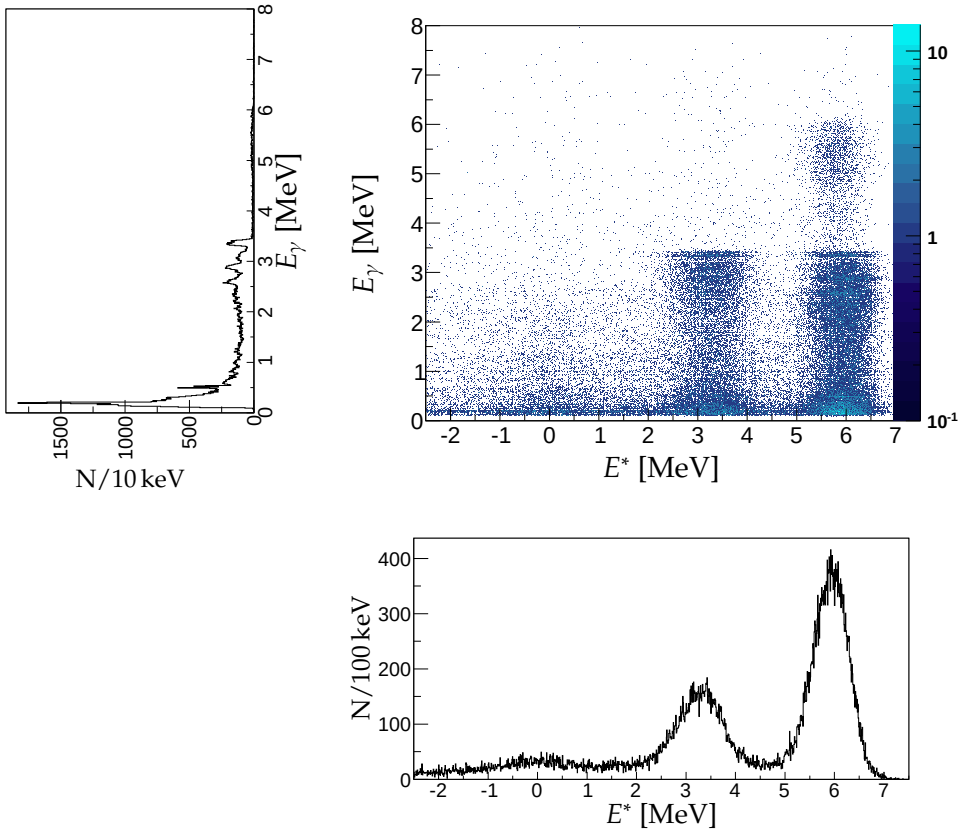

Figure 7.9: A plot of the excitation energy calculated from tritons versus gamma energies. The projection onto the two axis is plotted as well.

the vertical axis and the excitation energy spectra for the horizontal axis. The plot shows the sequential decays in ^{10}Be. Horizontal lines situated around the diagonal ($E_\gamma = E^*$) is the direct decay to the ground state. Both the 3367 keV decay of the first excited state and the 5959 keV decay of the 1^-_1-state are seen. It is evident from the figure, that not all detected gammas around 3367 keV are from the (d,t)-population of the first excited state. A large part of the gammas stem from an indirect population of the 2^+_1-state via a gamma decay from one of the higher lying states. Gating on the 3367 keV gamma line produces two peaks in an excitation energy spectrum, fig. 7.10. The peak at 3300 keV is the 2^+_1-state. The other peak might contain components from all the higher lying states, making it harder to use. Instead the two gamma peaks, rising from the gamma decay to the 2^+_1-state, are used to study the higher lying states.

The two sharp peaks at 2600 keV and 2900 keV can easily be separated and the statistics from the two decays are sufficient to calculate differential cross sections, hence the 3367 keV gammas can be ignored for the high lying states, and is only used to calculate the differential cross section for the 2_1^+-state.

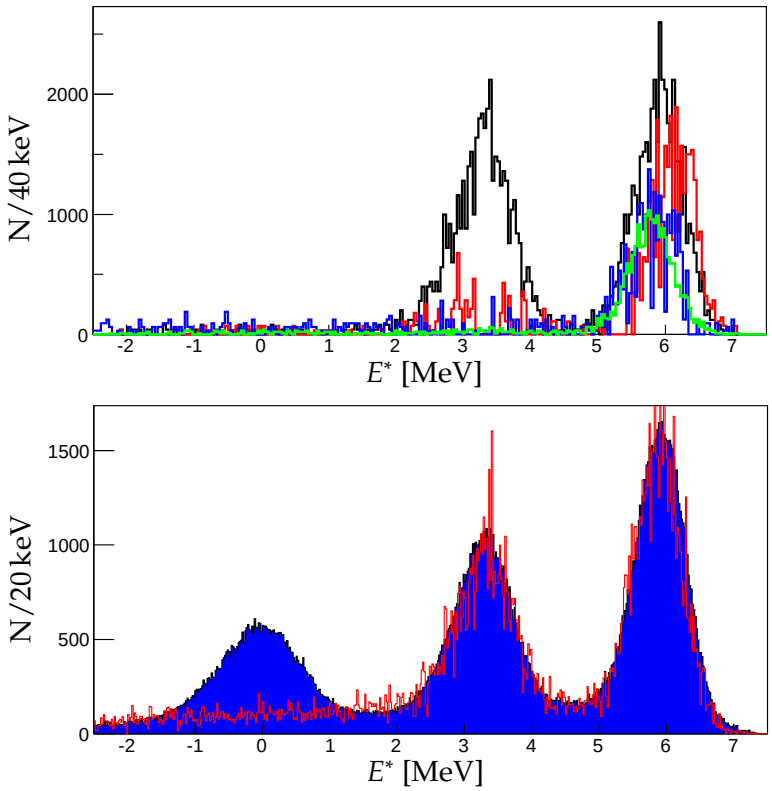

Figure 7.10: Top: The excitation energy spectra for ^{10}Be made using the gamma gates shown in table 7.1. Black: E_γ = 3300 keV, red: 2900 keV, blue: 2600 keV and green: 6000 keV. Bottom: The total excitation energy spectrum (blue) and the excitation energy spectrum made from background runs and gamma gated spectra (red).

The excitation energy spectra, made from gates on the 2600 keV and the 2900 keV gamma peaks, each have one peak, fig. 7.10. The mean value of the peaks are 5839 keV and 6151 keV corresponding to either the 2_2^+ or the 1_1^--state for the former and the 0_2^+ or the 2_1^--state for the latter. The quantity of each state within one of the two peaks have to be determined to calculate differential cross section for each state. The 2_2^+ and the 2_1^--states only have one gamma decay channel (2590 keV and 2895 keV

respectively) and all information regarding these states lies within the two gamma gated spectra. The 0_2^+ and 1_1^--states, on the other hand, have two decay channels, table 2.1. The second decay channel can be used to study the two states. The knowledge gained for the two states from the second decay channels can be used to determine the amount of 1_1^- and 0_2^+ in the two gamma gated spectra at 2600 keV and 2900 keV.

The 1_1^--state decays to the ground state and the 2_1^+-state with a ratio close to 2:1 (table 2.1) producing a 5959 keV and a 2590 keV respectively. The 1_1^--state is the only one of the four highly excited states, that decays to the ground state, and all the 6 MeV gammas seen in fig. 7.9 stem from the 1_1^--state. An excitation energy spectrum is made by gating on the 6 MeV peak, including the Compton edge to gain enough statistics, table 7.1. The excitation energy spectrum is seen in fig. 7.10 as the green line. The spectrum is scaled to take the MINIBALL detection efficiency into account. The MINIBALL detection efficiencies, calculated in section 5.7, are only for the peak energies, and not for the peak+Compton edge. The efficiency will be larger if the Compton edge is used as well, as in the 1_1^--case. The new efficiency for the 1_1^--state is estimated from a simple formula:

$$\varepsilon_{\text{peak+compt}} = \frac{N_{\text{peak+compt}}}{N_{\text{peak}}} \varepsilon_{\text{peak}} = 9.5\%. \tag{7.7}$$

This is the scaling factor used in fig. 7.10. The overlap between the 6 MeV spectrum and the 2600 keV is almost perfect. The mean values are the same, as expected (the two states producing the 2600 keV gamma are only separated by 5 keV), and the integrals, after scaling, are similar ($N_{2600} = 2006$ and $N_{6000} = 1951$). Using the integral of the 6 MeV peak and taking the branching ratios of the 1_1^--decays into account gives an estimate of the quantity of 1_1^- in the 2600 keV peak. The estimate is 45 % of the events stem from the 1_1^--state.

The 0_2^+-state decays to the 2_2^+-state 34 % percent of the time, producing a 219.2 keV gamma, table 2.1. The 1:2 ratio between the 219.2 keV and the 2811 keV is fully compensated by the 14:2.8 ratio in detection efficiency of the MINIBALL (table 5.2) and the 219.2 keV should be the strongest peak for the 0_2^+-state in the gamma spectrum, fig. 7.9. No indications of a gamma peak at that energy are seen in fig. 7.9, and the population of the 0_2^+, in this experiment, is assumed to be negligible. Hence the 2900 keV peak is expected to be fully 2_1^-.

All four gamma gated spectra for ^{10}Be are now well understood, and the strong populations of the 1_1^- and the 2_1^--states compared to the 2_2^+ and the 0_2^--state are in excellent agreement with the requirement of two step process' for the latter two, section 2.4. A perfect overlay is evident, when adding the four gamma gated spectra together, along with the background and

7.3 Low energy particles

A large fraction of the detected particles can not be identified through a $\Delta E - E$ identification, due to too low energy. Fig. 7.1 clearly shows, that at large laboratory angles the energies are too low to make particle identification. Large laboratory angles in inverse kinematics correspond to small CM angles in direct kinematics, which holds great information in the differential cross sections. Thus low energy particles are of a great importance, and the separation of the individual reactions are a significant part of the analysis.

Note that a lower limit of 2 MeV is set due to noise in the setup, and no particles are detected with energy lower than 2 MeV.

The analysis is done in two steps, one for the backward angles and one for the forward angles.

7.3.1 Backward laboratory angles

The only reaction producing particles, with high enough energy to be detected, in the backward angles is the d(^{11}Be,p)^{12}Be reaction. All particles, in the backward PSD's, are therefore analysed as protons from a d(^{11}Be,p)^{12}Be reaction, and the excitation energy spectrum for ^{12}Be is calculated, fig. 7.11. Fig. 7.11A shows the total excitation spectrum along with the spectrum calculated from background runs (grey). The spectrum is clearly dominated by background. By subtracting the background caused by contaminants in the target a much cleaner spectrum can be made, fig. 7.11B. The ground state population is clearly seen, and can be used to calculate the differential cross section in the very forward CM angles. A significant background is still present, which can lead to an overestimate of the differential cross section. No excited states are seen, due to too low particle energies.

7.3.2 Forward laboratory angles

The analysis in the forward direction is more complicated due to the larger amount of reactions and populated states. Background from heavy fragments like scattered ^{11}Be on carbon or ^{10}Be as described in Chapter 6 will complicate the analysis further. Also ^{8}Li and ^{6}He, which have large outgoing angles, are detected.

The analysis can be divided into two steps identifying the reactions populating the excited states through gamma gates, and finally determining the reactions populating the ground states of ^{10,11,12}Be. The last part requires a removal of the background.

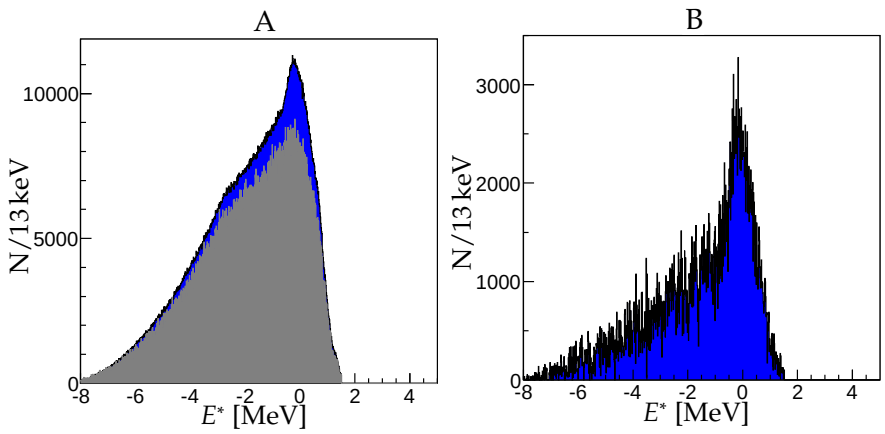

Figure 7.11: The excitation energy spectrum for low energy particles in the backward angles. The ground state of ^{12}Be is clearly seen when the large background is subtracted.

7.3.2.1 Excited states

The gamma gates shown in table 7.1 should also be valid for the low energy particles, but it has to be checked. Fig. 7.12 shows the gamma energies after correction for doppler shift. The spectrum is divided into three energy ranges to clarify the picture. The low statistic at high energy would not be visible if plotted together with the low energy part. The gamma energies versus the time difference between the gammas and the particles are shown in fig. 7.13. Fig. 7.13 clearly shows time delayed 511 keV gammas, but background from other positrons is more significant here, than for the identified proton data. Contrary to fig. 7.7, 511 keV gammas are seen at times before the reaction. The gamma gated spectrum for the $0_2^+ \rightarrow 0_1^+$ reaction shown in fig. 7.14top has a larger background even after subtraction of the background determined from the background gate. The peak at 2200 keV is clearly seen in the spectra, but the background could lead to an uncertainty in the final results.

The 320 keV gamma line from the inelastic scattering is clearly seen in fig. 7.12, but the picture is much more complicated between $E_\gamma = 2$ MeV and $E_\gamma = 3.5$ MeV, where five gamma lines are placed within 1.5 MeV. The 2700 keV gamma line from the $1_1^- \rightarrow 0_1^+$ decay in ^{12}Be is placed between the 2600 keV and the 2900 keV from decays in ^{10}Be. This leads to further uncertainty in the 2600 keV line due to the Compton edge of the 2700 keV line. Yet the resolution of the MINIBALL is high enough to distinguish all five states. The gating on the 2100 keV line from the $2_1^+ \rightarrow 0_1^+$ decay in ^{12}Be is complicated by a large background peak at 2100 keV stemming from the β-decay

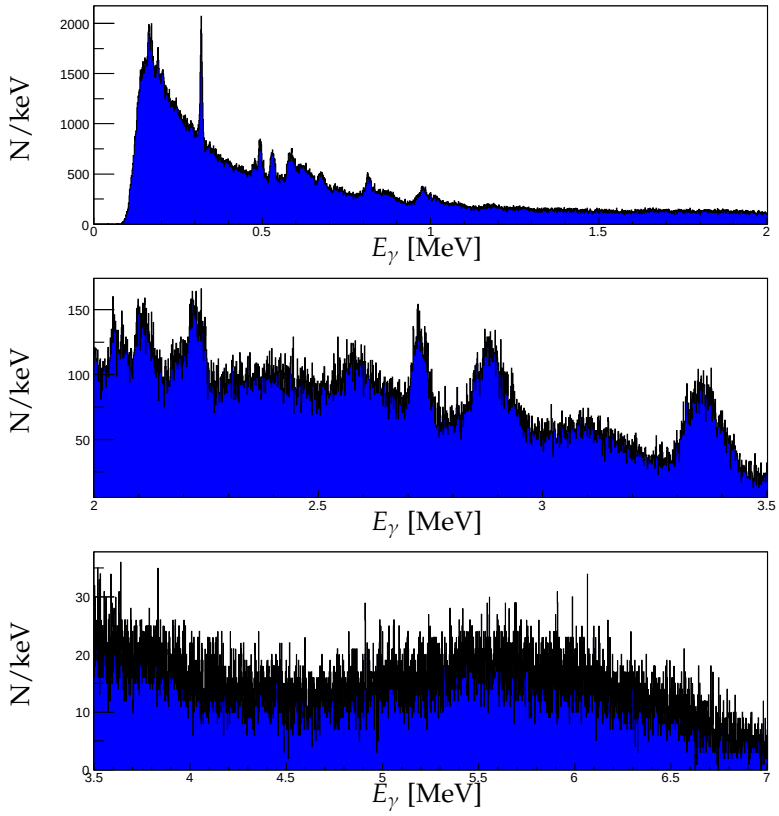

Figure 7.12: Gamma energy spectrum for gammas in coincidence with low energy particles. The spectrum is divided into three, due to the large difference (2000/keV to 20/keV) in number of detected gammas from low energy to high energy.

of ^{11}Be. The line is already discussed in section 7.2.3.2. The gammas from the β-decay of ^{11}Be are not doppler corrected, as they come from stopped ^{11}Be somewhere in the setup, and the peak is clearly seen in fig. 7.13. This peak will be divided into two peaks when correcting for the doppler shift, and can be seen in fig. 7.12 as the two outer peaks of the three at 2100 keV. The one in the middle is the gammas from the decay in ^{12}Be. An extra gate is placed on gammas for the $2^+_1 \rightarrow 0^+_1$ decay to remove background from random coincidences with gamma from the β-decay:

$$E'_\gamma < 2100 \text{ or } 2140 < E'_\gamma. \tag{7.8}$$

Here E'_γ is the raw gamma energy without any correction for doppler shift.

The large gamma background becomes a problem for the 5959 keV gamma line. No sharp peak is identified in the bottom plot in fig. 7.12, only a broad distribution

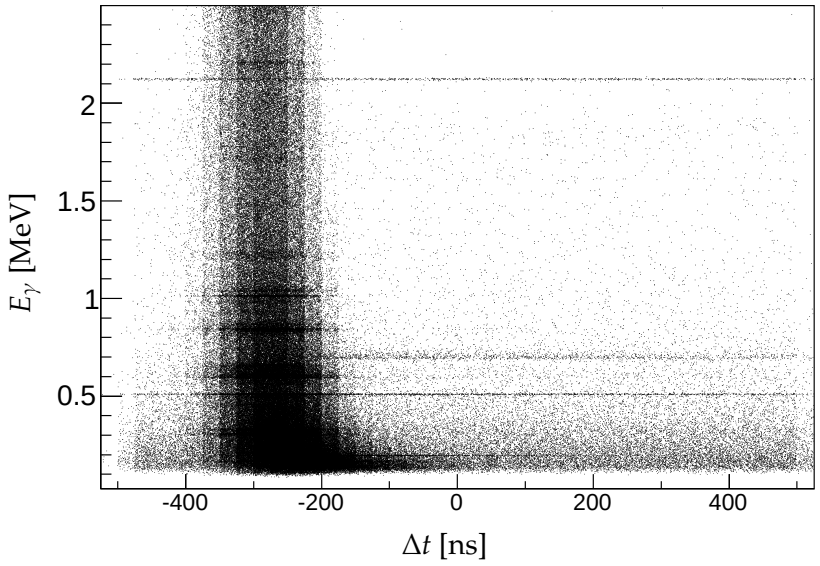

Figure 7.13: The gamma energy vs. the time between the detection of a low energy particle and the detection of the gamma. To avoid saturation in the scatter plot only 0.4 of the events are plotted.

starting at $E_\gamma = 4.6\,\text{MeV}$. A background has to be subtracted when making the excitation spectrum for the 1^-_1-state in ^{10}Be. The background is made at the high energy end (table 7.1) and has to be scaled with a factor given by:

$$\frac{N_{5959}}{N_{\text{bg}}} = \frac{\varepsilon_{4600} + \varepsilon_{6200}}{2\varepsilon_{6200}} \frac{L_{5959}}{L_{\text{bg}}} = 4.5. \tag{7.9}$$

With ε being the MINIBALL efficiency at the given energy, and L is the length in energy interval for the two cuts. Normally the scaling factor is given only by the ratio in the length, but due to the change in efficiency from 4600 keV to 6200 keV an extra factor has to be added.

Excitation energy spectra of ^{10,11,12}Be are shown for the gamma gated events in fig. 7.14. The background is subtracted in all the spectra, and clear peaks with only limited background left are shown. The energy of the peaks correspond perfectly with the excitation energy of the states. The spectrum in the middle, corresponding to inelastic scattering, has a broad distribution ranging from $2 - 3.5\,\text{MeV}$. This background is clearly separated from the inelastic scattered deuterons and can be ignored when calculating differential cross sections. The distribution will be investigated in chapter 10.

Once again the amount of the 1^-_1-state in the 2600 keV gamma gated spectrum has to be determined. This is done similar to the high energy tritons and the result is 41 % of the 2600 keV-gamma peak are from the 1^-_1-state, consistent with the high energy result.

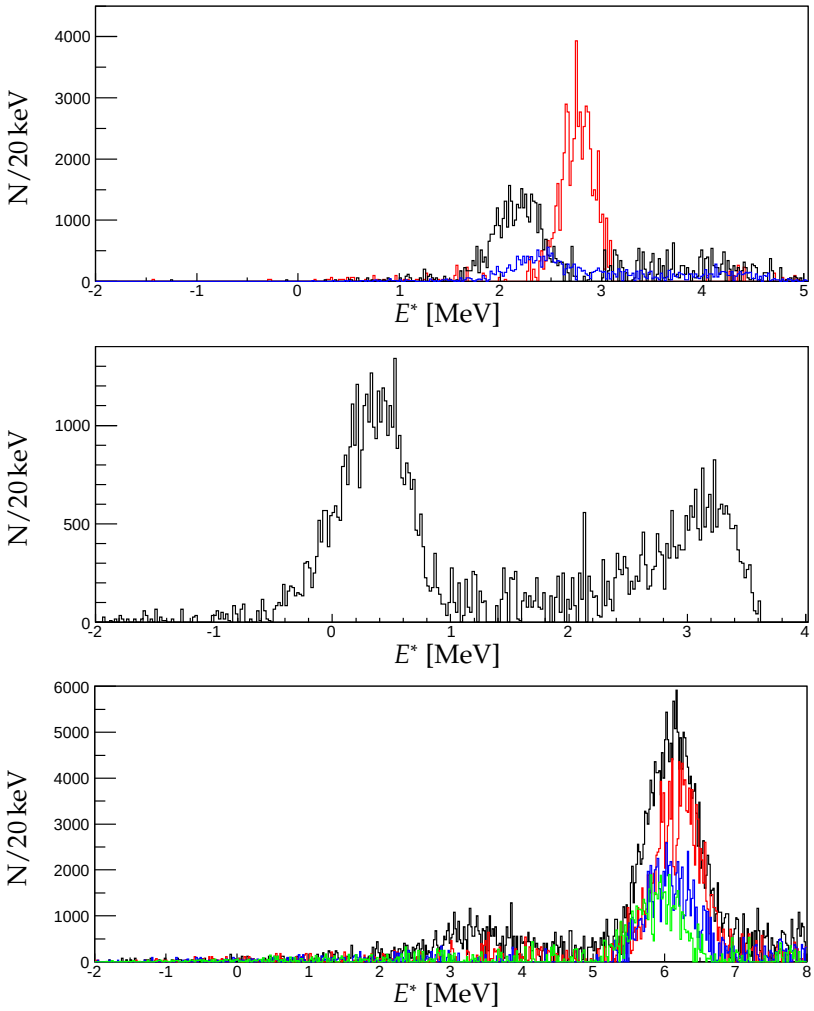

Figure 7.14: The excitation energy spectra from gamma gated low energy particles. The Particles are analysed as protons (top), deuterons (middle) and tritons (bottom). The colors correspond to the same as in the excitation energy spectra from high energy particles.

7.3.2.2 Ground states

Gamma gates cannot be used to identify reactions populating ground states, hence another method has to be used. Like for the high energy particles, the ground states can be found by subtracting background and excited states from the total excitation spectrum. Generally that would mean calculating three excitation energy spectra assuming all particles being protons, deuterons and tritons respectively, but of the three reactions populating the ground states of ^{12,11,10}Be, only the elastic scattering produces low energy particles in the forward direction, fig. 7.1. Hence only one excitation spectrum has to be made, assuming all particles are scattered deuterons. The total excitation spectrum (top) and the total spectrum with excited states and background subtracted (bottom) are shown in fig. 7.15. A peak is clearly seen at 0 MeV and no indication of further background around 0 MeV is present in the bottom spectrum. The extra components at higher energies are a combination of inelastic scattered deuterons into the continuum of ^{11}Be (peak at 1.8 MeV) and other heavy fragments like ^{8}Li and ^{6}He, not investigated in this thesis.

7.4 Summary

In summary, all but one bound states in ^{12}Be, ^{11}Be and ^{10}Be have been successfully determined using gammas detected by the MINIBALL. The identification has been done in a large angular range both with and without particle identification. The high beam intensity has compensated for the low detection efficiency of the MINIBALL above 2 MeV. Even at 6 MeV with a detection efficiency of $\varepsilon = 1.5\,\%$ we were able to get sufficient statistic to identify the 1^-_1-state in ^{10}Be. Comparisons of gamma gated and total excitation energy spectra have shown an almost complete identification of all high energy particles and 75 % of the low energy particles.

The calculation of the differential cross sections and the comparison with theoretical models will be described in the next chapter.

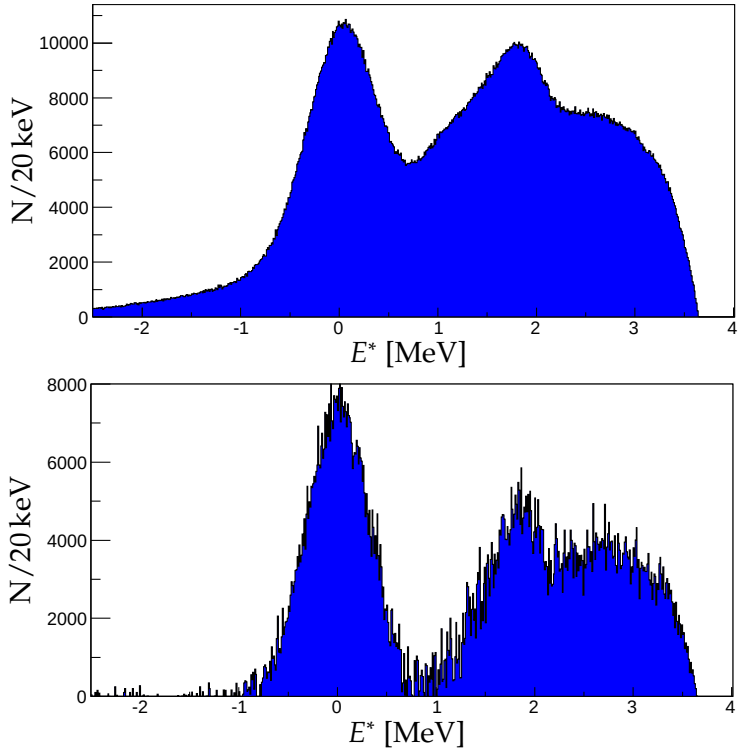

Figure 7.15: Top: An excitation energy spectrum for ^{11}Be assuming all low energy particles are scattered deuterons. Bottom: The same as the top one, but with background and reactions to excited states subtracted using gamma gates.

CHAPTER 8

Differential cross sections and spectroscopic factors

The experimental differential cross sections for all the individual reactions will be determined in this chapter. The experimental cross sections will be compared to preliminary theoretical calculations. Preliminary spectroscopic factors will be determined and the effects of the deformation and the halo structure of ^{11}Be will be investigated.

8.1 Differential cross sections

The aim of the experiment was to determine differential cross sections for the scattering and transfer reactions, and compare them to theoretical calculations. The comparisons are done separately for the three reactions ((d,d), (d,p) and (d,t)), and the theoretic calculations are done with different models. The difference between the models is the potential from ^{11}Be felt by the deuteron. The complicated structure of ^{11}Be described in chapter 2 has a large impact on the differential cross sections. This is well known and have been seen in different experiments [DP10, Sch12]. The focus in this thesis will be on the effect of the deformation of ^{11}Be and the large coupling to the first excited state of ^{11}Be in these reactions.

8.2 Calculating cross sections from the experimental data

The events were separated according to their reaction types in the previous chapter. With the reactions successfully identified the differential cross sections can be calculated using eqn. 3.6. Three of the parameters are already determined, $n_t = 7.5(3) \times 10^{-8}$ mb (section 3.2), $N_A^{\text{exp}} = 1.11(25) \times 10^{12}$ (section 6.4) and $N_A^{\text{sim}} = 1 \times 10^6$, leaving only the angular distribution (a) to be determined.

The angular distributions are determined by splitting the excitation energy spectra, calculated in chapter 7, into small intervals of center of mass angles, fig. 8.1. Each spectrum covers an angular range of 3 $^{\text{o}}$ in center of mass. The same spectra are

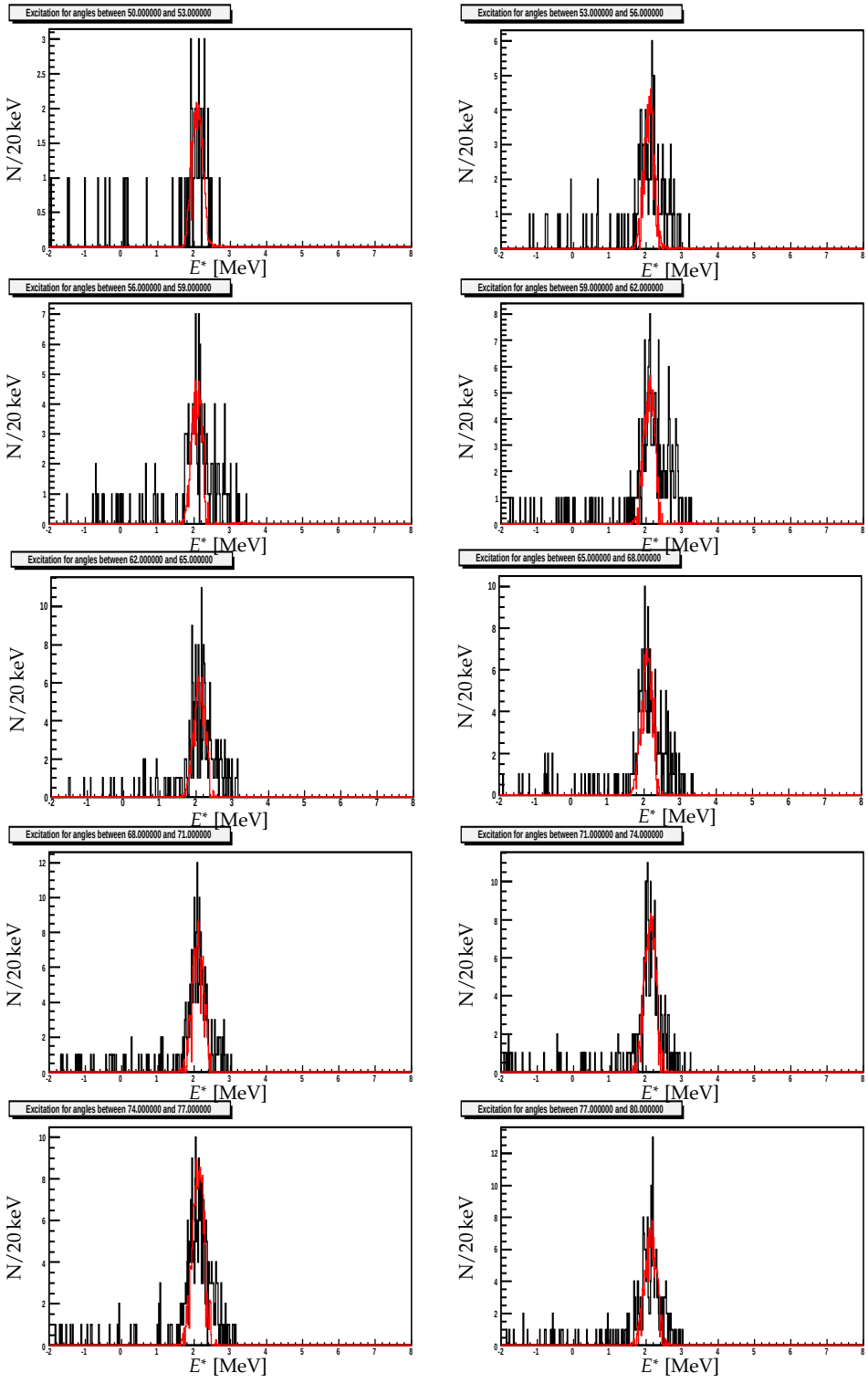

Figure 8.1: Excitation energy spectra made for small angular ranges, each one covering 3 º in center of mass. The simulated data (red) is scaled to best fit the experimental data (black). The scaling factor for each spectra provides the angular distribution.

generated for the simulated data, and the scaling factor (a) in a given center of mass angle is determined by fitting the simulated data to the experimental data using eqn. 3.8. Fig. 8.1 shows ten of these excitation energy spectra for the 2_1^+-state in ^{12}Be along with the scaled spectra from the simulated data. The angular distributions of the excited states are detemined from the gamma gated spectra. The fit is performed by adding the simulated spectra to the spectra from the background gates instead of subtracting the background gated spectra from the peak gated. This provides a more reliable uncertainty from the fit. The angular distributions for the ground states are calculated from the total excitation energy spectra. Again background spectra are made using background runs and gamma gated spectra, and the scaled simulation is added to these spectra in the fit.

The angular distributions calculated using gamma gates could be altered, if the gamma rays are emitted anisotropic. An anisotropic gamma ray emission would lead to a dependency in the MINIBALL detection efficiency (determined in section 5.7) of the angle of the outgoing particle. The effect was explored in an experiment using only limited angular coverage in the gamma detection [Bro12]. The effect should only be limited in this experiment due to the large angular coverage of the MINIBALL [Cat12], and the efficiencies determined will be used with no regards to the angle of the particles. The validity of this simplification is supported by a simple test performed on the data. The gamma gated spectra in the small angular intervals are compared to a non-gamma gated spectra in the same interval and perfect overlays are seen (like the comparisons in chapter 7)

Differential cross sections are calculated for all the bound states in ^{10,11,12}Be except for the 0_2^+-state in ^{10}Be, which was not seen in the analysis. A differential cross section is determined from the total number of events in the 2600 keV gamma peak in ^{10}Be. This cross section should be a combination of the differential cross sections from the 1_1^- and the 2_2^+-states and the differential cross section of the 2_2^+-state in ^{10}Be is determined by subtracting the 1_1^- differential cross section from the 2600 keV one. The total ($2_2^+ + 1_1^-$) and the 2_2^+ differential cross sections are shown as the last two plots in fig. 8.4. The differential cross sections will be shown along with the theoretic calculations in the next sections.

8.3 Scattering data

An important part of DWBA calculations are the potential between the initial nucleus and particle ($V_{^{11}\mathrm{Be,d}}$), section 8.4. This potential is normally determined from the elastic scattering data. The simplest approach is an optical model approach, which will be attempted first. The known deformation of ^{11}Be along with the small separation of the two bound states indicate a strong coupling of the two states. A deformed po-

tential is tested as well. The deformed potential creates differential cross sections for both the ground and the first excited state.

Parameter	Satchler [Sat66]	Perey [Per74]	Kanungo [Kan10] (H. Yan [Han06])	Kanungo [Kan10] (D. Auton [Aut70])
V_0	124.7	83.36	80.53	118.0
r_0	0.9	1.15	1.17	0.87
a_0	0.9	0.81	0.8	0.91
W_v	0	0	5.19	0
W_d	4.38	15.744	4.71	5.80
r_I	2.452	1.34	1.56	1.57
a_I	0.264	0.68	0.8	0.78
V_{so}	6.0	0	3.54	5.80
r_{so}	0.9	0	1.23	0.87
a_{so}	0.9	0	0.81	0.91

Table 8.1: Optical model parameters used to calculate the elastic scattering shown in fig. 8.2. All depths are in MeV and all distances in fm. The two reference in parentheses is the original references.

8.3.1 Optical model calculation

The optical model calculation is described in section 3.3.1 and the calculations are performed with four different potentials shown in table 8.1. The potentials are taken from three papers, Satchler et al. [Sat66], Perey et al. [Per74] and Kanungo et al. [Kan10]. The former two are based on generalised parameters for optical potentials derived from reactions of deuterons on stable nuclei. The latter provides two optical potentials used in a previous low energy ^{11}Be(d,p)^{12}Be experiment performed at TRIUMF in 2005. The total optical potential is given by:

$$U(r) = -V_0 f(x_0) - i\left(W_v f(x_I) - W_d \frac{\mathrm{d}f((x_I))}{\mathrm{d}x_I}\right) + V_{so}\left(\frac{\hbar}{m_\pi c}\right)^2 \frac{1}{r}\frac{\mathrm{d}f((x_{so}))}{\mathrm{d}x_{so}}(\vec{L}\cdot\vec{s}) \qquad (8.1)$$

where $f(x)$ is the Wood-Saxon:

$$f(x_i) = \frac{1}{1+\exp(x_i)} \tag{8.2}$$

$$x_i = \frac{r - r_i A^{1/3}}{a_i}. \tag{8.3}$$

Fig. 8.2 shows the experimental elastic scattering cross section (red dots) along with the four optical model calculations. None of the potentials can reproduce the experimental data and an attempt to adjust the potential depth of the real and the imaginary part to improve the the overlap has been unsuccessfull. The same was an attempt to use a large diffusiones for the imaginary part suggested by A. Bonaccorso et al. [Bon02]. The potential that reproduces the experimental data best is the Satchler potential and it will be used to make some first attempts of DWBA calculations of the transfer reactions.

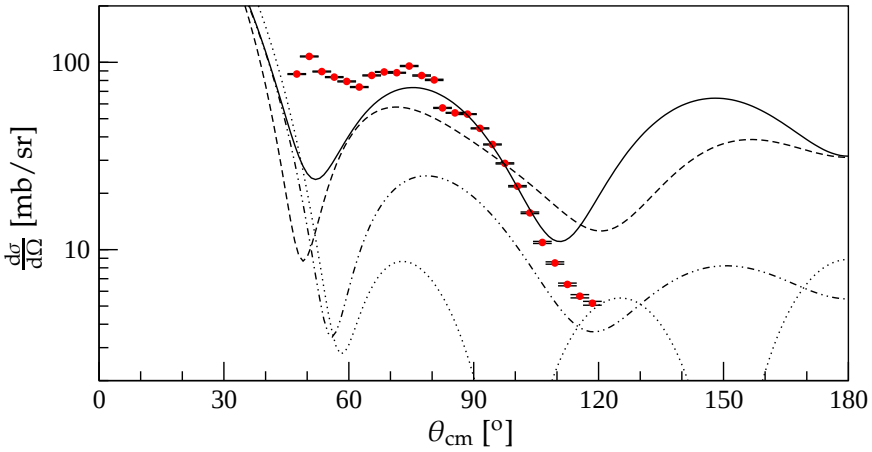

Figure 8.2: The differential cross section for ^{11}Be(d,d)^{11}Be. The experimental cross section (red dots) is plotted along with four different optical model calculations. The parameters are shown in table 8.1. Full line: Satchler et al. Dotted line: Perey-Perey et al. Dashed line: R. Kanungo et al. (set I). Dashed+dotted line: R. Kanungo et al. (set II).

The disagreement between theory and experiment could be caused by higher order reactions, which should be considered to improve the calculations. The first and only attempt made for these data is using a deformed potential, and will be described next. More complex reactions could also add to the differential cross section. Two contributions, that ought to be investigated, are the compound and the exchange reactions. Compound reactions are known to be present in almost all direct reactions to

some extent, and a significant contribution cannot be excluded for ^{11}Be(d,d)^{11}Be. The exchange reaction is suggested because of the two loosely bound neutrons, the one in ^{11}Be and the one in the deuteron. Both nuclei can easily deliver a neutron to the other (as seen in the two other reactions investigated here), and if they exchange a neutron it would look like a scattering reaction. No attempts to determine the contribution of these two reactions have been made.

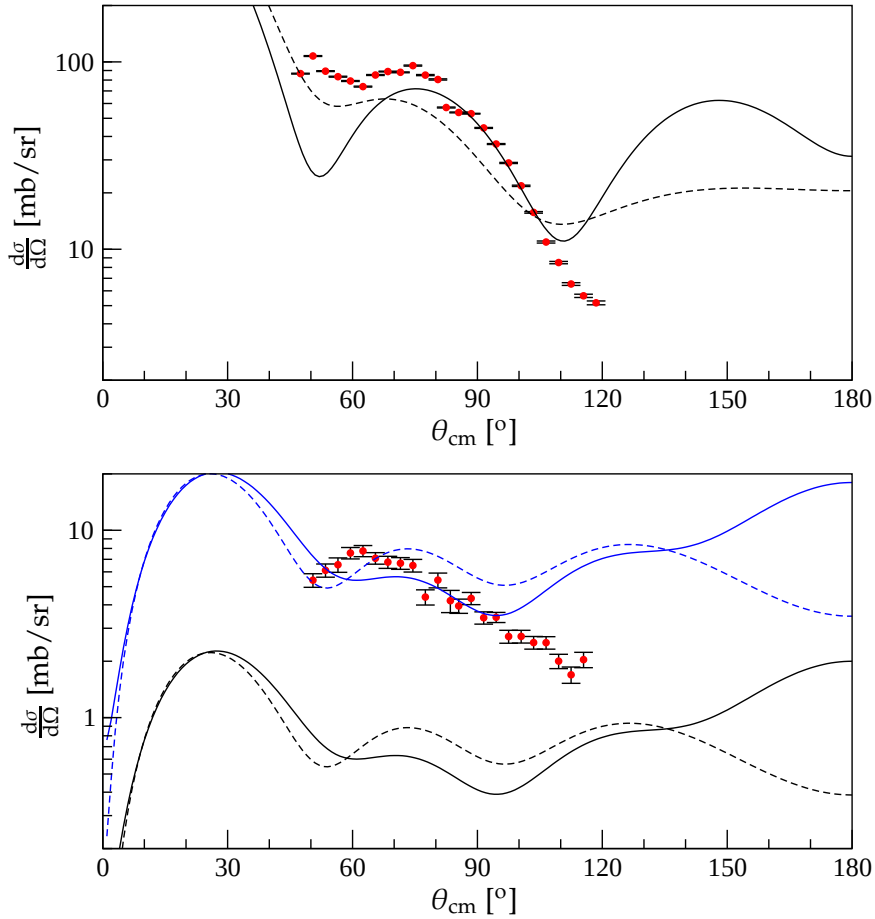

Figure 8.3: Differential cross sections for elastic (top) and inelastic scatterings (bottom). The experimental data (red dots) are compared to two deformed potentials, Satchler et al. (Full line) and a using modified depths for the Satchler potential (dashed line). The blue curves in the bottom are the theoretic curves scaled with a factor 9.

8.3.2 Coupled channel calculation

A deformation of the optical potential is added in an attempt to improve the elastic cross section and to calculate a theoretic differential cross section for the inelastic scattering to the first excited state in ^{11}Be. The deformation is set to:

$$\delta_1 = 0.84\,\text{fm} \quad \text{and} \quad \delta_2 = 1.27\,\text{fm}$$

taken from Hussein et al. [Hus08]. The parameters should lead to a coupling of the $1/2^-$ and the $1/2^+$ (even to the $5/2^+$) according to the selection rules in section 3.3.2. The deformation is added to the potential by Satchler et al. in a first attempt, full line in fig. 8.3. The elastic channel is not affected much and the inelastic channel is a factor 9 too low. The depth of the the reel and the imaginary potential is scaled to:

$$V = 120.18\,\text{MeV} \quad \text{and} \quad W = 19.535\,\text{MeV}$$

in order to improve the calculated cross section. The new values are determined using sfresco [Tho88]. While the shape of the elastic scattering differential cross section is improved at low angles, the agreement at large angles is worsened. The inelastic scattering channel is still a factor of 9 off and the deformed potential has to be modified further. Like the Satchler potential in the optical model the deformed potential with the modified depths will be used in the DWBA calculations of the transfer reactions.

8.4 Transfer reaction data

DWBA calculations are performed for both transfer reactions ((d,t) and (d,p)). The theory is described in section 3.3.3 and three potentials are needed to perform the integral in eqn. 3.40. The potentials involving deuterons are given in table 8.1 and in section 8.3.2. The potentials involving tritons and protons are listed in table 8.2 along with the papers they are taken from. The Be+p potential was derived from low energy scattering of protons on ^{12}C by J. R. Comfort et al. [Com80]. The potential was also used in the ^{11}Be(d,p)^{12}Be experiment at TRIUMF in combination with the last potential in table 8.1 [Kan10]. The Be+t is derived for low energy scattering of ^{3}He on ^{9}Be by J. Y. Park et al. [Par69]. The shapes are given in eqn. 8.1-8.3.

8.4.1 ^{11}Be(d,t)^{10}Be

Two calculations are made for the (d,t) reaction. The core-core potential (^{10}Be+d) (Satchler et al.) and the potential between the final nuclei (^{10}Be+t) (Park) will not be changed, but calculations using both the spherical (Satchler) and the deformed potential from section 8.3 for ^{11}Be+d, will be performed. The results are shown in fig. 8.4.

Parameter	Be+d Comfort [Com80].	Be+t Park [Par69].
V_0	57.8	172.5
r_0	1.25	1.2
a_0	0.25	0.5
W_d	8.08	6.8
r_I	1.4	1.2
a_I	0.22	1.85
V_{so}	6.5	5.0
r_{so}	1.25	1.2
a_{so}	0.25	0.5

Table 8.2: Optical potentials used in the DWBA calculations for the (d,p) and (d,t) transfer reactions along with the optical potentials from table 8.1.

The spectroscopic factors from the two calculations are given in table 8.3. None of the models reproduce the experimental data very well, and only the ground state is reasonably well described. Especially the shape of the 2_2^+-state cannot be reproduced. This may fall back on the experimental cross section. The inability to determine the 2_2^+ cross section independently leads to a large uncertainty. The discrepancy for the 1_1^- and the 2_1^--states could be an effect of the halo structures of the two states. The DWBA cross sections are too low for all the states in both calculations, leading to unrealistic high spectroscopic factors. Especially the deformed potential produces too low cross sections. This might be improved upon by adding a deformation to the ^{10}Be potentials as well. ^{10}Be is known to be deformed as well, and an investigation of the effect of the deformation could be interesting. At least more detailed calculations are required to provide more reliable results.

State in ^{10}Be	Spherical	Deformed
0_1^+	0.45(5)	2
2_1^+	1.2(2)	4
2_2^+	1.7	6
1_1^-	2.5	4.5
2_1^-	1.4(5)	4.5

Table 8.3: Spectroscopic factors determined from ^{11}Be(d,t)^{10}Be reactions. The results are only preliminary.

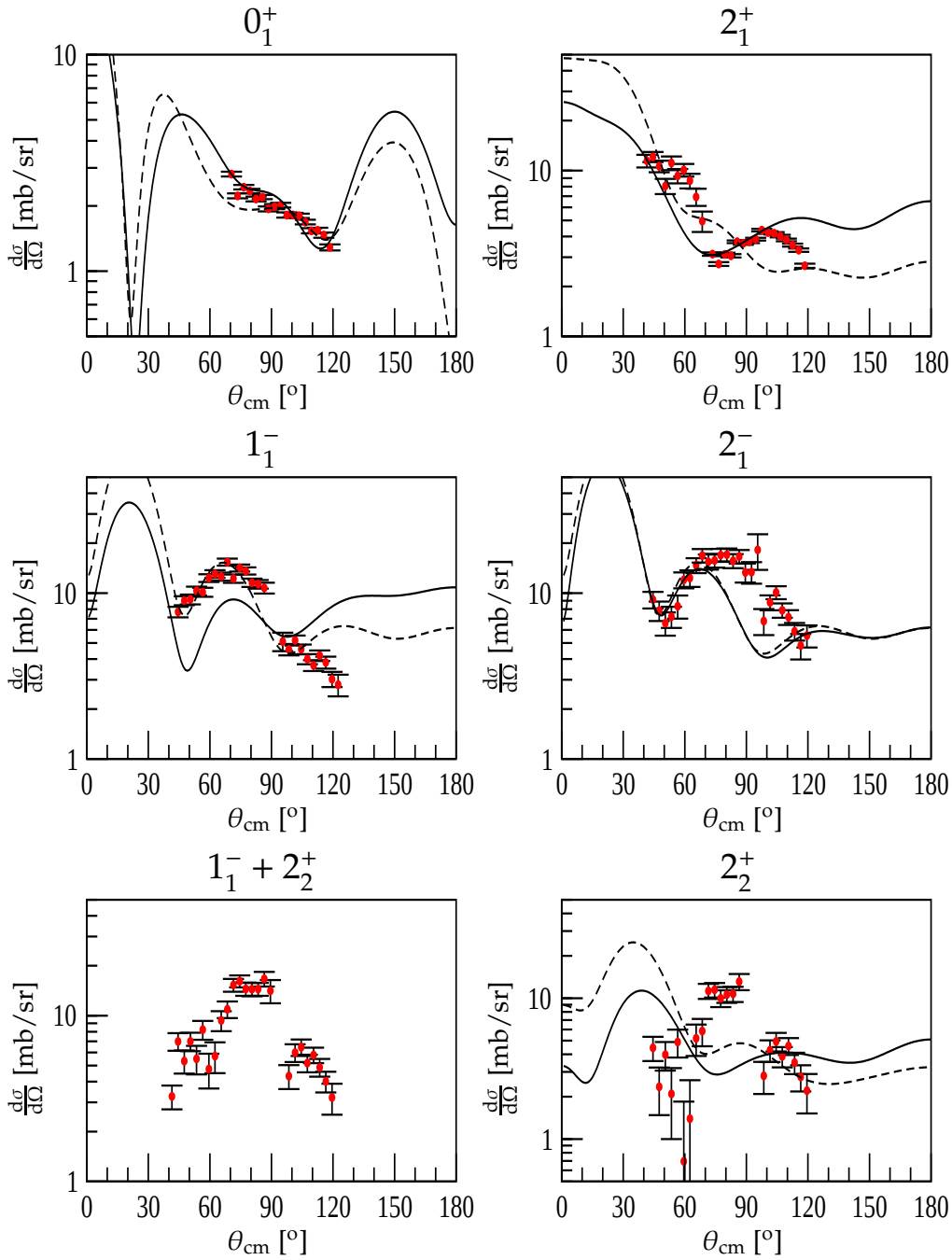

Figure 8.4: The experimental differential cross sections for (d,t) reactions (red dots) compared to two DWBA calculations, using a spherical (full line) potential and a deformed (dashed line). The $1_1^- + 2_2^+$ cross section is the cross section determined from gamma gating on the 2600 keV line. The 2_2^+ cross section is calculated by subtracting the 1_1^- from the $1_1^- + 2_2^+$.

8.4.2 ^{11}Be(d,p)^{12}Be

Three DWBA calculations are performed for the ^{11}Be(d,p)^{12}Be reactions. The spherical and the deformed potentials for ^{11}Be+d are tested. Furthermore calculations using potentials, taken from the previous ^{11}Be(d,p)^{12}Be experiment [Kan10], are performed in order to test their calculations. Only angles in the very forward direction in CM were covered in the experiment at TRIUMF and the data from this experiment can be used to validate the calculations at larger angles. The differential cross sections are shown in fig. 8.5 and the spectroscopic factors are given in table 8.4 along with spectroscopic factors determined in the experiment at TRIUMF and spectroscopic factors determined theoretically by H. Fortune et al. [For11].

Comparing the three DWBA calculations with the experimental data shows an almost perfect agreement for the ground state, especially the deformed potential reproduces the experimental data. The agreement worsens when going up in excitation energy. A very flat structure is seen in all the theoretical calculations and the experimental data for the 2^+_1-state. The experimental data has a slightly steeper curve though. Both the spherical and the deformed potential fail to reproduce the shape of the 0^+_2 and the 1^-_1, while the parameters taken from R. Kanungo et al. almost perfectly reproduces the shape of 0^+_2-state, though it still fails to describe the 1^-_1-state. Once again higher order terms are expected to influence the population of the high lying states in ^{12}Be. Especially the coupling into the continuum states in ^{11}Be is expected to play a significant part, and continuum discretized coupled channel (CDCC) calculations should be attempted next. Calculations, taking the proposed two-neutron halo structure of the 1^-_1-state into account, should be performed as well.

The spectroscopic factors determined using the same potentials as R. Kanungo et al. are compared to the factors determined in the experiment at TRIUMF. The factors are close to each other, except the 0^+_2-state. The 0^+_2 and the 2^+_1-states were not separated in the old experiment, which lead to large uncertainties on the 0^+_2-state. The value of 0.73 has later been questioned by H. Fortune et al. [For12]. The spectroscopic factors give an indirect comparison of the differential cross sections determined in the two experiments, and the strong agreement indicates reliable experimental cross sections.

All three sets of spectroscopic factors determined in this experiments are in good agreement, except for the 2^+_1-state, where the factor from the deformed potential is higher than the other two. The spectroscopic factors of the two 0^+-states are very close to each other. This indicates a similar amount of the $1s^2_{1/2}$ configuration in the two, and is evidence for the shell mixing in ^{12}Be. The theoretical calculated spectroscopic factors on the other hand are far off, only the 0^+_2-state is within a factor of 2 from the experimental data. A better agreement in the shape of the theoretic and experimental

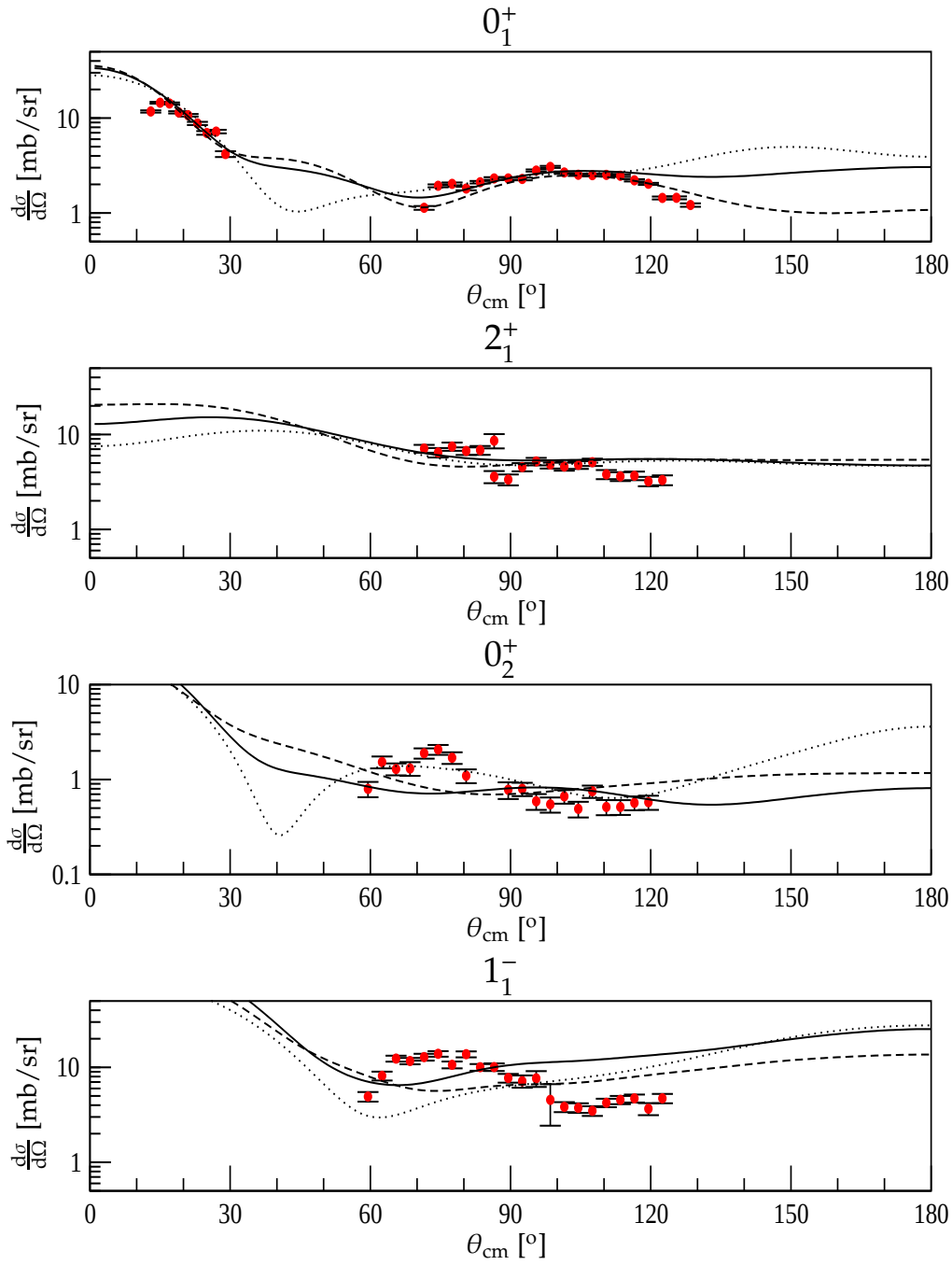

Figure 8.5: The experimental differential cross sections for (d,p) reactions (red dots) compared to two DWBA calculations, using a spherical (full line) potential, a deformed potential (dashed line) and potentials taken from the old (d,p) experiment (dotted).

State in ^{12}Be	Spherical	Deformed	Kanungo	TRIUMF [Kan10]	Theory [For11]
0^+_1	0.15(2)	0.25(5)	0.15(3)	$0.28^{+0.03}_{-0.07}$	0.78
2^+_1	0.15(5)	0.30(1)	0.075(25)	$0.1^{+0.09}_{-0.07}$	0.52
0^+_2	0.25(10)	0.20(8)	0.25(8)	$0.73^{+0.27}_{-0.40}$	0.37
1^-_1	0.55(20)	0.50(20)	0.27(15)	≈ 0.35	–

Table 8.4: Spectroscopic factors determined from ^{11}Be(d,p)^{12}Be reactions using three different potential parameters. The results are only preliminary. The spectroscopic factors determined in the experiment at TRIUMF are given along with theoretical calculated ones for comparison.

cross section is needed in order to fully disprove the theoretical spectroscopic factors though.

8.5 Summary

Experimental differential cross sections for all bound states, except one, in ^{10,11,12}Be were determined. A comparison with the theoretical calculations was not successful, and only the ground state of ^{12}Be could be successfully reproduced. Higher order reactions are expected to play a significant part in the reactions studied, and more detailed calculations are suggested. This includes, improving the optical potentials and attempting calculations using higher order terms. Compound reactions, exchange reactions and CDCC calculations have been suggested, but not yet performed. CDCC calculations on reactions involving both ^{11}Be and deuterons at higher beam energies have been performed before [Del07]. .

The spectroscopic factors determined for the (d,t) reactions were unrealistically high and must be improved upon. The large disagreement between the two (d,t)-calculations further confirmed the unreliability of the calculations. The spectroscopic factors from the (d,p)-data, on the other hand, were internally in good agreement and close to previously experimental determined factors. Evidence for the mixing of the $1s_{1/2}$ and the $0p_{1/2}$ shell was seen by comparing the spectroscopic factors for the two 0^+-states. Proving the breaking of the N=8 magic number. The latest theoretical calculated spectroscopic factors did not agree with the experimental results and a further investigation is necessary.

CHAPTER 9

^{11}Be+p reactions

While the primary reactions in the experiment were reactions of ^{11}Be on deuterons, the runs performed on regular polyethylene proved to have enough statistic for further direct reaction studies. The analysis of both (p,p) and (p,d) reactions seen in the runs of ^{11}Be on regular polyethylene are described in this chapter along with the differential cross sections and preliminary theoretic calculation.

9.1 Reactions on protons

During the experiment a few runs of ^{11}Be on a regular polyethylene target were performed, section 4.4. The runs were used to determine the background from reactions on protons in the deuterated polyethylene (chapter 7), but the data may also be used to study scattering and transfer reactions on protons. (p,d)-reactions have been used for years to study various nuclei including ^{10}Be and ^{11}Be [Win01]. ^{12}Be can not be reached using a proton target, but both ^{11}Be and ^{10}Be can be studied with these data.

9.2 The analysis of ^{11}Be+p data

The analysis of the reactions on protons are done exactly like the analysis of the reactions on deuterons described in the previous chapters, hence no detailed description will be given.

Both high energy deuterons and protons were identified in a $\Delta E - E$ plot and the excitation energies were calculated using eqn. 7.4. The excitation energy spectra are shown in fig. 9.1. Only the ground states of ^{11}Be and ^{10}Be are seen, hence only very limited inelastic scattering is possible. This is supported by the lack of a 320 keV peak in the gamma spectrum, fig. 9.2. None of the excited states in ^{10}Be are populated and only the two ground state are studied.

The differential cross sections of ^{11}Be(p,p)^{11}Be(gs) and ^{11}Be(p,d)10Be(gs) are calculated using the method described in section 8.2. An optical model calculation is done for the (p,p) scattering using a potential from J. R. Comfort et al. [Com80], seen in table 8.2. The optical model can once again not explain the experimental data. The

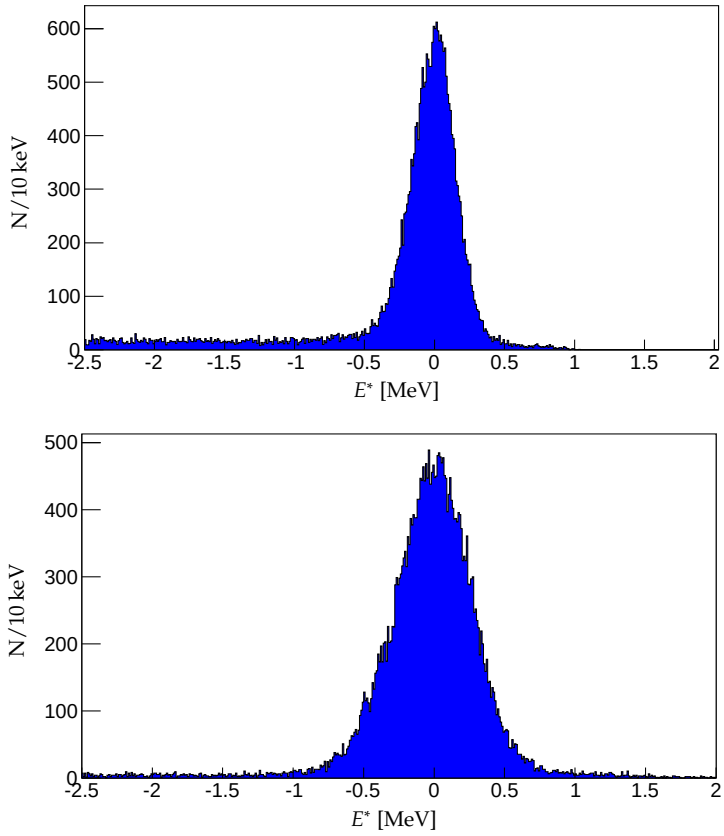

Figure 9.1: Excitation energy spectra made from runs on regular polyethylene. Top: The excitation energy of ^{11}Be calculated from scattered proton. Bottom: The excitation energy of ^{10}Be from (p,d) reactions.

disagreement between theory and experiment is even larger for (p,p) scattering than for (d,d). Higher order effects could play a significant part in the (p,p)-scattering. Especially compound reaction should be investigated further.

Preliminary DWBA calculations of ^{11}Be(p,d)^{10}Be are performed using the spherical (Satchler) and deformed potentials, also used in chapter 8, for ^{10}Be+d and the potential from Comfort et al. for Be+p. The shapes are much more consistent with the experimental data than the scattering events. Especially the deformed potential reproduces the experimental structure. The spectroscopic factors determined from

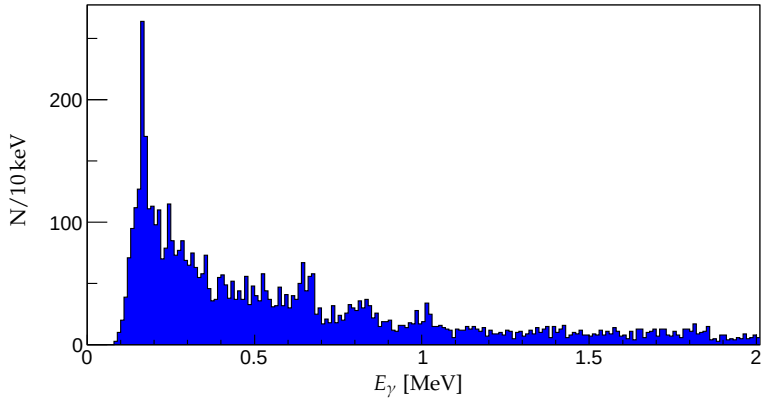

Figure 9.2: Gamma energy spectrum from gammas in coincidence with protons.

the DWBA calculations are:

$$\text{Spherical:} \quad S = \quad 1.25(35) \tag{9.1}$$

$$\text{Deformed:} \quad S = \quad 1.15(15) \tag{9.2}$$

$$\text{Theory:} \quad S = \quad 0.84 \tag{9.3}$$

$$\text{Prev. experiment:} \quad = \quad 0.67/0.79 \tag{9.4}$$

The theoretic value and previous experimental values are taken from Fortier et al. [For99]. Again the spectroscopic factors are too high and the theoretical calculations of the cross sections have to be improved.

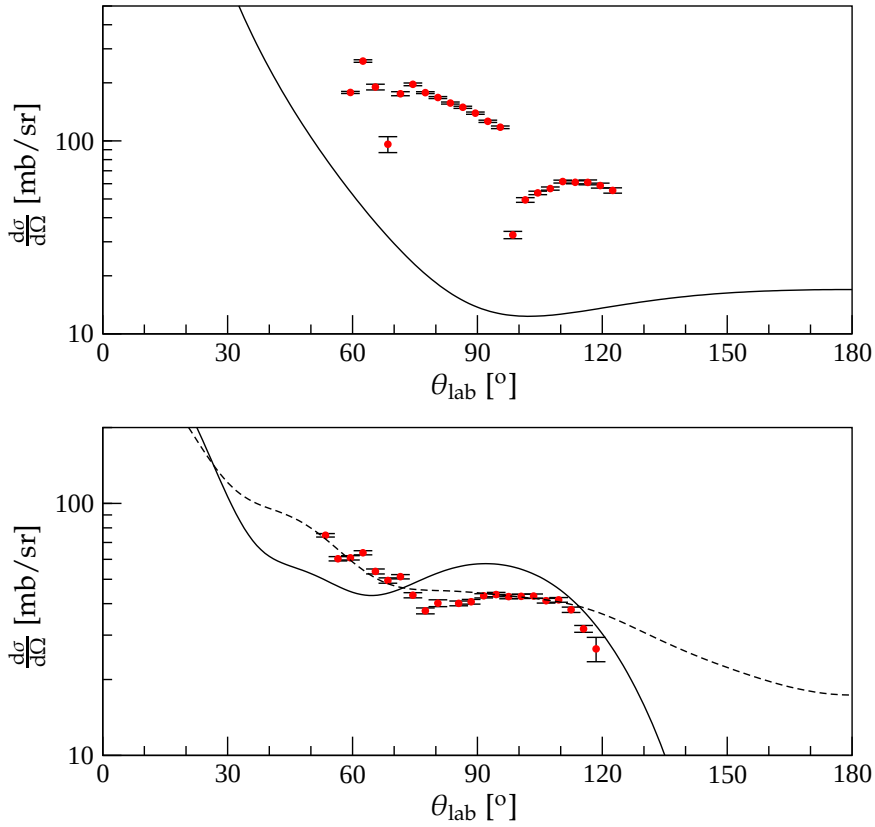

Figure 9.3: Experimentally determined differential cross section (red dots) for ^{11}Be(p,p)^{11}Be (top) and ^{11}Be(p,d)^{10}Be (bottom). The cross sections are compared to theoretical calculations using potentials from table 8.2 and 8.1. Full line: Spherical Be+d potential. Dashed line: Deformed Be+d potential.

CHAPTER 10

Further investigation of ^{12}Be

The differential cross section and spectroscopical factors determined in the previous chapters were the main aim of the experiment, but a further study of the (d,p) reaction led to interesting results. Results that will be presented in this chapter along with the analysis.

10.1 Lifetime measurement of the 0_2^+ state in ^{12}Be.

The lifetime of 0_2^+ state has been determined using the time difference between the detection of the 511 keV gammas and the protons. The long lifetime of the state has already been seen in fig. 7.7. Fig. 10.1 shows the time difference spectrum gated on the energy interval in table 7.1. A decay is seen after the main peak and the data from $\Delta t = 200$ ns to 500 ns are fitted to an exponential decay:

$$N = N_0 \exp -\frac{(\Delta t - t_0)}{\tau}. \tag{10.1}$$

The fitted value for τ was:

$$\tau = 3\,57(22)\,\text{ns}, \tag{10.2}$$

close to and consistent with the previous measured value of 3 31(17) ns [Shi07]. A better time resolution is needed to improve the lifetime measurement.

10.2 Investigation of a bound 0^- state in ^{12}Be

A bound 0^--state was suggested in ^{12}Be by C. Romero-Redondo et al. [RR08a] from a three body calculation. The state has never been seen experimentally, but due to low resolutions in previous experiments it has not been disproved either. The strength and high resolution of the T-REX and MINIBALL have already been shown in chapter 7, where the 2_1^+ and 0_2^+ states were separated in the data even though the difference in excitation energy is 100 keV. The setup should be able to detect and identify any bound 0^--state.

The excitation energy of the 0^- is only predicted with a large uncertainty in [RR08a]. The state is above the 2_1^+ ($E^* > 2100$ keV) and below the 1n threshold

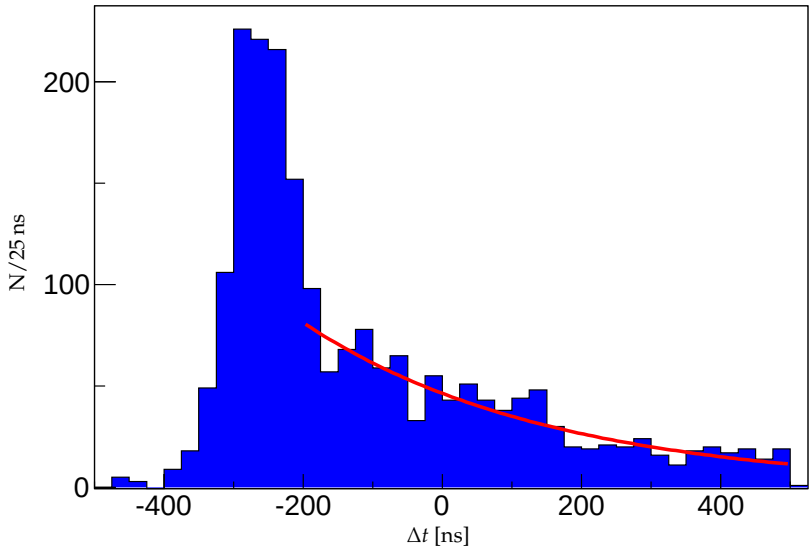

Figure 10.1: A lifetime measurement of the 0_2^+ state in ^{12}Be. A histogram of the time difference between the detected gamma and detected proton along with a fit to an exponential decay.

($E^* = 3160\,\text{keV}$). The decay channel and lifetime is dependent on the excitation energy of the 0_1^--state. If it is below the 1_1^--state it will decay to the 2_1^+ through a M2 transition and it will be a long lived state ($\tau \approx 10^{-8}\,\text{s}$). If it lies above the 1_1^- it will decay via a M1 transition to the 1_1^--state and it will have a short lifetime ($\tau \approx 10^{-11}\,\text{s}$).

The population strength of a bound 0^- in a (d,p)-reaction should be comparable to the population strength of the 1_1^--state. The energies are similar, and both have a ^{10}Be+sp structure. The 1_1^- is strongly populated as shown in chapter 7, hence a significant amount of a 0^--state should be seen.

The investigation of a bound 0_1^--state is done in three steps. First by studying the interval $E^* \in [2800\,\text{keV}, 3160\,\text{keV}]$ looking for a gamma line between 100 keV and 500 keV in the gamma spectrum for ^{12}Be, fig. 7.6. The short lifetime for the state above the 1_1^- would lead to a prompt doppler shifted gamma like the ones from the 2_1^+ and the 1_1^- decay. No gamma peak is seen in this area even with the larger MINIBALL efficiency at those energies, ruling out a 0_1^--state above 2800 keV. Secondly the interval $E^* \in [2200\,\text{keV}, 2700\,\text{keV}]$ is studied. The identification of the long lived 0_2^+ by looking at time delayed gammas shows the ability to identify long lived states in ^{12}Be. A 0^--state between the 2_1^+ and the 1_1^- states should produce a time delayed gamma line that

can be seen in fig. 7.7 as a vertical line, like the 511 keV. No other line below 600 keV is seen ruling out the second energy interval. This leaves the excitation energy of the 0^-_1 to be within 100 keV above either the 2^+_1 or the 1^-_1 state. Gamma gates cannot be used to study these areas, due to the lower energy limit of the MINIBALL at 100 keV. Instead the excitation energy spectrum without gamma gates is used. The background and gamma gated spectra could not fully explain all detected protons corresponding to $E^* > 0$ MeV, fig. 7.8. The gamma gated and background spectra are subtracted from the total to study this further, fig. 10.2. The ground state peak is still present as expected. A broad distribution ranging from 0.5 MeV to 2.8 MeV is also present. The distribution is too wide to be only one state and a part of it is expected to be background yet to be understood. The distribution is situated around 2.37 MeV and a bound 0^-_1-state above the 1^-_1 can be ruled out, leaving only the possible excitation energies of a bound 0^-_1-state to be within the interval $E^* \in [2100\,\text{keV}, 2200\,\text{keV}]$. The mean value of the distribution contradicts this, but a better understanding of the background is needed to fully rule out a bound 0^-_1-state in ^{12}Be. The events in the broad distribution might also stem from protons populating the 0^+_2-state in ^{12}Be. The gamma gate for the 0^+_2-state required a stopping of the ^{12}Be nucleus within the reaction chamber and the extra time gate might also cut away true events. These effects were already mentioned in section 7.2.3.2 and a larger positive uncertainty should be assigned to the spectroscopic factors of the 0^+_2-state in table 8.4.

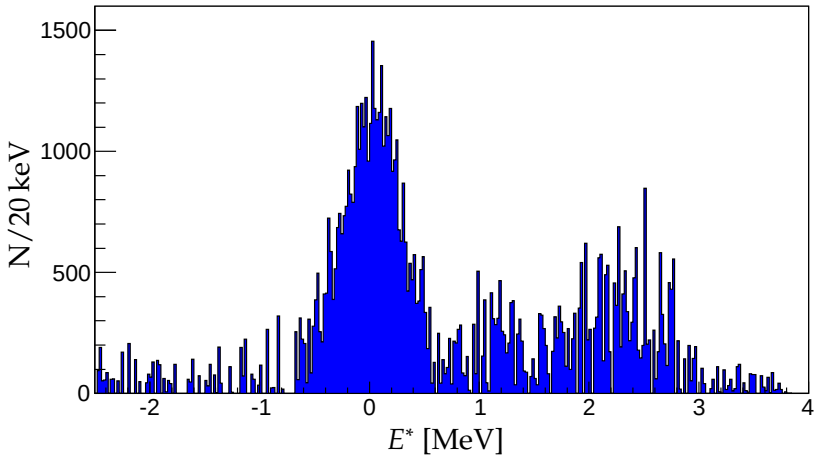

Figure 10.2: The excitation energy spectrum left after subtraction of gamma gated and background spectra. The ground state is clearly seen, but also a significant distribution with excitation energy above 0 MeV.

A recent three body calculation has shown the possibility of a broad 0^--resonance between the 1n and the 2n threshold rather than a bound state [Gar12]. This calculation is yet to be investigated, but it might be done by using the method described in the next section.

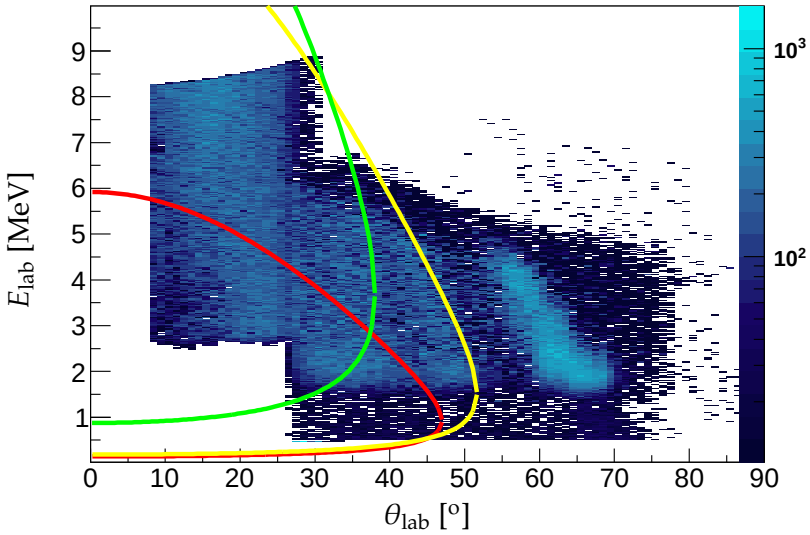

Figure 10.3: The energy vs. angle for all low energy particles in the forward direction. The kinetic curves for (d,p) (red), (d,d) (yellow) and (d,t) (green) populating the lowest resonances in ^{12,11,10}Be are shown as well.

10.3 Investigation of low lying resonances

So far only bound states of ^{10,11,12}Be have been investigated, but also low lying resonances are populated in the experiment. Indications of the $5/2^-$-resonance in ^{11}Be were seen in fig. 7.15. The investigation of the resonances are complicated by the low energy and small angles of the outgoing particles. Fig. 10.3 shows the kinetic curves for the outgoing proton (red), deuteron (yellow) and triton (green) from reactions populating the lowest resonances in ^{12}Be (E^* = 4.5 MeV), ^{11}Be (E^* = 1.8 MeV) and ^{10}Be (E^* = 7.3 MeV) respectively. The curves are plotted on top of a θ_{lab} vs. E_{par} for low energy particles. Background and states identified from gamma-gates are subtracted from the plot. The elastic scattered events, already investigated, are clearly seen, but do not interfere with the resonances. The three curves are entangled, and furthermore ^{4,6}He, ^{7,8,9}Li and ^{10}Be will also be seen with similar energies and angles.

A gate is needed to identify the three reaction types. Three attempts to make gates for the resonances are described in this section. All the attempts are based on the fact, that the resonances decay through neutron emission. The first one has successfully been used on the lowest resonance in ^{12}Be, and the analysis of this resonance will be fully described. Only some first attempts have been made for the last two, and a more detailed analysis is required to gain any information about resonances.

10.3.1 Gammas from decay products

The first method is to gate on gammas from the daughter nucleus. Hence the method requires neutron emission decay to an excited state in the daughter nucleus in order to get a subsequent gamma decay. Thus a study of the lowest resonances in ^{11}Be and ^{10}Be are impossible, with this method, as they decay completely to the ground state of ^{10}Be and ^{9}Be respectively. The low lying $1/2^-$-state in ^{11}Be makes it energetically possible for the lowest resonance in ^{12}Be to decay to the excited state in ^{11}Be, which will decay with a 320 keV gamma afterwards. The 320 keV is seen in coincidence with low energy particles, and has been used to identify the inelastic scattered deuterons, section 7.3.2.1. Fig. 10.4 shows the laboratory angle vs. the energy for the particles in concidence with a 320 keV gamma. Two curves are present in the plot. The strong curve around 60° is inelastic scattered deuterons, the wider and weaker curve at angles between 10^{0} and 40^{0} is interpreted as protons from the d(^{11}Be,p)^{12}Be reaction populating the lowest resonance in ^{12}Be. The red curve from fig. 10.3 fits perfectly with the experimental data.

The large separation between the deuterons and protons seen in the θ_{lab} vs. E plot makes it possible to distinguished the deuterons from the protons in the analysis, as seen in the gamma gated excitation energy spectrum in fig. 7.14 (the large background in the spectrum, mentioned in section 7.3.2.1, are the protons). All the gamma gated events are analysed as d(^{11}Be,p)^{12}Be reactions and an excitation spectrum is shown in fig, 10.5. The low energy peak is the deuterons, which are ignored, but the peak centered at 4.5 MeV is the ^{12}Be resonance. The width of the peak is determined by comparing the experimental data with simulations using various resonance widths. Three widths have been attempted: $\Gamma = 0$ keV (red), 200 keV (green) and 500 keV (yellow). The simulation with a delta function resonance is too narrow as expected. The offset in the mean value between the simulated and the experimental data, and the tail at 4 MeV, makes a precise measurement impossible. The best estimate is: $\Gamma = 20\,0(1\,00)$ keV, which is almost twice the accepted value of $1\,07(17)$ keV determined by H. Fortune et al. [For94].

The spin and parity of the resonance were initially predicted to be 2^+ by H. Fortune et al. [For94]. The strong population of the $1/2^-$ in ^{11}Be through first a (d,p)

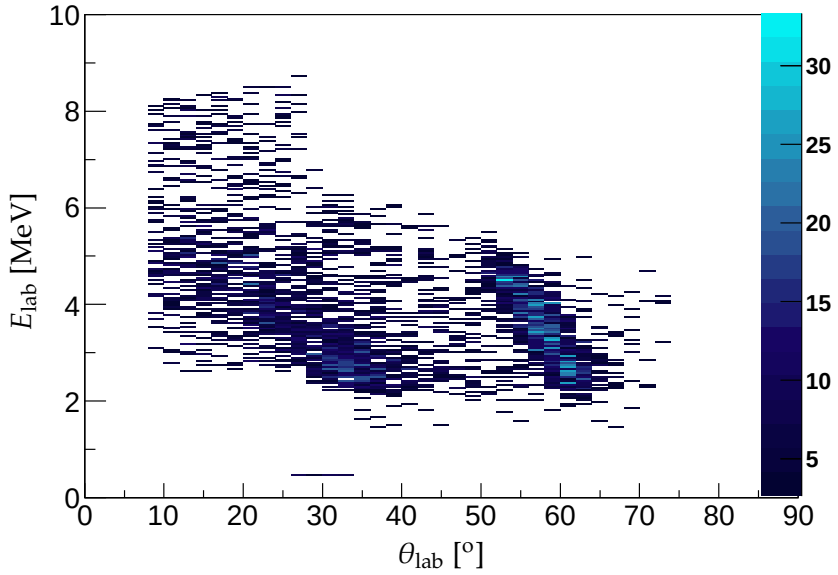

Figure 10.4: The energy as a function of the laboratory angle for low energy particles in coincidence with a 320 keV gamma. The inelastic scattered events are clearly seen, but also a curve at smaller angles are present. The curve is expected to be events from a (d,p) reaction populating the lowest resonance in ^{12}Be.

population of the resonance and then a decay to the $1/2^-$-state, contradicts this prediction. The branching ratio of a decay from a 2^+-resonance in ^{12}Be to the $1/2^-$-state in ^{11}Be has been estimated to less than 2 % by E. Garrido et al. [Gar12]. The branching ratio of the decay cannot be determined before a complete understanding of the last 25 % of the low energy particles is established (fig. 10.3), but a lower limit can be given. The lower limit is determined by comparing the number of particles in the gamma gated spectrum (ignoring the scattered deuterons) with all unidentified particles within ±500 keV of the red line in fig. 10.3. The lower limit is:

$$\text{BR(res)} \geq 10\,\%. \tag{10.3}$$

This is a very conservative limit, but still higher than the 2 % estimate for a 2^+-resonance. A branching ratio of 10 % would also lead to a differential cross section in the order of 50 mb/sr for the ^{11}Be(d,p)^{12}Be(res) reaction. This is almost a factor of ten higher than all the other (d,p)-cross sections and comparable to the elastic scattering cross section. A branching ratio above 50 % seems more reliable.

New theoretical calculations predict the spin and parity of the resonance to be

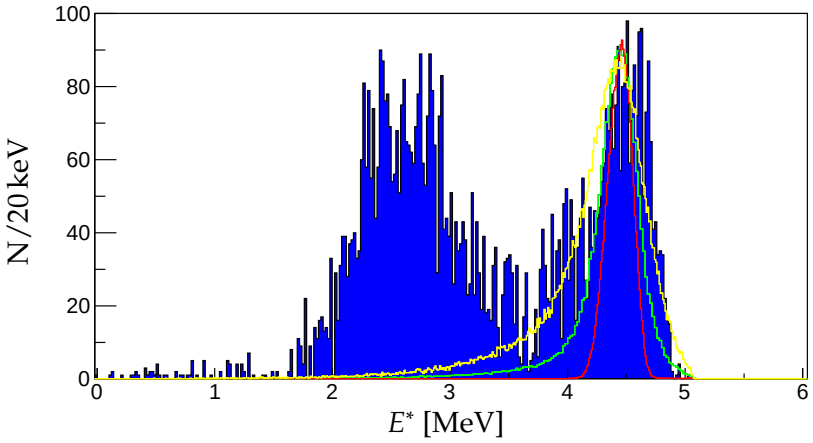

Figure 10.5: The excitation energy calculated assuming a (d,p) reaction for low energy particles in coincidence with a 320 keV. The low energy part is the inelastic scattered deuterons, and the peak at 4.5 MeV is the lowest known resonance in ^{12}Be. The resonance is compared with three simulations. The Different width of the resonance have been used in the simulations: red: Γ = 0 keV, green: Γ = 200 keV and yellow: Γ = 500 keV

either 1^- [Gar12] or 3^- [For11]. None of these values can be confirmed or disproved with the present knowledge.

10.3.2 Neutron detection using Ge-detectors

The second method is to detect neutrons from the neutron emission decay. Detection of neutrons in studies of resonances is not a new technique, and has been used in various experiments. Normally dedicated neutron detectors, like plastic scintillators, are used. The setup for this experiment was not designed for studies of resonances, hence no neutron detectors were present in the experiment.

Instead the MINIBALL Ge-detectors were used to indirectly detect the neutrons. The idea is to detect gammas from decays of excited germanium isotopes. The germanium isotopes are excited from inelastic scattering of neutrons (Ge(n,n')Ge*). The method was already suggested by Chasman et al. in 1969 [Cha65]. The three strongest gamma lines are shown in table 10.1, the fourth line in the table is from a long lived $0^+ \rightarrow 0^+$ transition in ^{72}Ge, described in Jenkins et al. [Jen09]. This decay was already mentioned in chapter 7. The advantage of the last line is the long lifetime, which enables a time and energy gate, like the gate for the 0_2^+-state in ^{12}Be made in

Reaction	E_γ [keV]
Ge(n,n')Ge*	600
	690
	835
	1035
^{11}Be+^{12}C	637 (^{22}F)
	821 (^{21}F)
	980 (^{8}Li)
^{22}Ne+d	1017 (^{23}Ne)

Table 10.1: Table showing the four strongest gamma lines produced from inelastic neutron scattering on germanium isotopes. Some nearby gamma lines from ^{11}Be+^{12}C and ^{22}Ne+d reactions are shown as well.

section 7.2.3.2. The three first are much stronger, but unfortunately the energies are very close to gamma lines from fusion reactions of ^{11}Be on ^{12}C, these lines are seen in table 10.1 as well. The gamma peaks are shown in fig. 10.6, all four peaks are visible, furthermore a very weak peak at 1210 keV ($\approx 2 \cdot 600$ keV) is seen indicating possibly detection of a two-neutron emission. The long lifetime of the 690 keV gamma was shown in fig. 7.7.

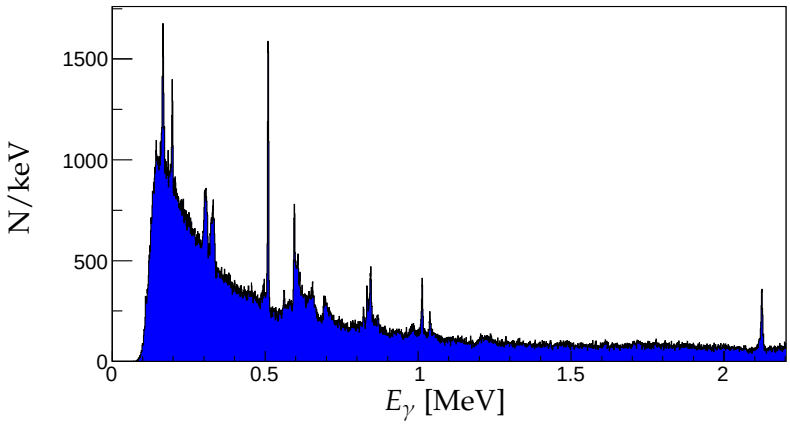

Figure 10.6: The gamma energies detected in coincidence with a low energy particle. The energies are not corrected for doppler shift.

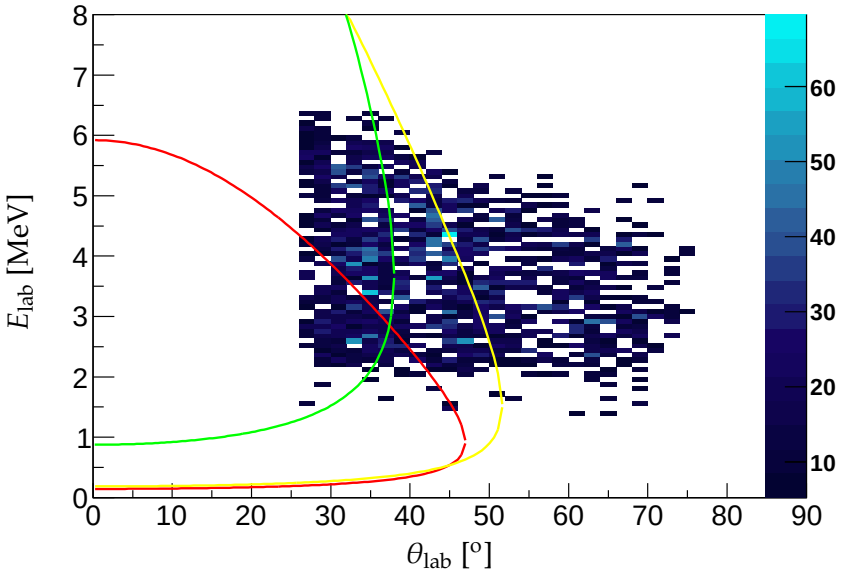

Figure 10.7: The energy vs. angle for low energy particles in the forward PSD's in coincidence with an expected neutron. The background from reactions on carbon is subtracted. The kinetic curves for (d,p) (red), (d,d) (yellow) and (d,t) (green) populating the lowest resonances in ^{12,11,10}Be are shown as well.

A gate has been made using all four peaks, both for reactions on deuterated polyethylene and on carbon. A θ_{lab} vs. E plot is made with the carbon data subtracted, fig. 10.7. The statistic is low, and no clear curves are seen. An indication of an increased intensity following the yellow ((d,d')) line is seen. Population of the $5/2^+$-resonance in ^{11}Be has already been identified, but not studied, fig. 7.15. The large number of events still present at angles above 50 degrees indicate a significant background in the plot, which prevents any clear identification of population of a resonance.

Furthermore, the neutron gate can not disentangle events from the three resonances, as they all decay by neutron emission. Gamma-gamma coincidences have been used in an attempt to disentangle the states. The lowest resonance of ^{12}Be has already been proven to decay to the $1/2^-$-state of ^{11}Be, which produces a 320 keV gamma. First attempt is to make a gate requiring two gammas, a 320 keV and a neutron, fig. 10.8A. The second attempt is to look for two neutrons in coincidence coming from a two neutron decay of ^{12}Be to the ground state of ^{10}Be, fig. 10.8B. The resonances in ^{10}Be and ^{11}Be are both under the two neutron threshold, and only the

^{12}Be resonance should decay with two-neutron emission. The statistics are extremely low for the particle-gamma-gamma coincidence events and a study of the 4.5 MeV-resonance in ^{12}Be cannot be performed without improving the analysis.

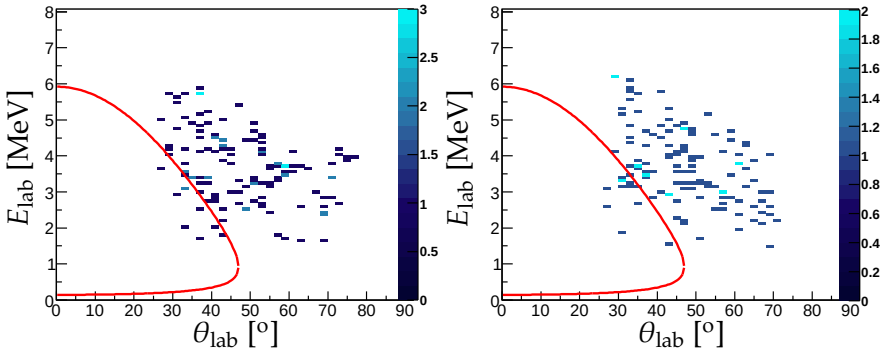

Figure 10.8: The energy vs. angle for low energy particles in the forward PSD's gated on gamma-gamma coincidence. Left: A coincidence of a neutron and a 320 keV gamma is required. Right: A coincidence of two neutrons is required. The red curve indicates the kinematics of the (d,p)-reaction populating the 4.5 MeV resonance in ^{12}Be.

10.3.3 Coincidence events analysis.

Instead of detecting the emitted neutron, which has been proven complicated, the heavy fragment can be detected. Coincidence events between tritons and ^{10}Be have already been used in chapter 6 for beam diagnostic. This proves that coincidence events occurs in this experiment for reactions to the bound states of ^{10}Be, and ^{11}Be. The outgoing angle of the nuclei decreases with the excitation energy, and the resonances are at the limit of our angular range. The emission of a neutron should for some events lead to a larger outgoing angle of the heavy fragment, making it possible to have coincidence events for reactions populating resonances.

The reactions to the bound states and the reactions to resonances can be separated by looking at the missing energy in the latter. In a reaction to a bound state, like the ground state of ^{10}Be, the two outgoing particles carries all the kinetic energy, while in a reaction populating a resonance some of the kinetic energy is taken by the undetected neutron. The two types of reactions can then be identified by calculating

the excitation of the nucleus in two ways:

$$E_1^* = T_A - T_b - T_B + Q. \quad (10.4)$$

$$E_2^* = T_A - T_b - \frac{P_B^2}{2m_B} + Q \quad (10.5)$$

$$(10.6)$$

The latter is the same as used in chapter 7 and provides the right excitation energy. The former will give the excitation energy minus the kinetic energy of the neutron. The equations require knowledge of the reaction, hence the excitation energies are calculated assuming all three reactions ((d,p), (d,d) and (d,t)) individually. The two excitation energies are plotted against each other, fig. 10.9. If the two excitation energies are the same ($E_1 = E_2$) for an event this is a true event to a bound state. If $E_1 > E_2$, the particles stem from another reaction (mainly fusion reactions) Finally if $E_2 > E_1$ for an event, it is either another reaction or a population of a resonance. Unfortunately no events are found with $E_2 > E_1$, that cannot be explained by another reaction. Three clear peaks are seen in the plots. The lowest is yet to be understood. The middle is scattered deuterons and the top one is tritons from population of the 6 MeV states in ^{10}Be.

This is only a quick first attempt to use this method and might be useful if improved upon.

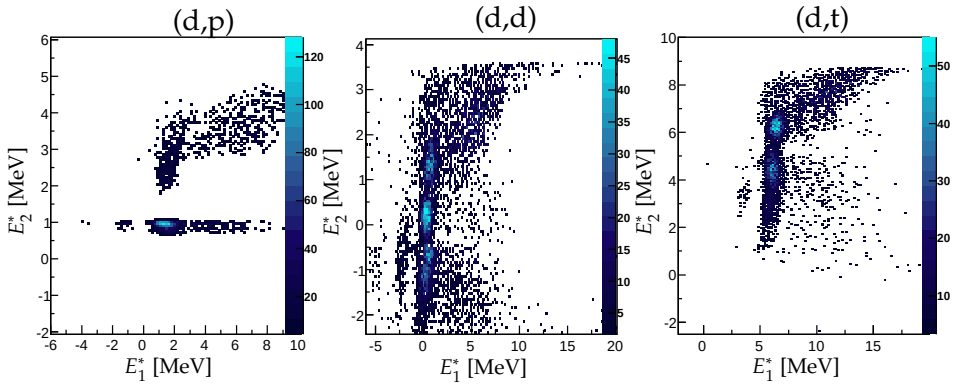

Figure 10.9: E_1^* vs. E_2^* for two particle coincidence events. The particles are analysed assuming three reactions: d(^{11}Be,p)^{12}Be (left), d(^{11}Be,d)^{11}Be (middle) and d(^{11}Be,t)^{10}Be (right)

10.4 Summary

Studies of ^{12}Be not related to the differential cross sections were described in this chapter. The experimental setup was not designed for these studies but the high statistic enabled it, though only results with large uncertainties could be provided.

The techniques used for the lifetime measurement and the study of the resonances should be applicable for other experiments and should provide inspiration for future work.

CHAPTER 11

Summary and outlook

The experimental investigation of neutron rich beryllium isotopes will be summarised in this chapter. Important parts and strengths of the experimental setup and the analysis will be highlighted, and the physical properties of the beryllium isotopes derived from the experiment will be given. An outlook on the future analysis of the data will be given along with suggestions for improvements in the experimental setup in the end.

11.1 Summary

The three neutron rich beryllium isotopes, ^{10}Be, ^{11}Be and ^{12}Be, have been studied in direct reactions at low energies. The study was performed in inverse kinematics using an intense ^{11}Be beam incident on a deuteron (and a proton) target. The experiment was performed at ISOLDE, CERN, using the REX-ISOLDE LINAC to produce a post-accelerated beam with an energy of 2.8 MeV/u. Light particles (p,d,t and α) were produced in reactions and detected by the T-REX setup. The T-REX setup provided an almost 2π-coverage in angles from 8 ^{o} to 152 ^{o} in the laboratory frame. The large spatial coverage of the T-REX and the high intensity of the beam enabled a high statistic study of the reactions. The only reactions studied in this thesis were ^{11}Be(d,p)^{12}Be, ^{11}Be(d,d')^{11}Be and ^{11}Be(d,t)^{10}Be for the deuteron target, and ^{11}Be(p,p)^{11}Be and ^{11}Be(p,d)^{10}Be for the proton target. The ^{11}Be(d,α)^{9}Li and ^{11}Be(d,^{6}He)^{7}Li reactions seen in the experiment have been considered background, but differential cross sections for the reactions can be determined with a more detailed analysis of the experimental data.

The T-REX setup only provided a low energy resolution and limited particle identification. The limitations of the T-REX were fully compensated by the detection of gammas with the MINIBALL array. The MINIBALL detectors provided energy resolution down to 10 keV and all populated states in ^{10,11,12}Be were successfully identified. Differential cross sections were calculated for angles between 60 ^{o} and 120 ^{o} in center of mass for all the identified states. This experiment provides the first experimental differential cross section for the 0^{+}_{2}-state in ^{12}Be. The angular ranges of the differential cross sections are sufficient to see structures in most of the cross sections. A comparison with simple theoretical calculations show a large discrepancy between

the experimental data and the theoretical models for most of the reactions. Especially reactions involving loosely bound final states could not be described with the simple theoretical models. All these states ($1/2^+$ and $1/2^-$ in ^{11}Be, 1^-_1 in ^{12}Be, and 1^-_1 and 2^-_1 in ^{10}Be) are expected to be halo states, which is known to affect the reaction mechanisms. The halo structure of the states are expected to be the main reason for the discrepancy. The effect of a halo structure, or at least a loosely bound neutron, on the reaction mechanism will play an important part in all reactions studied in this experiment due to the two halo nuclei in the initial state (^{11}Be and ^{2}H). The breakup of the deuteron in direct reactions is known to play an important part in reactions involving deuterons and CDCC calculations have been compared to DWBA calculations to investigate the effect [Upa12]. The coupling with continuum states is even more likely for ^{11}Be with a binding energy of only 501 keV. CDCC calculations should be the next step in the study of the differential cross sections provided by the experiment. An important ingredient in a detailed study of the coupling to the continuum is the population of the lowest resonance in ^{11}Be through inelastic scattering. A population of the resonance is identified in the experimental data, but no differential cross sections are calculated yet. The possibility of compound and exchange reactions should also be investigated.

Preliminary spectroscopic factors are determined for all the transfer reactions despite the discrepancy between the structures of the differential cross sections. The spectroscopic factors for the ^{11}Be(d,p)^{12}Be reactions were determined with three different sets of potentials and the obtained values were consistent. The spectroscopic factors for all but the 0^+_2-state were in good agreement with previous experimental results. The spectroscopic factors determined for the 0^+_2 are considered more reliable than the previous determined experimental value, due to the clear identification of the state. Evidence for the mixing of the $1s_{1/2}$ and the $0p_{1/2}$ shell was seen by comparing the spectroscopic factors for the two 0^+-states in ^{12}Be. This is a clear indication for the breaking of the N=8 magic number. However the spectroscopic factors can not confirm the latest shell model calculations. No reliable spectroscopic values are determined for the reactions to ^{10}Be (neither (d,t) nor (p,d)) and new calculations are required before comparing with theory.

The high statistic, high energy resolution and large angular coverage provided an excellent foundation for a more detailed analysis of the experimental data. A new analysis technique to determine the beam structure from coincidence events were derived. The structure of a low energy radioactive beam was determined with high precision at the reaction point for the first time, using the technique. The energy of a fully accelerated radioactive beam was also determined for the first time at REX-ISOLDE. The detailed knowledge regarding the beam structure lead to an increase in the energy resolution in spectra from charged particles and a far better agreement

between the simulated and experimental data.

The success in using coincidence events for beam diagnostic led to a first attempt to identifying resonances using coincidence events. The attempt was unsuccessful, but showed promising features. An attempt to use germanium detectors for neutron detection led to the same results. The technique has been known for years but never used in a study of direct reaction and the analysis has to be slightly improved before reliable results are obtained. A detection of the sequential decay of the lowest known resonance in ^{12}Be through the $1/2^-$-state in ^{11}Be was successfully performed, providing the first data on the decay of the resonance. Lower limits could be determined for the branching ratio (BR $\geq 10\,\%$) and the cross section ($\frac{d\sigma}{d\Omega} \gtrsim 5\,\mathrm{mb/sr}$), and a width was determined with high uncertainty. Stronger limits can be reached with a more detailed analysis of the data.

The possibility of cleanly identifying reactions populating the 0_2^+-state in ^{12}Be was utilised to determine the lifetime of the state and give a rough estimate of the branching ratio, confirming the established values from Shimoura et al. [Shi07].

All in all the experiment can be considered successful, and the results obtained show interesting effects.

11.2 Outlook

While the results, already obtained from the experiment, are abundant, further insight of the low mass region of the nuclear chart can be gained from the data. All information in the experimental data regarding the bound states of ^{10,11,12}Be are obtained, but more than 10 % of the data are yet to be fully understood. A further analysis should improve the knowledge already gained on the resonances populated in ^{11}Be and ^{12}Be. Especially a calculation of the differential cross section of inelastic scattering to the resonance in ^{11}Be would prove valuable in the understanding of the reaction mechanisms. Studies of Lithium isotopes could furthermore be performed by studying the outgoing helium particles, as could fusion reactions of ^{11}Be on ^{12}C.

Even though the experiment has proven very successful, improvements in the experimental setup could be useful. An important part missing in the data is the differential cross sections at small center of mass energies. Particles with small center of mass angles have low energy in the laboratory and information regarding these areas can only be obtained by either increasing the reaction energy or lowering the energy limit for detection. The latter requires an upgrade of the T-REX setup, ideally changing the PSD detectors to detectors with a lower threshold. An upgrade has been proposed and is being designed at the moment. The higher beam energy will be obtained with the upgrade of ISOLDE to HIE-ISOLDE. The first stage of the upgrade is planned to be ready late 2014/early 2015. The first stage should provide energies

up to 5 MeV/u, sufficient to detect protons from reactions populating excited states in ^{12}Be in the backward laboratory angles, even with the present T-REX setup.

Bibliography

[Aad12] G. Aad *et al.*, *Observation of a new particle in the search for the Standard Model Higgs boson with the ATLAS detector at the LHC*. Physics Letters B, **716**, 1 – 29 (2012), URL http://www.sciencedirect.com/science/article/pii/S037026931200857X.

[Ago03] S. Agostinelli *et al.*, *Geant4 – a simulation toolkit*. Nuclear Instruments and Methods in Physics Research Section A: Accelerators, Spectrometers, Detectors and Associated Equipment, **506**, 250 – 303 (2003), URL http://www.sciencedirect.com/science/article/pii/S0168900203013688.

[AK06] J. Al-Khalili and K. Arai, *Excited state halos in* ^{10}Be. Phys. Rev. C, **74**, 034312 (2006), URL http://link.aps.org/doi/10.1103/PhysRevC.74.034312.

[Alb78] D. E. Alburger *et al.*, *Core excited $T = 2$ levels in $A = 12$ from studies of* ^{12}Be. Phys. Rev. C, **17**, 1525–1530 (1978), URL http://link.aps.org/doi/10.1103/PhysRevC.17.1525.

[Aum00] T. Aumann *et al.*, *One-Neutron Knockout from Individual Single-Particle States of* ^{11}*Be*. Phys. Rev. Lett., **84**, 35–38 (2000), URL http://link.aps.org/doi/10.1103/PhysRevLett.84.35.

[Aut70] D. Auton, *Direct reactions on 10Be*. Nuclear Physics A, **157**, 305 – 322 (1970), URL http://www.sciencedirect.com/science/article/pii/0375947470901156.

[Bar76] F. C. Barker, *T=2 states of the A=12 nuclei*. Journal of Physics G: Nuclear Physics, **2**, L45 (1976), URL http://stacks.iop.org/0305-4616/2/i=4/a=001.

[Bil10] V. Bildstein, *Exploring the Island of Inversion with the d(30Mg, p)31Mg Reaction*. Ph.D. thesis, Tehnische Universität München (2010).

[Bil12] V. Bildstein *et al.*, *T-REX*. The European Physical Journal A - Hadrons and Nuclei, **48**, 1–10 (2012), 10.1140/epja/i2012-12085-6, URL http://dx.doi.org/10.1140/epja/i2012-12085-6.

[Boi09] H. Boie, *Bremsstrahlung Emission Probability in the Alpha Decay of 210Po*. Ph.D. thesis, Universität Heidelberg (2009).

[Bon02] A. Bonaccorso and F. Carstoiu, *Optical potentials of halo and weakly bound nuclei*. Nuclear Physics A, **706**, 322 – 334 (2002), URL http://www.sciencedirect.com/science/article/pii/S0375947402007558.

[Bro12] S. M. Brown *et al.*, *Low-lying neutron fp-shell intruder states in ^{27}Ne*. Phys. Rev. C, **85**, 011302 (2012), URL http://link.aps.org/doi/10.1103/PhysRevC.85.011302.

[Cat12] W. Catford (2012), private communication.

[Cau05] E. Caurier, G. Martínez-Pinedo, F. Nowacki, A. Poves and A. P. Zuker, *The shell model as a unified view of nuclear structure*. Rev. Mod. Phys., **77**, 427–488 (2005), URL http://link.aps.org/doi/10.1103/RevModPhys.77.427.

[CG97] M. Cortina-Gil *et al.*, *Proton elastic scattering on light neutron-rich nuclei*. Physics Letters B, **401**, 9 – 14 (1997), URL http://www.sciencedirect.com/science/article/pii/S0370269397003213.

[Cha65] C. Chasman, K. Jones and R. Ristinen, *Fast neutron bombardment of a lithium-drifted germanium gamma-ray detector*. Nuclear Instruments and Methods, **37**, 1 – 8 (1965), URL http://www.sciencedirect.com/science/article/pii/0029554X65903289.

[Cha12] S. Chatrchyan *et al.*, *Observation of a new boson at a mass of 125 GeV with the CMS experiment at the LHC*. Physics Letters B, **716**, 30 – 61 (2012), URL http://www.sciencedirect.com/science/article/pii/S0370269312008581.

[Com80] J. R. Comfort and B. C. Karp, *Scattering and reaction dynamics for the ^{12}C+p system*. Phys. Rev. C, **21**, 2162–2176 (1980), URL http://link.aps.org/doi/10.1103/PhysRevC.21.2162.

[Cur05] F. Currell and G. Fussmann, *Physics of Electron Beam Ion Traps and Sources*. IEEE Transactions on Plasma Science, **33**, 1763–1777 (2005).

[Del07] A. Deltuva, A. M. Moro, E. Cravo, F. M. Nunes and A. C. Fonseca, *Three-body description of direct nuclear reactions: Comparison with the continuum discretized coupled channels method*. Phys. Rev. C, **76**, 064602 (2007), URL http://link.aps.org/doi/10.1103/PhysRevC.76.064602.

[Des05] M. Descovich *et al.*, *In-beam measurement of the position resolution of a highly segmented coaxial germanium detector*. Nuclear Instruments

and Methods in Physics Research Section A: Accelerators, Spectrometers, Detectors and Associated Equipment, **553**, 535 – 542 (2005), URL http://www.sciencedirect.com/science/article/pii/S0168900205014385.

[DP10] A. Di Pietro *et al.*, *Elastic Scattering and Reaction Mechanisms of the Halo Nucleus ^{11}Be around the Coulomb Barrier*. Phys. Rev. Lett., **105**, 022701 (2010), URL http://link.aps.org/doi/10.1103/PhysRevLett.105.022701.

[Ebe01] J. Eberth *et al.*, *MINIBALL A Ge detector array for radioactive ion beam facilities*. Progress in Particle and Nuclear Physics, **46**, 389 – 398 (2001), URL http://www.sciencedirect.com/science/article/B6TJC-4326C6W-1J/2/43a6db81176f42612612bae508ee818b.

[Ebr12] J.-P. Ebran, E. Khan, T. Niksic and D. Vretenar, *How atomic nuclei cluster*. Nature, **487**, 341–344 (2012), URL http://dx.doi.org/10.1038/nature11246.

[Erl12] J. Erler *et al.*, *The limits of the nuclear landscape*. Nature, **486**, 509–512 (2012), URL http://dx.doi.org/10.1038/nature11188.

[For94] H. T. Fortune, G.-B. Liu and D. E. Alburger, *$(sd)^2$ states in ^{12}*Be. Phys. Rev. C, **50**, 1355–1359 (1994), URL http://link.aps.org/doi/10.1103/PhysRevC.50.1355.

[For99] S. Fortier *et al.*, *Core excitation in 11Begs via the p(11Be,10Be)d reaction*. Physics Letters B, **461**, 22 – 27 (1999), URL http://www.sciencedirect.com/science/article/pii/S0370269399008254.

[For11] H. T. Fortune and R. Sherr, *Structure of 2^+, $T = 2$ states in $A = 12$ nuclei*. Phys. Rev. C, **83**, 044313 (2011), URL http://link.aps.org/doi/10.1103/PhysRevC.83.044313.

[For12] H. T. Fortune and R. Sherr, *Consistent description of ^{11}Be and ^{12}Be and of the ^{11}Be(d,p)^{12}Be reaction*. Phys. Rev. C, **85**, 051303 (2012), URL http://link.aps.org/doi/10.1103/PhysRevC.85.051303.

[Fre10] M. Freer *et al.*, *Cluster Structure of 12C and 11Be*. Nuclear Physics A, **834**, 621c – 626c (2010), the 10th International Conference on Nucleus-Nucleus Collisions (NN2009), URL http://www.sciencedirect.com/science/article/pii/S0375947410001089.

[Gar12] E. Garrido, A. S. Jensen, D. V. Fedorov and J. G. Johansen, *Three-body properties of low-lying ^{12}Be resonances*. Phys. Rev. C, **86**, 024310 (2012), URL http://link.aps.org/doi/10.1103/PhysRevC.86.024310.

[Han01] P. Hansen, *Studies of single-particle structure at and beyond the drip lines*. Nuclear Physics A, **682**, 310 – 319 (2001), URL http://www.sciencedirect.com/science/article/pii/S0375947400006540.

[Han06] Y. Han, Y. Shi and Q. Shen, *Deuteron global optical model potential for energies up to 200 MeV*. Phys. Rev. C, **74**, 044615 (2006), URL http://link.aps.org/doi/10.1103/PhysRevC.74.044615.

[Hey11] K. Heyde and J. L. Wood, *Shape coexistence in atomic nuclei*. Rev. Mod. Phys., **83**, 1467–1521 (2011), URL http://link.aps.org/doi/10.1103/RevModPhys.83.1467.

[Hus08] M. S. Hussein and R. Lichtenthäler, *Exit doorway model for nuclear elastic breakup of weakly bound projectiles*. Phys. Rev. C, **77**, 054609 (2008), URL http://link.aps.org/doi/10.1103/PhysRevC.77.054609.

[Ita00] N. Itagaki and S. Okabe, *Molecular orbital structures in* ^{10}Be. Phys. Rev. C, **61**, 044306 (2000), URL http://link.aps.org/doi/10.1103/PhysRevC.61.044306.

[Iwa00] H. Iwasaki *et al.*, *Low-lying intruder* 1^- *state in* ^{12}*Be and the melting of the N=8 shell closure*. Physics Letters B, **491**, 8 – 14 (2000), URL http://www.sciencedirect.com/science/article/pii/S0370269300010170.

[Jen04] A. S. Jensen, K. Riisager, D. V. Fedorov and E. Garrido, *Structure and reactions of quantum halos*. Rev. Mod. Phys., **76**, 215–261 (2004), URL http://link.aps.org/doi/10.1103/RevModPhys.76.215.

[Jen09] D. Jenkins, R. Glover, R. Herzberg, A. Boston, C. Gray-Jones and A. Nordlund, *Proof-of-principle for fast neutron detection with advanced tracking arrays of highly segmented germanium detectors*. Nuclear Instruments and Methods in Physics Research Section A: Accelerators, Spectrometers, Detectors and Associated Equipment, **602**, 457 – 460 (2009), URL http://www.sciencedirect.com/science/article/B6TJM-4VK6N4T-F/2/272be12481f4aee2f25b1081ccf01db5.

[Jen11] K. Jennings, Byron, *Non-observability of Spectroscopic Factors*. arXiv:1102.3721 [nucl-ex] (2011).

[Jep04] H. B. Jeppesen, *Low-energy Nuclear reactions with the radioactive isotope 9Li*. Ph.D. thesis, Aarhus University (2004).

[Joh97] R. C. Johnson, J. S. Al-Khalili and J. Tostevin, *Elastic Scattering of Halo Nuclei*. Phys. Rev. Lett., **79**, 2771–2774 (1997), URL http://link.aps.org/doi/10.1103/PhysRevLett.79.2771.

[Kan10] R. Kanungo *et al.*, *Structure of states in 12Be via the 11Be(d,p) reaction*. Physics Letters B, **682**, 391 – 395 (2010), URL http://www.sciencedirect.com/science/article/B6TVN-4XPB6VM-1/2/74ac1dcd0b499f5eb7316abb66e3eed5.

[KE02] Y. Kanada-En'yo and H. Horiuchi, *Structure of excited states of* ^{11}Be *studied with antisymmetrized molecular dynamics*. Phys. Rev. C, **66**, 024305 (2002), URL http://link.aps.org/doi/10.1103/PhysRevC.66.024305.

[Kes03] O. Kester *et al.*, *Accelerated radioactive beams from REX-ISOLDE*. Nuclear Instruments and Methods in Physics Research Section B: Beam Interactions with Materials and Atoms, **204**, 20 – 30 (2003), 14th International Conference on Electromagnetic Isotope Separators and Techniques Related to their Applications, URL http://www.sciencedirect.com/science/article/pii/S0168583X02018864.

[Lee11] J. Lee *et al.*, *Neutron spectroscopic factors of* ^{34}Ar *and* ^{46}Ar *from* (p,d) *transfer reactions*. Phys. Rev. C, **83**, 014606 (2011), URL http://link.aps.org/doi/10.1103/PhysRevC.83.014606.

[Mat09] C. M. Mattoon *et al.*, *Line-shape analysis of Doppler-broadened* γ *lines following the* β *decay of* ^{11}Li. Phys. Rev. C, **80**, 034318 (2009), URL http://link.aps.org/doi/10.1103/PhysRevC.80.034318.

[Mil82] D. J. Millener, D. E. Alburger, E. K. Warburton and D. H. Wilkinson, *Decay scheme of* ^{11}Be. Phys. Rev. C, **26**, 1167–1185 (1982), URL http://link.aps.org/doi/10.1103/PhysRevC.26.1167.

[Mor06] A. Moro and F. Nunes, *Transfer to the continuum and breakup reactions*. Nuclear Physics A, **767**, 138 – 154 (2006), URL http://www.sciencedirect.com/science/article/pii/S0375947405012698.

[Nav00] A. Navin *et al.*, *Direct Evidence for the Breakdown of the* $N = 8$ *Shell Closure in 12Be*. Phys. Rev. Lett., **85**, 266–269 (2000).

[Nav09] P. Navrátil, S. Quaglioni, I. Stetcu and B. R. Barrett, *Recent developments in no-core shell-model calculations*. Journal of Physics G: Nuclear and Particle Physics, **36**, 083101 (2009), URL http://stacks.iop.org/0954-3899/36/i=8/a=083101.

[Nil55] G. Nilsson, S., *BINDING STATES OF INDIVIDUAL NUCLEONS IN STRONGLY DEFORMED NUCLEI*. Kgl. Danske Videnskab. Selskab, Mat. fys. medd., **29** (1955).

[Oer97] W. von Oertzen, *Dimers based on the a + a potential and chain states of carbon isotopes*. Zeitschrift für Physik A Hadrons and Nuclei, **357**, 355–365 (1997), 10.1007/s002180050255, URL `http://dx.doi.org/10.1007/s002180050255`.

[Pai06] S. D. Pain *et al.*, *Structure of ^{12}Be: Intruder d-Wave Strength at $N = 8$*. Phys. Rev. Lett., **96**, 032502 (2006).

[Pan97] V. R. Pandharipande, I. Sick and P. K. A. d. Huberts, *Independent particle motion and correlations in fermion systems*. Rev. Mod. Phys., **69**, 981–991 (1997), URL `http://link.aps.org/doi/10.1103/RevModPhys.69.981`.

[Par69] J. Park, J. Duggan, P. Miller, M. Duncan and R. Dangle, *Elastic scattering of 3He particles by 9Be and 11B between 4.0 and 18.0 MeV*. Nuclear Physics A, **134**, 277 – 288 (1969), URL `http://www.sciencedirect.com/science/article/pii/0375947469910525`.

[Per74] C. Perey and F. Perey, *Compilation of phenomenological optical-model parameters 1969 – 1972*. Atomic Data and Nuclear Data Tables, **13**, 293 – 337 (1974), URL `http://www.sciencedirect.com/science/article/pii/0092640X74900059`.

[Rad95] D. Radford, *ESCL8R and LEVIT8R: Software for interactive graphical analysis of HPGe coincidence data sets*. Nuclear Instruments and Methods in Physics Research Section A: Accelerators, Spectrometers, Detectors and Associated Equipment, **361**, 297 – 305 (1995), URL `http://www.sciencedirect.com/science/article/pii/0168900295001832`.

[Rii12] K. Riisager, *Halos and related structures*. arXiv:1208.6415 [nucl-ex] (2012).

[RR08a] C. Romero-Redondo, E. Garrido, D. Fedorov and A. Jensen, *Isomeric 0- halo-states in 12Be and 11Li*. Physics Letters B, **660**, 32–36 (2008), URL `http://www.sciencedirect.com/science/article/B6TVN-4RH2R92-3/2/d5b6ef359c08588395859934bd5e74c5`.

[RR08b] C. Romero-Redondo, E. Garrido, D. V. Fedorov and A. S. Jensen, *Three-body structure of low-lying ^{12}Be states*. Phys. Rev. C, **77**, 054313 (2008).

[Sat66] G. Satchler, *An optical potential for deuteron scattering from carbon*. Nuclear Physics, **85**, 273 – 287 (1966), URL `http://www.sciencedirect.com/science/article/pii/0029558266906249`.

[Sch12] K. T. Schmitt *et al.*, *Halo Nucleus* ^{11}Be*: A Spectroscopic Study via Neutron Transfer*. Phys. Rev. Lett., **108**, 192701 (2012), URL http://link.aps.org/doi/10.1103/PhysRevLett.108.192701.

[Shi03] S. Shimoura *et al.*, *Isomeric 0+ state in 12Be*. Physics Letters B, **560**, 31 – 36 (2003), URL http://www.sciencedirect.com/science/article/B6TVN-486BNXY-6/2/753156bbf61b4b566708cbc750f739d4.

[Shi07] S. Shimoura *et al.*, *Lifetime of the isomeric state in 12Be*. Physics Letters B, **654**, 87 – 91 (2007), URL http://www.sciencedirect.com/science/article/pii/S0370269307010131.

[Sor08] O. Sorlin and M.-G. Porquet, *Nuclear magic numbers: New features far from stability*. Progress in Particle and Nuclear Physics, **61**, 602 – 673 (2008), URL http://www.sciencedirect.com/science/article/pii/S0146641008000380.

[Sum07] N. C. Summers and F. M. Nunes, *Core excitation in the elastic scattering and breakup of 11Be on protons*. Phys. Rev. C, **76**, 014611 (2007), URL http://link.aps.org/doi/10.1103/PhysRevC.76.014611.

[Tal60] I. Talmi and I. Unna, *Order of Levels in the Shell Model and Spin of* Be^{11}. Phys. Rev. Lett., **4**, 469–470 (1960), URL http://link.aps.org/doi/10.1103/PhysRevLett.4.469.

[Tho88] I. J. Thompson, *Coupled reaction channels calculations in nuclear physics*. Computer Physics Reports, **7**, 167 – 212 (1988), URL http://www.sciencedirect.com/science/article/pii/0167797788900056.

[Tho06] J. Thompson, Ian, *FRESCO, Coupled Reaction Channels Calculations* (2006), URL www.fresco.org.uk.

[Tho09] J. Thompson, Ian and M. Nunes, Filomena, *Nuclear reactions for astrophysics*. Cambridge University press (2009).

[Tho11] M. Thoennessen and B. Sherrill, *From isotopes to the stars*. Nature, **473**, 25–26 (2011), URL http://dx.doi.org/10.1038/473025a.

[Tim10] N. K. Timofeyuk, *Overlap functions, spectroscopic factors, and asymptotic normalization coefficients generated by a shell-model source term*. Phys. Rev. C, **81**, 064306 (2010), URL http://link.aps.org/doi/10.1103/PhysRevC.81.064306.

[TUN] *Nuclear data evaluation project*. URL http://www.tunl.duke.edu/nucldata/.

[Upa12] N. J. Upadhyay, A. Deltuva and F. M. Nunes, *Testing the continuum-discretized coupled channels method for deuteron-induced reactions*. Phys. Rev. C, **85**, 054621 (2012), URL http://link.aps.org/doi/10.1103/PhysRevC.85.054621.

[Vou09] D. Voulot, *REX-Linac emittance measurents*. Internal note cern-be-note-2009-012, CERN, Geneva, CH (2009).

[Wim10a] K. Wimmer, *Discovery of the Shape Coexisting 0+ State in 32 Mg*. Ph.D. thesis, Tehnische Universität München (2010).

[Wim10b] K. Wimmer *et al.*, *Discovery of the Shape Coexisting* 0^+ *State in* ^{32}Mg *by a Two Neutron Transfer Reaction*. Phys. Rev. Lett., **105**, 252501 (2010), URL http://link.aps.org/doi/10.1103/PhysRevLett.105.252501.

[Win01] J. Winfield *et al.*, *Single-neutron transfer from 11Begs via the (p,d) reaction with a radioactive beam*. Nuclear Physics A, **683**, 48 – 78 (2001), URL http://www.sciencedirect.com/science/article/pii/S0375947400004632.

[Wus92] S. Wustenbecker *et al.*, *Atomic Effects on α-α Scattering to the* ^{8}*Be Ground State*. Z.Phys., **A344**, 205 (1992).

[Zie83] F. Ziegler, James, *SRIM - The Stopping Range of Ions in Matter:* (1983), URL http://www.srim.org/.

[Zoc12] F. Zocca, M. Fraser, E. Bravin, M. Pasini, D. Voulot and F. Wenander, *Development of a silicon detector monitor for the HIE-ISOLDE superconducting upgrade of the REX-ISOLDE heavy-ion linac*. Nuclear Instruments and Methods in Physics Research Section A: Accelerators, Spectrometers, Detectors and Associated Equipment, **672**, 21 – 28 (2012), URL http://www.sciencedirect.com/science/article/pii/S0168900211023357.

[Zwi79] B. Zwieglinski, W. Benenson, R. Robertson and W. Coker, *Study of the 10Be(d, p)11Be reaction at 25 MeV*. Nuclear Physics A, **315**, 124 – 132 (1979), URL http://www.sciencedirect.com/science/article/pii/0375947479906377.

List of Figures

List of Tables